ABSTRACT

Title of dissertation: MODELING AND OPTIMIZATION OF A PHOTOVOLTAIC-ELECTROLYSIS SYSTEM FOR HYDROGEN GENERATION

Aisha A. Al-Obaid
Doctor of Philosophy, 2019

Dissertation directed by: Professor Raymond A. Adomaitis
Department of Chemical and Biomolecular Engineering

Hydrogen production from water electrolysis is widely accepted to be the most sustainable source of hydrogen production, especially when integrated with renewable energy sources such as solar or wind energy. Nevertheless, considerable improvements still are needed for renewable hydrogen to be fully competitive with the current fossil fuel energy resources. In this work, we develop and apply computational tools to model hydrogen production from solar powered water electrolysis systems.

A kinetic and mechanistic investigation of the oxygen evolution (OER) and hydrogen evolution (HER) reactions on the active nickel-iron layered double hydroxide (NiFe LDH) electrode is presented. Both linear sweep voltammetry and electrochemical impedance spectroscopy measurements were combined with theoretical models describing the electrode kinetics to evaluate the OER and HER rate constants. The rate determining step and reaction mechanism of the OER and HER were identified as a result of this analysis.

A computational algorithm to model an integrated PV-electrolysis-battery system is presented with the goals of identifying the systems optimal design that maximizes the hydrogen production rate, minimizes the levelized cost of energy and total systems cost, while targeting a net-zero grid energy operation. The coupled system is connected to the electric grid to ensure uninterrupted operation of the electrolyzer. The model is simulated over one year to include both diurnal and seasonal weather variations. Over 2 million different design configurations were evaluated, 13 of which were chosen as the Pareto Front for this optimization problem.

Finally, we develop and apply computational tools to identify optimal design configurations when integrating a large number of PV cells under shady or faulty conditions. Monte Carlo simulation is used to introduce the stochastic effect and uncertainty generated by shading, and the model is simulated under different shading intensities. With the inclusion of a cost attribute, a multi-objective optimization problem is developed. Information entropy weight and the Technique for Order Preference by Similarity to Ideal Solution (TOPSIS) methods were combined to identify the optimal number of bypass diodes for each shading case. This computational platform can be extended towards developing simulation-based design tools for the integration of nano-scale energy devices.

MODELING AND OPTIMIZATION OF A PHOTOVOLTAIC-ELECTROLYSIS SYSTEM FOR HYDROGEN GENERATION

by

Aisha A. Al-Obaid

Dissertation submitted to the Faculty of the Graduate School of the
University of Maryland, College Park in partial fulfillment
of the requirements for the degree of
Doctor of Philosophy
2019

Advisory Committee:
Prof. Raymond A. Adomaitis, Chair/Advisor
Prof. Chunsheng Wang
Prof. Ganesh Sriram
Prof. Dongxia Liu
Prof. Taylor J. Woehl
Prof. Jeremy Munday

Dedication

I dedicate this dissertation to my amazing mother. Your unconditional love has sustained me throughout this journey.

Acknowledgments

I would like to express my deepest gratitude to Allah (God) who enlightened my way and gave me the strength and patience to complete my Ph.D research. I owe my gratitude to all the people who helped and supported me in completing my Ph.D thesis.

First and foremost, I'd like to thank my advisor, Professor Raymond Adomaitis for his support and encouragement. It has been a great pleasure to work with such an extraordinary individual. I also would like to thank my advisory committee Prof. Chunsheng Wang, Dr. Ganesh Sriram, Dr. Dongxia Liu, Dr. Taylor J. Woehl, and Dr. Jeremy Munday for their constructive feedback and professional advice. I would also like to thank Kuwait University for awarding me a graduate research fellowship.

I cannot begin to express my deep gratitude to the most amazing person in my life, my mother Maryam, who raised me to be the person I am today. Thank you for being there for me, thank you for believing in me, and thank you for being the most beautiful thing that happened to me in my life. Your unconditional love, continuous prayers and encouragement were the fuel that kept me going. You have always been and will continue to be my biggest role model in life.

This would not be complete if I didn't mention my two little angels, Abdulwahab and Abdulrahman. You truly colored my life (this is not just a metaphor, I literally have colors on some of my clothes). You are the pride and joy of my life.

I owe a special gratitude to my husband, Meshari, who believed in me, supported me, encouraged me, and also learned how to cook and change the kids diapers to make our lives easier. I also would like to thank all my family and specially my brothers and sisters: Fayza, Ibraheem, Mashael, Fahad, Haya, Fajer, Fatima, Abdulaziz, and Awasha. A special thanks to my friend and sister, Afnan, for her continuous support and comfort throughout my PhD journey. I also would like to express my gratitude to the rest of my family and friends for their encouragement and support.

Finally, I am grateful that I had the privilege of attending such a prestigious university: University of Maryland. I was blessed with the opportunity to work with the best and brightest minds in the field.

Table of Contents

List of Tables

List of Figures

List of Variables and Symbols

A^+	Set of positive ideal solution
A^-	Set of negative ideal solution
ACS	Annual cost of the system (\$/yr)
AM	Air mass
ast	Apparent solar time
Cap	Battery capacity (kWh)
$C_{a,j}$	Annual cost of component j (\$/yr)
C_{aCapital}	Annualized capital cost (\$/yr)
$C_{\text{aO\&M}}$	Annualized operation and maintenance cost (\$/yr)
C_{aRep}	Annualized replacement cost (\$/yr)
C_{dl}	Double layer capacitance formed at the electrode/electrolyte interface (F)
C_{p}	Pseduo-capacitance (F)
CPE	Constant phase element
CRE	Capital recovery factor
C_t	Counter for the number of shaded cells in a string
D	Decision matrix
d_i	Euclidean distances of alternative i
d_j	Diversity of information carried by attribute j
DoD	Battery depth of discharge (%)
E_{an}	Annual energy produced by the PV system (kWh/yr)
E_b	Battery energy (kWh)
E_{cloudy}	Solar irradiance of a cloudy day (W/m^2)
E_D	Direct component of solar irradiance (W/m^2)
E_F	Diffuse component of solar irradiance (W/m^2)
E_G	Global irradiance (W/m^2)
E_{sc}	Solar constant (=1366 W/m^2)
E_{total}	Total solar irradiance (W/m^2)
e	Information entropy
F	Faraday's constant (=96485 C/mol)
I_o	Dark saturation current (A)
I_{ph}	Photo-current (A)
I_{sc}	Short-circuit current (A)
i	Real discount rate
j	Current density (mA/cm^2)
k_i'	Electrochemical rate constant (mol cm^{-2}s^{-1})
k_i	Chemical rate constant (mol cm^{-2} s^{-1})
k_i^o	Partial standard chemical rate constant (cm s^{-1})
LCE	Levelized cost of energy (\$/kWh)
M	Number of cells connected in parallel

M_{pv}	Number of PV modules connected in parallel
N	Number of cells connected in series
NGE	Net grid energy (kWh)
$n_{\mathrm{H_2}}$	Hydrogen production rate (mol/s)
n_j	Lifetime of the j^{th} component (PV module, electrolyzer, battery) (yr)
$\vec{n_i}$	Vector normal to and pointing out of the PV module surface
P	Normalized decision matrix
P_e	Power of the Electrolyzer (kW)
P_{mp}	Maximum power point of the PV module (kW)
R_{cell}	Total cell electrolyte resistance (Ω)
R_{ct}	Reaction charge transfer resistance across the electrode/electrolyte interface (Ω)
R_{F}	Faradaic resistance (Ω)
R_{f}	Film porous structure resistance (Ω)
R_{p}	Pseduo-resistance (Ω)
R_{s}	Ohmic electrolyte resistance (Ω)
R_{s}	Series resistance (when used in diode equation) (Ω)
R_{sh}	Shunt resistance (Ω)
$RNGE$	Relative net grid energy (%)
SEC	Specific energy consumption (kWh/Nm^3)
$\vec{s}$	Solar radiation vector
t_d	Number of days past the most recent winter solstice
$V_{\mathrm{H_2}}$	Hydrogen volumetric production rate (Nm^3/h)
U_j	Unit capital cost (\$/kW)
V_{mp}	Maximum power voltage (V)
$U_{\mathrm{O\&M},j}$	Unit operating and maintenance cost (\$/kW)
V_{oc}	Open-circuit voltage (V)
w	Objective weight associated with each attribute
X	Dimensionless concentration factor
z	Site elevation (km)
β	Diode ideality factor
β_i	Symmetry factor
δ	Earth's declination at $t_d = 0$ ($= 23.44^o$)
ζ	Zenith angle (^{o})
ζ_i	Relative closeness of alternative i to the ideal solution
η	Overpotential (V)
η_b	Battery charging efficiency (%)
Θ	Fraction of the surface coverage of the adsorbed intermediate
θ	Longitude (^{o})
θ_{tilt}	PV module tilt angle (^{o})

λ_y Angle representing Earth's mean orbit (^{o})
ϕ Latitude measured north of the equator (^{o})

Chapter 1: Introduction

1.1 Hydrogen Production from Renewable Energy Sources

Currently, finite fossil fuel resources supply the vast majority of the world's energy demand [1]. The scarcity of fossil fuel resources, the rising global energy demand, and the measurable climate change have stressed the need for renewable energy sources [1].

Hydrogen, as an energy carrier, is a promising candidate to supply the world's energy demand. Nevertheless, significant technological barriers must be overcome for hydrogen to be competitive with current energy resources [2]. Research interest is growing in hydrogen-economy based applications through either enhancing current technologies or designing new production processes, enabling the production of hydrogen in an efficient and cost effective manner. In addition to production, challenges in hydrogen storage, transportation, and distribution must be tackled simultaneously before the hydrogen economy can function at grid-scale level applications [3]. Currently, up to 96% of hydrogen production is fossil fuel based, which poses significant long-term environmental threats [4].

To tackle this issue and mitigate the environmental threats, research focus has shifted towards using renewables as energy source for hydrogen production. As such,

a range technologies have been developed for the production of renewable hydrogen. Among them are water electrolysis, biomass conversion, and solar conversion [5].

Water electrolysis is the most mature technology. It is a process of splitting water into oxygen and hydrogen by applying electrical potential across two electrodes. Water splitting reaction consists of two primary half reactions: oxygen evolution reaction (OER) and hydrogen evolution reaction (HER). To promote sustainability, renewable energy sources, such as solar or wind, can be used to generate the electricity. Biomass conversion involves thermochemical or biochemical processes to convert biomass into intermediates that can be further reformed to produce hydrogen [5]. Hydrogen production directly from biomass fermentation is another example of a biomass conversion process [5]. Solar conversion examples include thermolysis, using concentrated solar power systems to drive thermochemical reactions, and photolysis, where solar photons are used in biological or electrochemical systems to produce hydrogen [5].

Hydrogen production by water electrolysis is widely accepted to be the most sustainable source of hydrogen production, especially when integrated with renewable energy sources such as solar or wind energy [4]. It also has the advantage that it is capable of producing extremely pure hydrogen (>99.999%), which is ideal for some applications such as fuel cell vehicles. Despite it being known for over 200 years, hydrogen production from water electrolysis constitutes less than 4% of the current hydrogen economy [6].

1.2 Active Catalysts for Water Splitting

Numerous efforts have been devoted to developing new catalytic materials with low cost and high electrocatalytic activity towards water splitting reaction [7]. In the past few decades, research focus has shifted from the conventional expensive noble metals, such as Pt and RuO_2, towards using efficient, Earth-abundant, and low cost materials. Among these are transitional metal based materials which offer high catalytic activity, high stability, and low cost.

Recently, layered double hydroxides (LDH) have attracted enourmous attention for water splitting applications. LDH materials consist of positively charged Brucite like layers with divalent or trivalent metal hydroxides. The positive charge on these layeres originates from the partial substitution of divalent metal cations, such as Ni^{2+}, Fe^{2+}, Mg^{2+}, Co^{2+}, Cu^{2+}, or Zn^{2+}, with trivalent metal cations like Fe^{3+}, Al^{3+}, or Mn^{3+} [8]. The interlayer space separating the LDH layers consists of anions, such as CO_3^{2-} or NO_3^-, compensating the positively charged LDH layers [9], [10]. A graphical representation of an LDH materiel can be found in [8].

Lu et al [9] investigated the electrocatalytic activity of a three-dimensional NiFe LDH electrode towards the OER in alkaline media. Compared to a $Ni(OH)_2$ electrode, the LDH electrocatalyst demonstrated superior activity toward the OER. The prepared NiFe LDH catalyst was deposited on Ni foam substrate via a one-step hydrothermal synthesis. The electrode reported a Tafel slope of 50 mV/dec and an overpotential of 280 mV at a current density of 30 mA/cm^2. This electrode also demonstrated high stability with minimal current degradation of 2.2% under a

10-hour long constant overpotential application in 1 M KOH electrolyte.

Luo et al [7] also prepared NiFe LDH electrocatalysts on Ni foam via a simple one-step hydrothemal synthesis. Their prepared films were tested toward both OER and HER in 1 M NaOH electrolyte. The films reported overpotentials of 240 and 210 mV towards the OER and HER, respectively, at a current density of 10 mA/cm^2. Their water-electrolysis cell was powered by a perovskite tandem cell, allowing a water splitting current density close to 10 mA/cm^2 at an applied voltage of 1.63 V and a solar-to-hydrogen (STH) efficiency of 12.3 %.

Li et al [10] proposed a new electrochemical method for the fabrication of Fe-containing layered double hydroxide (MFe-LDHs, M = Ni, Co and Li). The ultrathin LDH nanoplatelets were grown perpendicular on Ni-foam substrate via a 300 seconds electrosynthesis procedure followed by a 1-hour long self-oxidation process in air. All three electrodes demonstrated high electrocatalytic activity toward OER, with a superior performance of the NiFe LDH electrode. Their NiFe LDH electrode reported a Tafel slope of 52.8 mV/dec and an overpotential of 224 mV at 10 mA/cm^2, which is 65 mV less than the commercial Ir/C electrode. This fast and effective LDH preparation method is favorable for large-scale production applications.

Fan et al [11] reported an active Nickel-Vanadium monolayer double hydroxide for OER, with a Tafel slope of 50 mV/dec and an overpotential of 300 mV at 10 mA/cm^2, which is comparable to, but does not exceed, the best-performing NiFe LDH reported in the literature.

Hou et al [12] prepared a ternary hybrid electrode consisting of NiFe LDH nanosheets hydrothermally deposited on vertically oriented cobalt selenide (CoSe)

supported on exfoliated graphene foil for overall water splitting. Their efficient 3D hybrid electrode used as OER and HER catalyst demonstrated superior activity, achieving a cell current density of 20 mA/cm^2 at 1.71 V, which is well comparable to the integrated performance of Pt/C and Ir/C catalysts.

In addition to its superior performance as an electrocatalyst, NiFe LDH is a promising photocatalyst for photo-induced water splitting reaction. Nayak et al [13] synthesized layered graphitic carbon nitride (g-C_3N_4) and NiFe LDH composite photocatalyst for visible light-induced photocatalytic water splitting. They studied the structural, optical, and morphological properties of multiple composites prepared at different g-C_3N_4 wt% loading. The estimated band-gap values of the prepared composites increased from 2.2 to 2.7 eV as the g-C_3N_4 loading increased from 0 to 100 wt%. Photocatalytic activity measurement were taken under visible light irradiation region, and the prepared composites reported high activity toward both OER and HER, with an optimal performance of the composite with g-C_3N_4 content of 10 wt%.

Over the past two decades, LDHs properties have been tailored to meet practical application requirements in different fields [8]. The application of LDHs is not limited to their usage as active catalysts, but also can be used as flame retardants, drug delivery hosts, additives in polymers, and as biomaterials [8], [9]. Ohashi et al [14] presented the application of MgAl LDH as a non-swelling durable electrolyte in a solid-state alkaline fuel cell. The LDH catalyst reported promising results, however, the authors suggested that the electron conduction resistance can be enhanced by assuring the carbon black particles have adequate contact with each other. Ad-

ditionally, Li and coworkers [15] developed a biocompatible and stretchable double-carrier drug delivery system for wound healing applications. Their double-carrier drug delivery system consists of drug-loaded MgAl LDH nanoparticles incorporated in hydrogel. The addition of the drug loaded LDH into the hydrogel significantly enhanced the mechanical properties and biocompatibility of the hydrogel, and delayed the drug release, making it a promising candidate for chronic wound healing applications.

In this work, NiFe LDH is chosen as an electrocatalyst for both OER and HER due to its high electrocatalytic activity toward both reactions, simple preparation methods, low cost, and Earth abundance. Although it is not the optimal catalyst for the HER, it offers economic benefits arising from the use of the same material for both electrodes while maintaining high catalytic activity [16].

Recent studies demonstrated that tailoring NiFe LDH electrocatalyst can deliver superior activity toward the HER. Chen et al [17] presented a strategy to expedite the HER kinetics on NiFe LDH by partially substituting Fe atoms with Ru. The Ru-doped NiFe catalyst demonstrated superior electroactivity, with an overpotential as low as 29 mV at 10 mA/cm^2 current density, with a Tafel slope of 31 mV/dec in 1 M KOH electrolyte. Additionally Chen et al [18] reported a similar strategy to enhance the performance of NiFe LDH as a HER electrocatalyst, by doping it with Iridium (Ir^{4+}). The Ir^{4+}-doped NiFe LDH catalyst reported an overpotential of 34 mV at 10 mA/cm^2 current density, and a Tafel slope of 32 mV/dec in 1 M KOH electrolyte.

1.3 Dissertation Objectives and Outline

The main goal of this thesis research is to develop and apply experimental and computational techniques that can be used to improve hydrogen production from solar powered water electrolysis systems.

In Chapter 2, experimental and theoretical techniques are developed and applied to investigate the kinetics and mechanism of the HER and OER on NiFe LDH active electrodes. The reaction rate constants are identified as a result of this analysis, and a detailed examination of the reaction mechanism controlling each half cell reaction is performed. Unlike most studies that focus on either the HER or OER, we present a complete system kinetics investigation by combining results obtained from the anode and cathode to fit the electrochemical cell experimental data.

In Chapter 3, we apply the electrolysis cell model identified in Chapter 2 to design and optimize an integrated electrolysis-solar energy-battery system. The primary objective is to present computational tools that can be applied to identify the optimal system configuration required for maximum hydrogen production and minimum system cost. The model is simulated over a one year timescale to ensure both diurnal and seasonal weather variations are included.

In Chapter 4, we extend the effect of cloud cover shading to address performance mismatch between individual cells in the PV module. We present computational tools to understand the effect of cell mismatch (caused by partial shading) on the PV module performance. The primary goal is to identify the optimal number of bypass diodes in the PV module necessary to maximize performance and minimize

added costs.

Chapter 5 presents concluding remarks of this work and suggestions for future work.

Chapter 2: Kinetics of OER and HER on NiFe LDH

2.1 Introduction and Background

OER and HER are among the most frequently studied reactions in electrochemistry. This can be mainly because understanding the OER and HER kinetics and mechanism is important for numerous renewable energy applications such as fuel cells and hydrogen production from water electrolysis [19].

Optimizing electrocatalytic activity requires reaching the highest possible current density at the lowest possible applied potential. Hence, optimal catalysts are ones characterized with low overpotential, low Tafel slope, and good stability and resistivity to corrosion in electrolytes. Overpotential is defined as the difference between the applied potential and the equilibrium reaction potential. Lower overpotential values means that the catalyst is more capable of producing higher amounts of hydrogen or oxygen gases at lower applied voltage. Since overpotantial is a function of the operating current density, it is commonly reported at a current density of 10 mA/cm^2, enabling easy comparison between different electrodes reported in the literature.

Tafel slope is an important definition in electrochemistry, which provides a measure of the sensitivity of the electrode's activity towards an increase in the

applied potential. It is usually reported in the units of mV/dec, indicating how much voltage is required for a decade increase in the current. Hence, the lower the Tafel slope, the more the current increases with rising applied voltage. The Tafel slope also provides valuable information about the reaction mechanism and the rate determining step of the overall half-cell reaction [20].

Studying the relation between the reaction kinetic parameters, reaction mechanism, adsorbed species coverage, and the overpotential has been the focus of numerous research articles [19]. Different characterization experiments have been used to reveal valuable insight into the electrochemical reaction kinetics and mechanism. Among them -which are of interest to this work- are Linear Sweep Voltammetry (LSV) and Electrochemical Impedance Spectroscopy (EIS).

LSV involves measuring the current while the potential of the working electrode is swept linearly with time with respect to a reference electrode. Tafel plots can be used to interpret the LSV data, in which the natural logarithm of the current is plotted against the potential. To obtain more accurate kinetic data and Tafel slope values, the effect of the uncompensated solution resistance should be eliminated. Since the voltage is generally applied between the working and the reference electrodes, a fraction of it will be dissipated due to solution resistance depending on the cell geometry and type of electrolyte used. This is typically referred to as the IR drop, which can be corrected either during the experiments (some instruments have the IR drop correction option) or after the experiment when the value of the solution resistance is known or can be calculated or measured. EIS experiments have the advantage of measuring the solution resistance between the working and

the reference electrode.

EIS involves the application of a small potential or current perturbation to assure the pseudo linearity in the cell's response. Hence, for a sinusoidal potential perturbation, the output current also will be sinusoidal and have the same frequency, but with a phase shift. The magnitude of the impedance and the phase change are determined from the potential perturbation and its current response. The EIS results are normally reported as a Nyquist plot, where the imaginary part of the impedance is plotted against the real part, or as a Bode plot, where the phase shift angle and impedance magnitude are plotted against the frequency. The EIS data can be analyzed to find the equivalent electrical circuit diagram components, including resistors, capacitors, and inductors, and hence reveal valuable information about the electrode kinetics.

To obtain the electrode overpotential value, a galvanostatic polarization test is performed in which the current is kept at a fixed value of 10 mA/cm^2, and the potential is allowed to reach steady state for a period of time. The standard equilibrium reaction then can be subtracted from the measured potential to yield the electrode overpotential.

2.1.1 Literature Review

Numerous efforts have been made to investigate the kinetics of OER and HER on a range of promising catalyst materials. Krstajic et al [21] used the combination of classical steady-state voltammetry and impedance spectroscopy to understand

the HER mechanism on Ni electrodes in an alkali medium. They demonstrated that at low overpotential values the HER proceeds with a combination of a Volmer step, followed by a rate-controlling Tafel step. The mechanism at higher overpotential, however, was shown to be a consecutive combination of a Volmer step followed by a rate controlling Heyrovsky step. Nevertheless, in their model, the authors neglected the backward reactions of the Heyrovsky and Tafel steps in some parts of the model to simplify the calculations.

Azizi et al [19] investigated the kinetics and mechanism of HER on tin in an acidic electrolyte. The resulted kinetic model demonstrate that at lower potential range, the HER mechanism starts with a Volmer step, followed by parallel Tafel and Heyrovsky steps. At higher negative potential range, they concluded that the HER proceeds via a Volmer-Heyrovsky mechanism with the Volmer step being rate controlling. The Tafel slope value measured in this potential range was -126 mV/dec, which is in agreement with the Volmer step being rate controlling. Similar to Krstajic and coworkers [21], Azizi and coworkers made similar assumptions in neglecting the backward reaction rates of the Tafel and Heyrovsky in some parts of the model.

For the OER, the mechanism is much more complex since it is a multi-step reaction pathway involving multiple adsorbed species. Hence, it is generally more challenging to investigate the kinetic and mechanism of OER. Doyle et al [22] examined the OER kinetics on hydrous iron oxides in a basic electrolyte. In low overpotential region, the reported Tafel slope values were found to be 40 and 60 mV/dec under different oxide growth conditions. They indicated that these values of Tafel slope are typically associated with the formation of the adsorbed peroxide

(HOO) or the peroxo (OO) surface species being the rate limiting step.

Hu and coworkers [23] performed a kinetic analysis of Ir-Ta mixed oxide electrodes for the OER in acidic electrolyte. The authors made a few assumptions to simplify the model. Only the surface coverage of OH is considered as state variables, and hence, was used in the kinetic model. Additionally, the backward reaction rates of some of the mechanism steps were neglected. As a results, among the six reaction rate constants included in the kinetic model, only three were identified and are reported in their work.

Garcia-Osorio et al [24] evaluated the electrocatalytic behavior of inactive materials towards OER. They demonstrated in the materials they studied a Tafel slope greater than 100 mV/dec, suggesting that the rate controlling step is associated with the generation of adsorbed hydroxide species. This also indicates the inactivity of these materials towards OER, since an active catalyst would typically result in Tafel slope values ranging from 30 to 80 mV/dec. The authors proposed a six-step OER mechanism, however, they neglected the backward reaction rate of the last step in the mechanism. From their derived kinetic model, the reaction rate constants were identified as a result of fitting experimental and theoretical EIS data.

In practice, the efficiency of water electrolysis is limited by the large anodic overpotential of the OER. Over the last few decades, considerable research effort has been dedicated to the design and synthesis of new anodic materials with greater electrocatalytic activity relative to conventional, low Earth-abundant noble metals [25]. Among these new anodic materials are transitional metal based materials which offer high catalytic activity and low cost.

Nickel-Iron Layered Double Hydroxide (NiFe LDH) and other transition metal layered materials have attracted enormous attention owing to their high electrocatalytic activity toward both OER and HER [7], as well as their low cost, simple preparation methods, and Earth abundance [9]. Layered double hydroxides are positively charged Brucite like layers that consist of metal (divalent or trivalent) hydroxides, with an interlayer space consisting of anions, such as CO_3^{2-} or NO_3^- [9], [10]. Nickel is known to be an active material that resists corrosion better than other transition metals [26]. In addition, NiFe LDH can be deposited on Ni foam, and the resulting electrode can be used for OER and HER applications as it offers high electrocatalytic activity towards both catalytic reactions in an alkaline electrolyte [7]. Although it is not the optimal catalyst for the HER, it offers economic benefits arising from the use of the same material for both electrodes while maintaining high catalytic activity [16].

Lu et al [9] examined the electrocatalytic activity of NiFe LDH electrode towards OER in an alkaline electrolyte. Their electrode demonstrated a Tafel slope of 50 mV/dec and an overpotential of 280 mV to achieve a current density of 30 mA/cm^2. Luo et al [7] reported the performance of NiFe LDH films, with overpotentials of 240 and 210 mV towards the OER and HER, respectively, at a current density of 10 mA/cm^2. Fan et al [11] reported an active Nickel-Vanadium monolayer double hydroxide for OER, with a Tafel slope of 50 mV/dec and an overpotential of 300 mV at 10 mA/cm^2, which is comparable to, but does not exceed, the best-performing NiFe LDH reported in the literature.

2.1.2 Motivation and Goals

Understanding the mechanism of the oxygen evolution reaction (OER) and hydrogen evolution reaction (HER) is a fundamental step toward optimizing electrocatalytic activity, which is essential for optimal process design and operations [27]. Integrating a classical steady-state polarization technique with electrochemical impedance spectroscopy has shown to be effective in providing kinetic analysis of electrochemical reactions [25].

In this chapter, we investigate the mechanism and kinetics of both OER and HER on NiFe LDH material. A schematic diagram of the water electrolysis cell considered in this work is shown in Figure 2.1. We combine the results from analysis of linear sweep voltammetry (LSV) and electrochemical impedance spectroscopy (EIS) to reveal valuable insight into the reaction mechanism occurring on each electrode. We consider all the forward and backward reaction rates of the OER and HER when deriving the kinetic model, which yields a better approximation of real life operation. Unlike most studies that focus on either OER or HER, we present a complete system kinetics investigation by combining results obtained from the anode and cathode to fit the electrochemical cell experimental data. The results from this work have great promise and will be used in the following work for the process design and operation of an integrated electrolysis-solar energy system.

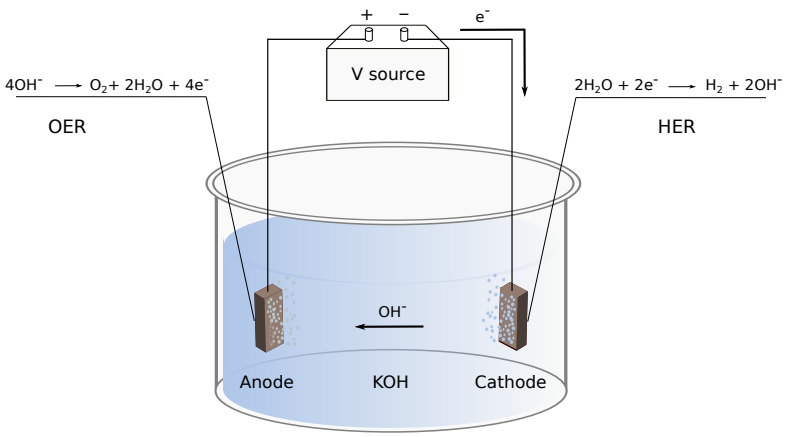

Figure 2.1: A schematic diagram of the water electrolysis cell, showing the OER and HER half cell reactions in alkaline media.

2.2 Experimental Electrode Synthesis

The NiFe LDH films were deposited on Ni foam substrates via a simple one-step hydrothermal synthesis in an autoclave reactor. Ni foam substrates (2×1 cm) were cleaned with concentrated HCl solution for 10 minutes, followed by deionized water and ethanol each for 10 minutes in an ultrasonic bath. 0.32 g of $Ni(NO_3)_2{\cdot}6H_2O$, 0.45 g $Fe(NO_3)_3{\cdot}9H_2O$ and 0.67 g urea were mixed in 80 ml deionized water until dissolution [9]. The Ni foam substrates were placed against the wall of a 100 ml autoclave, and the solution was poured into the autoclave. After allowing 12 hours of growth in an electric oven at 155 °C, the autoclave was allowed to cool naturally to room temperature, and the samples were washed with deionized water followed by ethanol, and dried at 80 °C for 6 hours. Figure 2.2 shows a graphical representation of the deposition process, and the results are shown in Figure 2.3.

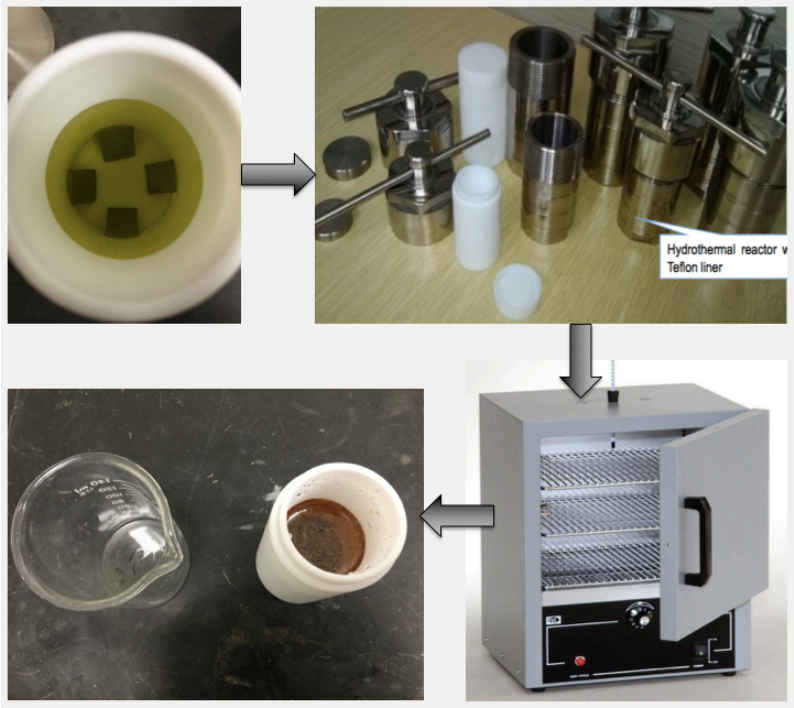

Figure 2.2: NiFe LDH deposition process on Ni foam substrates.

2.3 Deposited Film Characterization Experiments

The size and morphology of the deposited NiFe LDH samples were characterized using a Hitachi SU-70 FEG field-emission scanning electron microscopy (SEM) operating at 10 kV. SEM images of pure Ni-foam and NiFe LDH film deposited on Ni foam are shown in Figure 2.5. The morphology shown in Figure 2.4(e) and Figure 2.4(f) is in agreement with that described in previous work [9], which suggests a 3D vertical growth of LDH nanoplates on the Ni surface and a mesoporous structure of the LDH material. The LDH nanoplate average size is estimated to be 400 nm (Figure 2.4(f)).

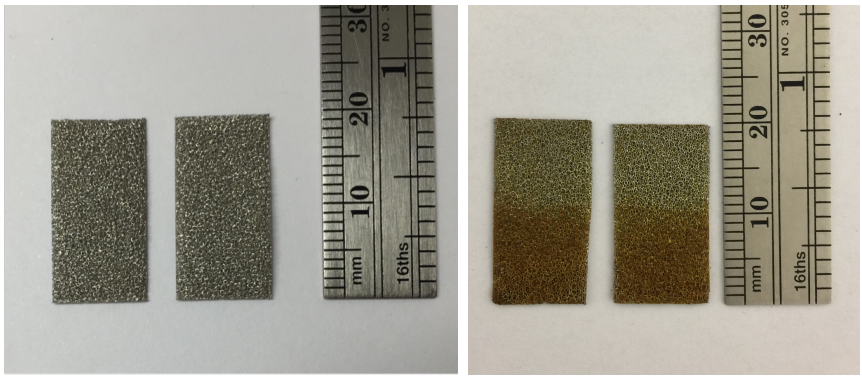

(a) Before (b) After

Figure 2.3: Ni foam substrate before (a), and after the film deposition (b).

In addition, X-ray photoelectron spectroscopy (XPS) data were collected with a Kratos Axis 165 operating in hybrid mode using Mg Kα X-rays (240 W). The use of Mg Kα X-rays was essential to detect the low concentrations of Fe in the sample and to overcome the total overlap of Fe 2p with the very intense Ni LMM that would have occurred if using the normally preferred monochromatic Al source. For the binding energy calibration, the C1s peak at 284.8 eV was used as a reference. Charge neutralization was required to minimize sample charging. Survey spectra and high resolution spectra were collected at pass energies of 160 eV and 40 eV, respectively.

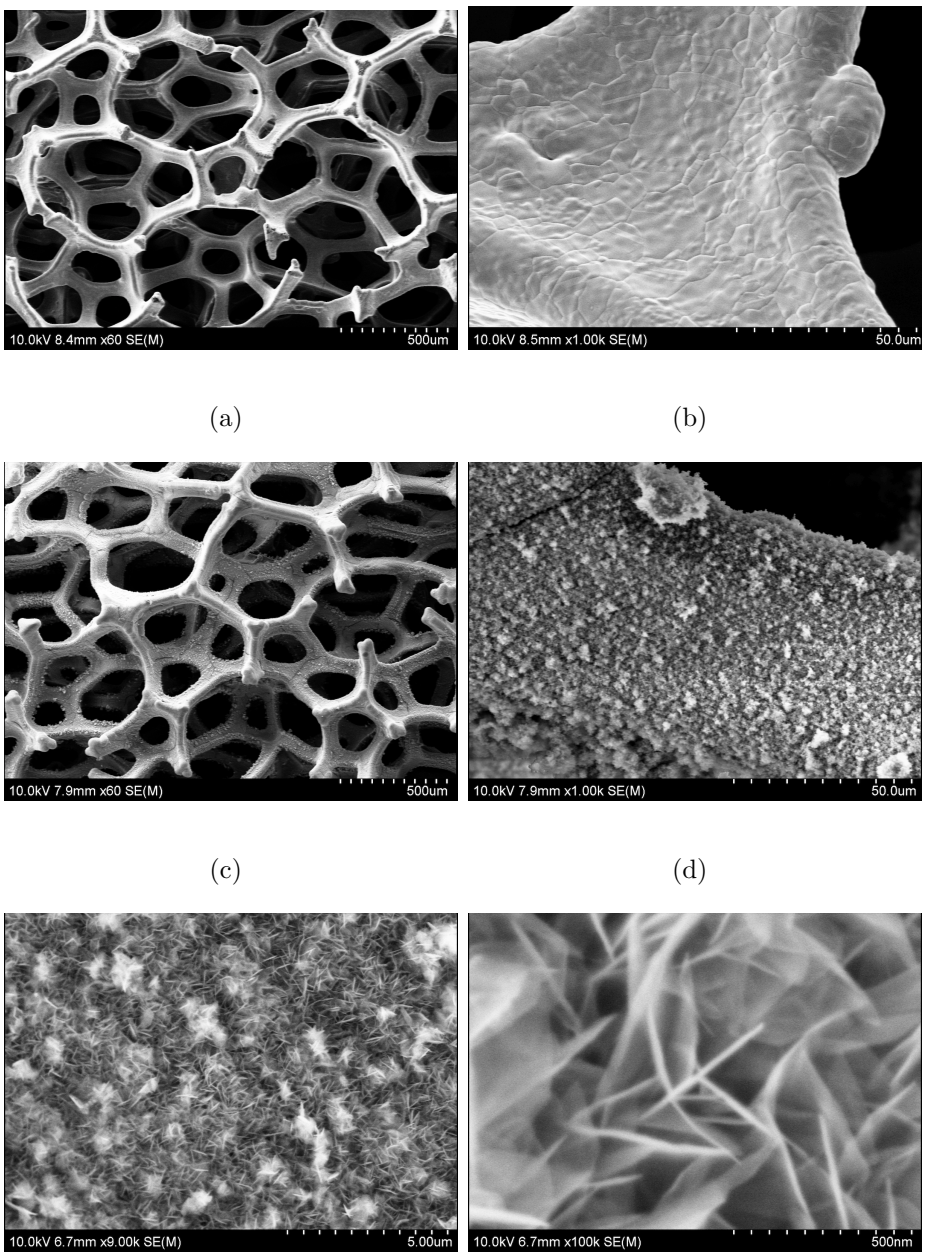

Figure 2.4: SEM images of pure Ni foam (a) and (b), and NiFe LDH deposited on Ni foam (c), (d), (e), and (f).

XPS data were analyzed using CASAXPS, quantification was performed after application of a Shirley background taking into account relative sensitivity factors from the Kratos vision Library and instrument transmission function. Quantification of the iron was complicated by overlap of the Fe 2p with the O KLL Auger, while only the $2p_{1/2}$ spin-orbit split components were overlapping, we could not use the 3/2 components alone to estimate peak area since the 3/2 and 1/2 components also overlap. The iron concentration was estimated using a constrained peak fit, using 3 spin orbit split components with spin-orbit splitting fixed at 13.4 eV and area ratio of 2:1 for the 3/2, 1/2 components, respectively, in accordance with quantum mechanics. In addition, peak FWHMs and relative area ratios of the three sets of components were fixed, the Shirley background was then adjusted at the high binding energy side until both the 3/2 and 1/2 peaks fit the data well.

XPS results (Figure 2.5(a)) show the presence of Ni, Fe, C, and O elements in the sample, with an estimated ratio of Ni/Fe of about 85.2:14.8. We also noticed by comparing the XPS results of samples prepared at different temperature that the ratio of Ni to Fe increases as the synthesis temperature decreases, with an estimated Ni:Fe ratio of about 95.5:4.5 at 128 °C (Figure 2.5(b)).

X-Ray Diffraction (XRD) patterns of NiFe LDH on Ni foam substrate were collected on a Bruker C2 Discover diffractometer using a Cu Kα source. Spectra were collected using a 2D Vantec detector in the range from 8.8 °to 85.6 °. XRD results in Figure 2.6 show the LDH reflection peaks of (003), (006), and (009), which represent the behavior of a typical LDH phase, and is in agreement with that reported in the literature [7], [9], [10].

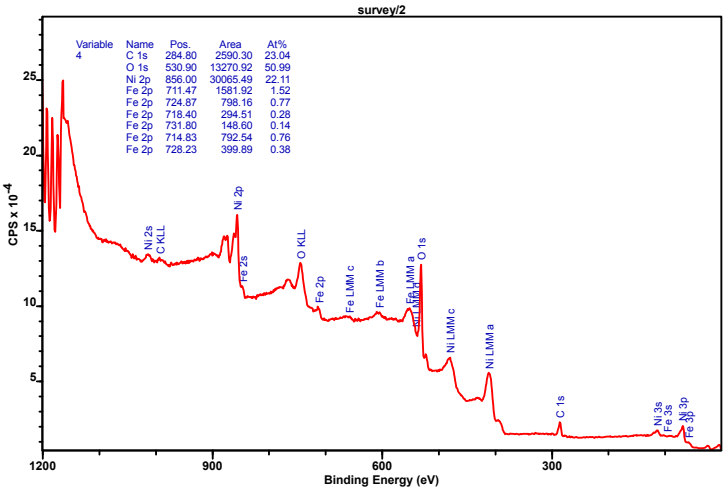

(a)

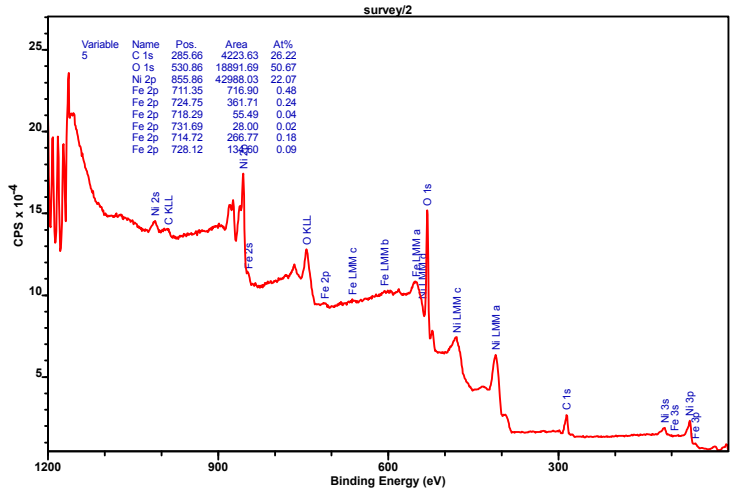

(b)

Figure 2.5: XPS results for NiFe LDH at 155 °C (a), and 128 °C (b).

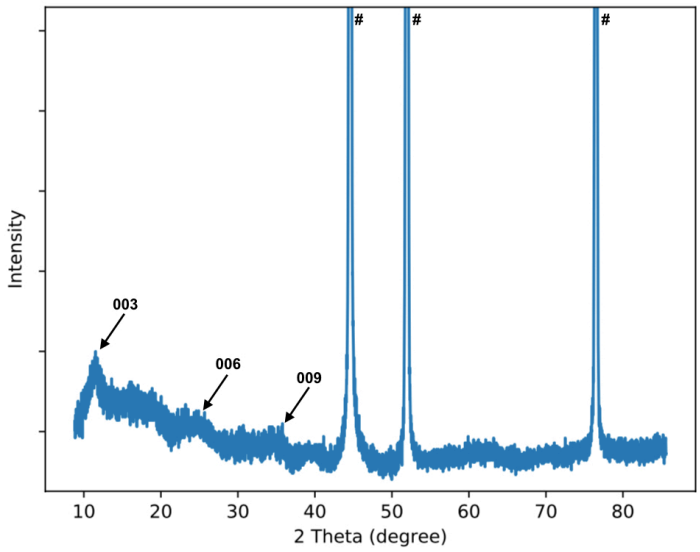

Figure 2.6: XRD characteristics of NiFe LDH deposited on Ni foam substrate. The peaks marked # represent the Ni foam substrate.

2.4 Electrochemical Measurements

A conventional three-electrode electrochemical cell was used for the measurements with 1 M KOH solution as an electrolyte. The reference electrode chosen was CH Instruments Alkaline/Mercury Oxide (Hg/HgO/1M NaOH, 0.098 V vs NHE at 25 °C).

A GAMRY interface 1000E potentiostat was used to perform the electrochemical measurements. LSV data were obtained for the cathode (HER electrode) at the applied potential range -0.93 to -1.7 V vs Hg/HgO, and for the anode (OER electrode) between the applied potentials 0.48 to 0.93 V vs Hg/HgO reference electrode, with a scan rate of 1 mV/s and a step size of 10 mV. EIS measurements were taken at different potentials within the LSV potential range. EIS data were

obtained in the frequency range 0.1 to 1×10^5 Hz, with an alternating AC voltage of 10 mV. The voltage drop corresponding to the uncompensated solution resistance was determined from the measurements using the impedance results, and all data presented in this work are corrected for the IR drop. For the combined electrolysis cell measurements, LSV data were obtained using a two-electrode cell set up with the potential range of 1.36 to 2.5 V applied between the anode and cathode.

2.5 NiFe LDH Performance as an HER Electrode

2.5.1 Electrochemical Characterization Results and Analysis

The HER mechanism starts with an electrochemical adsorption of a water molecule onto an active site on the cathode to produce the adsorbed species H (a step that is typically referred to as the Volmer step). The hydrogen gas can then be produced from two competing reaction paths: a chemical recombination of the adsorbed species H (Tafel step), and an electrochemical desorption step (Heyrovsky step). The HER mechanism is presented in Table 2.1.

Figure 2.7 represents a galvanostatic polarization test performed at a current density of -10 mA/cm^2, which reveals a potential of -1174 mV. Combining this value with the HER equilibrium potential of -829 mV vs NHE (equals to -927 mV vs Hg/HgO), the deposited film reported a cathodic overpotential of 247 mV at a current density of 10 mA/cm^2 toward the HER. This value is higher than the 210 mV overpotential reported by Luo et al [7], yet lower than the 269 mV overpotential demonstrated by Chen et al [17].

Table 2.1: HER mechanism in a basic electrolyte [21]. S_{HER} represents active sites on the HER electrode. Electrons are denoted by e^-, and the subscripts (aq) and (g) denote the aqueous and the gas phases, respectively.

Volmer:	$H_2O_{(aq)} + S_{HER} + e^-$	$\rightleftharpoons$	$H + OH^-_{(aq)}$
Heyrovsky:	$H + H_2O_{(aq)} + e^-$	$\rightleftharpoons$	$H_{2(g)} + S_{HER} + OH^-_{(aq)}$
Tafel:	$2H$	$\rightleftharpoons$	$H_{2(g)} + 2S_{HER}$

Aside from providing valuable information on the catalyst activity toward an electrochemical reaction, the Tafel slope can offer valuable insight into the reaction mechanism. An experimental Tafel plot constructed from the LSV data (Figure 2.8) shows two distinct Tafel slopes with values of 38.4 and 71.3 mV/dec at lower and higher potential regions, respectively, demonstrating high electrocatalytic activity of the prepared film. A change in Tafel slope with increasing potential can be attributed to a reaction mechanism or pathway change, or to the changes in the surface coverage of intermediates [27]. It is well accepted in the literature that a Tafel slope close to 120, 40, or 30 mV/dec indicates that the HER mechanism is controlled by Volmer, Heyrovsky, or Tafel steps, respectively [27], [28], [29]. Hence, the Tafel slope value of 38.4 mV/dec reported in this work suggests that the Heyrovsky step is rate controlling. However, it will be difficult to draw a definitive conclusion about the mechanism based on the 71.3 mV/dec value observed in the high potential region since it is not a conventional value for the HER. Further investigation of the reaction mechanism is discussed in section 2.5.2.

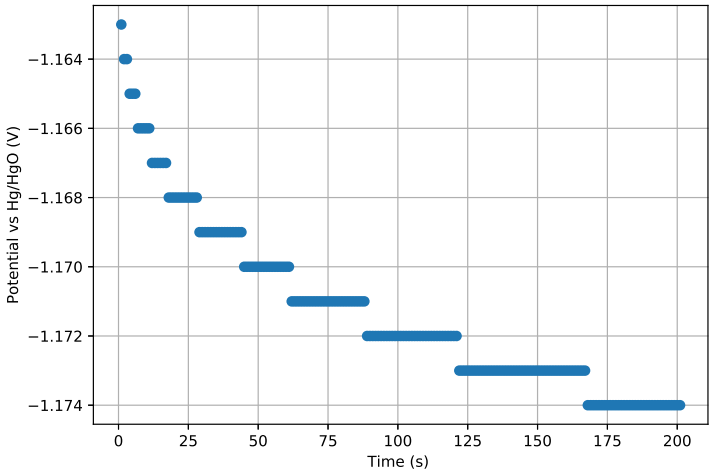

Figure 2.7: Galvanostatic polarization test performed for the HER electrode at a current density -10 mA/cm^2.

To gain a better insight into the kinetic mechanism that governs the HER, EIS measurements were taken at different values within the LSV potential range. Figure 2.9 shows the Nyquist plots of the EIS measurements in the form of semi-circle shaped spectra. The diameter of the semi-circle decreases as the applied potential increases, indicating increasing HER activity. The intersection of the spectra with the real impedance axis at the high frequency range represents the ohmic resistance, mainly caused by the electrolyte resistance. The high frequency region of HER Nyquist plots shows a straight line or a deformed semi-circle behavior, which can be attributed to the porous structure of the active catalyst [30], and is in agreement with the SEM results presented earlier.

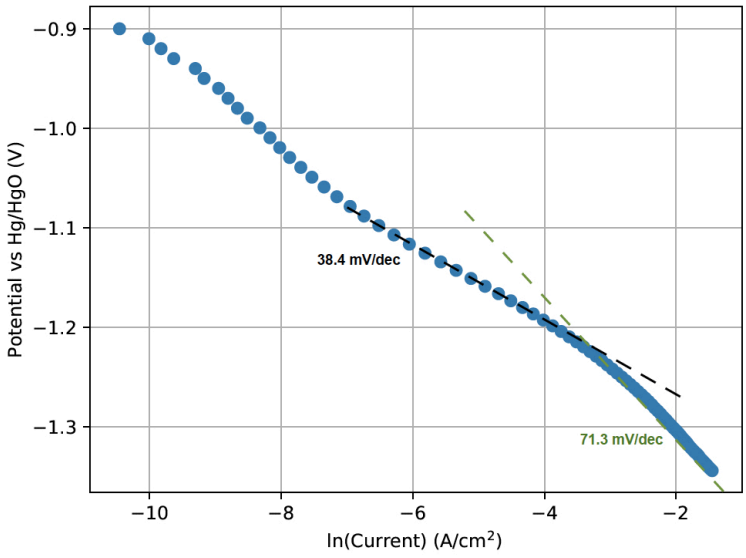

Figure 2.8: Tafel plot for NiFe LDH as a HER electrode showing two Tafel slopes at low and high potential regions.

The choice of the equivalent electric circuit representing the EIS spectrum is crucial in the model. Theoretically, several different circuits can provide a good fit to the EIS spectrum, but do not necessarily describe the physical phenomena of an electrochemical system [31]. As such, it is helpful to conduct a literature review to have a preliminary perception on the mechanism occurring on the electrode, in addition to performing structural and morphological characterization experiments of the electrode, such as SEM [31]. It is well known in the literature that Armstrong and Henderson equivalent electric circuit is well suited to provide a valid physical interpretation of the HER mechanism [19], [21], [32]. As such, the impedance results were interpreted by fitting the data to an Armstrong and Henderson equivalent electric circuit (Figure 2.10) using both Z-view software and EIS Spectrum Analyser to obtain the equivalent circuit components.

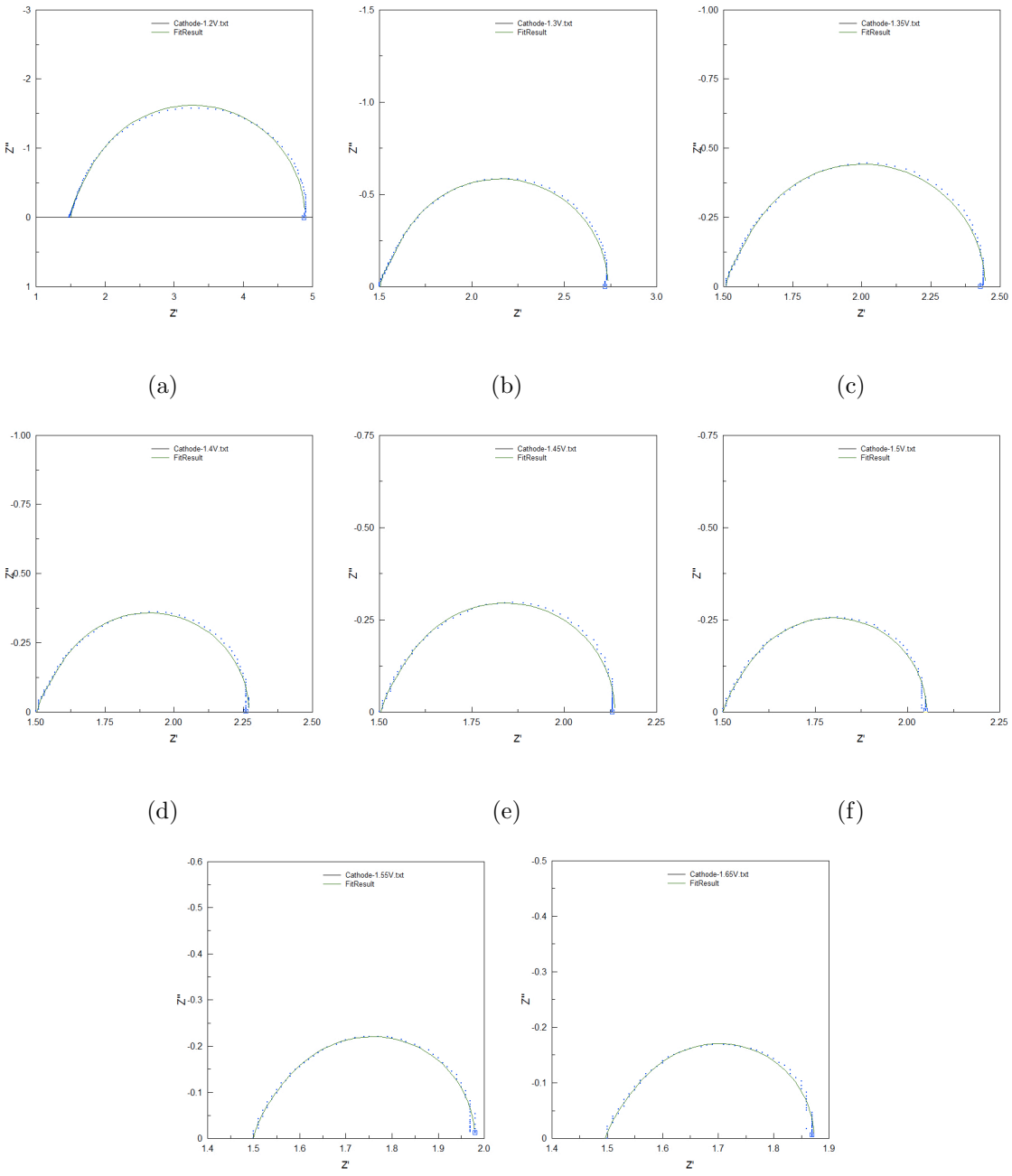

Figure 2.9: Nyquist plots of EIS measurements obtained for the HER at -1.2 V (a), -1.3 V (b), -1.35 V (c), -1.4 V (d), -1.45 V (e), -1.5V (f), -1.55 V (g), and -1.65 V (h) vs Hg/HgO.

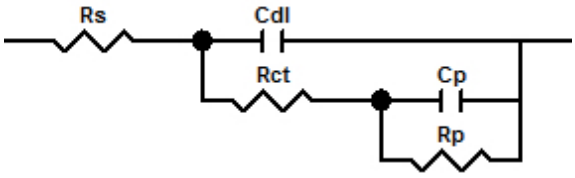

Figure 2.10: Armstrong and Henderson equivalent electric circuit.

In Figure 2.10, R_s is the ohmic electrolyte resistance measured between the working and the reference electrodes, C_{dl} is the double layer capacitance formed at the electrode/electrolyte interface, R_{ct} is the reaction charge transfer resistance across the electrode/electrolyte interface, and R_p and C_p are the pseduo-resistance and pseduo-capacitance related to the adsorption, desorption and mass transfer limitations of the adsorbed species H at the working electrode [21], [32]. The R_p and C_p are also associated with the relaxation of the adsorbed hydrogen surface coverage as the applied potential changes, with a relaxation time constant $\tau = R_p C_p$ [33]. To obtain a better fit, an inductor was connected in series to the Armstrong and Henderson circuit, which may account for the cell wires and connection contributions at high frequencies.

Z-view software provides a wide variety of built-in or user-defined equivalent circuit models. The fitting results provide error % confidence interval estimates for each component in the electric circuit, as well as general "goodness of fit" measurements, such as Chi-squared and sum of squares. The Chi-squared is the square of the standard deviation between the original experimental data and the fitted theoretical spectrum [34]. The sum of squares is proportional to the average percentage error between the experimental EIS spectrum points and the calculated values [34].

In this work, all the EIS fitting results for the HER and OER reported Chi-squared values of less that 7×10^{-4}, and a low sum of squares value confirmed by the low error % of the individual electric circuit components. This suggests the excellent fit between experimental and fitted EIS spectrum, which is also confirmed by the excellent fit shown in the EIS Nyquist plots (Figure 2.9 and Figure 2.16).

The EIS fitting results for the HER are shown in Figure 2.9 and Table 2.2. It can be seen that the solution resistance is nearly constant, while both the charge transfer and the psudo-resistances decrease exponentially as the applied voltage increases, a result that is confirmed by the decrease in the semi-circle diameters of Figure 2.9.

2.5.2 HER Theoretical Analysis

The electrochemical reaction rate expressions for the Volmer, Herpvsky, and Tefel steps are given in Equations (2.1), (2.2), and (2.3), respectively [21]. In these rate expressions, Θ_{H} is the fraction of the surface coverage of the adsorbed intermediate H, k_i' is the electrochemical rate constant (mol $\mathrm{cm}^{-2}\mathrm{s}^{-1}$), k_i is the chemical rate constant (mol cm^{-2} s^{-1}), k_i^o is the partial standard chemical rate constant (cm s^{-1}), β_i is a symmetry factor, assumed to be 0.5, and η is the overpotential (V).

$$\nu_V = k_V'(1 - \Theta_{\mathrm{H}}) - k_{-V}'\Theta_{\mathrm{H}} \tag{2.1}$$

$$\nu_H = k_H'\Theta_{\mathrm{H}} - k_{-H}'(1 - \Theta_{\mathrm{H}}) \tag{2.2}$$

$$\nu_T = k_T\Theta_{\mathrm{H}}^2 - k_{-T}(1 - \Theta_{\mathrm{H}})^2 \tag{2.3}$$

Table 2.2: EIS fitting results to the Armstrong and Henderson equivalent electric circuit for the HER, and the corresponding relative errors.

V (V)	R_{s} (Ω)	R_{ct} (mΩ)	R_{p} (mΩ)	C_{dl} (μF)	C_{p} (μF)	L (μH)
-1.20	1.509 ± 0.2	1072 ± 5.9	2308 ± 2.8	171.6 ± 2.0	159.5 ± 2.7	0.09 ± 25.7
-1.30	1.498 ± 0.3	304.3 ± 8.7	933.7 ± 3.2	107.1 ± 6.7	140.5 ± 2.6	0.22 ± 11.1
-1.35	1.501 ± 0.3	267.7 ± 9.9	676.9 ± 4.5	103.5 ± 7.8	136.7 ± 2.6	0.21 ± 11.1
-1.40	1.492 ± 0.4	255.6 ± 8.4	552.2 ± 4.3	89.6 ± 9.3	141.1 ± 2.5	0.24 ± 9.8
-1.45	1.489 ± 0.4	205.8 ± 8.7	441.4 ± 5.2	87.1 ± 10.1	141.0 ± 2.4	0.29 ± 8.2
-1.50	1.483 ± 0.4	191.8 ± 7.4	376.8 ± 5.3	81.6 ± 11.3	149.6 ± 2.3	0.30 ± 8.3
-1.55	1.485 ± 0.3	206.4 ± 6.8	287.5 ± 6.1	91.5 ± 7.5	166.6 ± 3.9	0.28 ± 6.2
-1.65	1.469 ± 0.5	158.9 ± 4.8	245.3 ± 5.9	67.3 ± 14.2	170.9 ± 2.4	0.33 ± 7.2

where:

$$k_i' = k_i \exp\left(\frac{-\beta_i F\eta}{RT}\right) = k_i^o [H_2O] \exp\left(\frac{-\beta_i F\eta}{RT}\right), i = V, H$$

$$k_{-i}' = k_{-i} \exp\left(\frac{(1-\beta_i) F\eta}{RT}\right) = k_{-i}^o [OH^-] \exp\left(\frac{(1-\beta_i) F\eta}{RT}\right), i = V, H$$

$$k_T = k_T^o$$

$$k_{-T} = k_{-T}^o \frac{P_{\mathrm{H_2}}}{P^o}$$

The steady state kinetics of the HER can be characterized by applying a charge balance. The current density can then be given as a function of the electrochemical reaction rates:

$$r_o = j/F = -(\nu_V + \nu_H) \tag{2.4}$$

For a purely charge transfer controlled process, it is reasonable to assume that the reciprocal of the charge transfer resistance can be characterized by Tafel slope. However, it is better to assume that more than one step is involved in the HER mechanism; hence, the reciprocal of the Faradaic resistance R_{F}^{-1} is a better representation of Tafel slope [21], [35]. The Faradaic resistance is defined as the sum of the charge transfer and pseudo resistances.

$$R_{\mathrm{F}}^{-1} = \left(\frac{\partial j}{\partial E}\right)_{\Theta_{\mathrm{H}}} = -F\left(\left(\frac{\partial \nu_V}{\partial E}\right)_{\Theta_{\mathrm{H}}} + \left(\frac{\partial \nu_H}{\partial E}\right)_{\Theta_{\mathrm{H}}}\right) \tag{2.5}$$

The rate of change of the adsorbed hydrogen surface coverage can be obtained by performing a material balance [19]:

$$r_1 = \frac{q}{F}\left(\frac{\partial \Theta_{\mathrm{H}}}{\partial t}\right) = \nu_V - \nu_H - 2\nu_T \tag{2.6}$$

The steady state coverage is obtained when r_1 is set to zero, facilitating the calculations of the coverage as a function of reaction rate constants. Setting r_1 to zero reveals a second order polynomial in Θ_{H}, which can be solved using:

$$\begin{aligned} \Theta_{\mathrm{H}} &= \frac{-b \pm \sqrt{b^2 - 4ac}}{2a} \\ a &= 2\left(k_{-T} - k_T\right) \\ b &= -\left(k'_V + k'_{-V} + k'_H + k'_{-H} + 4k_{-T}\right) \\ c &= \left(k'_V + k'_{-H} + 2k_{-T}\right) \end{aligned} \tag{2.7}$$

Equations (2.1), (2.2), (2.4), and (2.5) show the dependency of the current density and Faradaic resistance on the Volmer and Heyrovsky reaction rate constants, the potential, along with the surface coverage, and Equation (2.7) represents the surface coverage as a function of all six reaction rate constants, and the potential. Consequently, j and R_{F} can be theoretically represented as a function of all the reaction rate constants and the potential. A least squares procedure to fit the theoretical current density model with experimental results obtained from the steady state polarization curve is implemented using scipy.optimize.least_squares package in the Python programming environment. The cost function to be minimized is

$$\text{minimize } F(x) = 0.5 \times \sum \left(j_{i,exp} - j_{i,th}\right)^2, i = 0, ..., m-1 \tag{2.8}$$

where x is the solution set [k_V, k_{-V}, k_H, k_{-H}, k_T, k_{-T}], m is the number of experimental LSV data points, $j_{i,th}$ is the value of the current density calculated from Equation (2.4). In the least squares problem, the stopping criteria corresponds to reaching a stable solution with a tolerance of 1×10^{-12}. The value of the cost function at the optimal solution was 9.90×10^{-10}.

The chemical reaction rate constants for the individual HER mechanism steps, Tafel, Volmer, and Heyrovsky, were obtained as a result of the fitting procedure, and are shown in Table 2.3. Figure 2.11(a) demonstrates the excellent fit of the current-voltage characteristics with experimental LSV data. The identified reaction rate model shows a good agreement between theoretically calculated Faradaic resistance and values obtained from EIS results (Figure 2.11(b)).

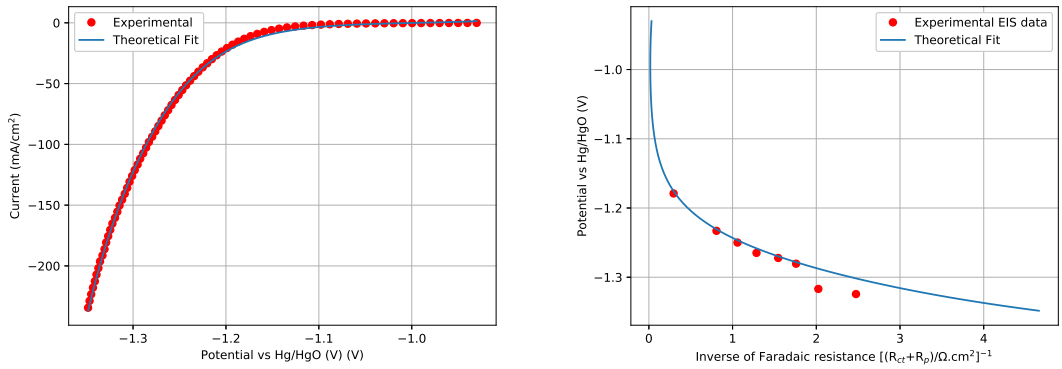

(a) (b)

Figure 2.11: Experimental and simulated results of the HER current density (a) and inverse of Faradaic resistance (b) versus potential.

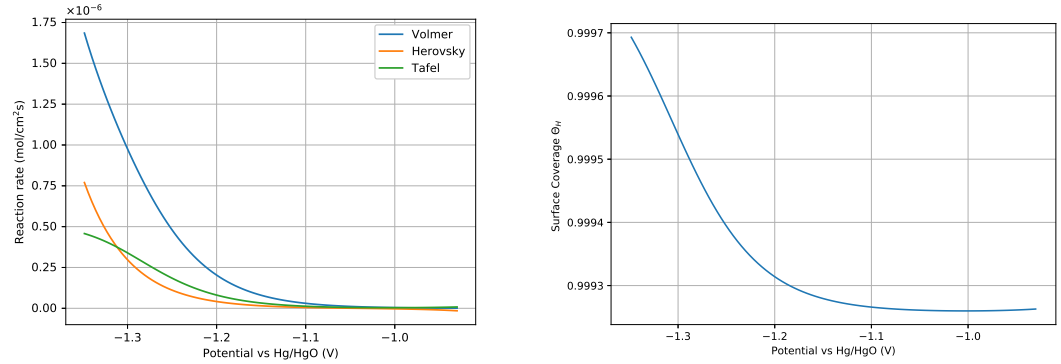

(a) (b)

Figure 2.12: Tafel, Volmer, and Heyrovsky reaction rates at the obtained kinetic parameters (a) and hydrogen fractional surface coverage (b) versus potential.

Table 2.3: Chemical rate constants k_i (mol cm^{-2} s^{-1}) and partial standard chemical rate constants k_i^o (cm s^{-1}) obtained for HER.

k_V	k_{-V}	k_H	k_{-H}	k_T	k_{-T}
1.38e-6	1.00e-10	1.94e-10	2.21e-5	5.52e-7	1.00
k_V^o	k_{-V}^o	k_H^o	k_{-H}^o	k_T^o	k_{-T}^o
2.48e-5	1.00e-7	3.48e-9	2.21e-2	5.52e-7	1.00

The set of identified reaction rate constants in Table 2.3 reveals the Heyrovsky step as the rate limiting step for the HER on NiFe LDH electrode. Figure 2.12(a) shows the calculated Tafel, Volmer, and Heyrovsky reaction rates using the identified kinetic parameters, which reveals a dependence of the HER mechanism on the potential. At low potential range (below a compensated voltage of -1.31 V, equivalent to an applied voltage of -1.52 V vs Hg/HgO), the HER mechanism starts with a Volmer step, followed by parallel Tafel and rate controlling Heyrovsky steps. At higher potential range, the HER mechanism consists of a consecutive combination of the Volmer step, followed by a rate-controlling Heyrovsky step, with negligible contribution by the Tafel step. This result is in good agreement with the Tafel slope analysis presented earlier.

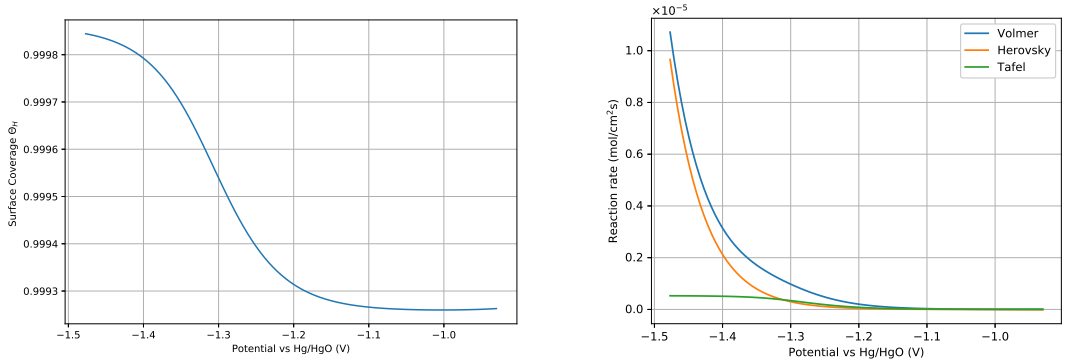

(a) (b)

Figure 2.13: Hydrogen fractional surface coverage (a) and reaction rates (b) for extended potential range.

Figure 2.12(b) shows the influence of the potential on the adsorbed hydrogen surface coverage, with a noticeable high coverage value close to unity in all potential ranges. This observation is expected since the Heyrovsky is the rate controlling step. A small increase in the coverage value is noticed with increasing potential, which is associated with the shift between Tafel and Heyrovsky reaction rate values close to -1.3 V. The Tafel step requires the presence of two adjacent adsorbed hydrogen species on the surface, resulting in an increase of the coverage as this rate become smaller. Ultimately, when the Tafel rate reaches a small negligible value, the Volmer and Heyrovsky rates approach the same value, allowing the surface hydrogen coverage to reach a stable value (Figure 2.13(a)).

When the theoretical potential range is further extended (Figure 2.13(b)) Tafel step reaction rate becomes independent of the applied potential, which can be attributed to the surface coverage of the adsorbed intermediate reaching a constant

high coverage value in this potential region. This conclusion can be drawn by examining Equation (2.3) and the definition of its rate constants being independent of potential; however, the dependency of this rate at low potential values originates from that of the surface coverage.

2.6 NiFe LDH as an OER Electrode

2.6.1 Electrochemical Characterization Results and Analysis

One of the main challenges of OER mechanistic analysis lies in its complexity, owing to the fact that it involves the transfer of four electrons through a multi-step reaction pathway in which various reaction intermediates are formed [27]. As a result, various reaction pathways were proposed for the OER. One of the better-accepted reaction pathways for the OER was proposed by Dong et al [36] on the NiFe LDH electrode and is presented in Table 2.4. The OER mechanism starts when a hydroxide ion $OH_{(aq)}$ adsorbs onto an active site on the anode, followed by a sequence of intermediate reactions to form the adsorbed species O, HOO, OO before releasing oxygen gas $O_{2_{(g)}}$ from the adsorbed species OO.

Table 2.4: OER mechanism in a basic electrolyte [36]. S_{OER} represents active sites on the OER electrode. Electrons are denoted by e^-, and the subscripts (aq) and (g) denote the aqueous and the gas phases, respectively. All remaining species correspond to adsorbed surface species.

Step 1:	$OH^-_{(aq)} + S_{OER}$	$\rightleftharpoons$	$HO + e^-$
Step 2:	$OH^-_{(aq)} + HO$	$\rightleftharpoons$	$O + H_2O_{(aq)} + e^-$
Step 3:	$OH^-_{(aq)} + O$	$\rightleftharpoons$	$HOO + e^-$
Step 4:	$OH^-_{(aq)} + HOO$	$\rightleftharpoons$	$OO + H_2O_{(aq)} + e^-$
Step 5:	OO	$\rightleftharpoons$	$O_{2(g)} + S_{OER}$

In terms of the catalytic performance towards the OER, Figure 2.14 shows a galvanostatic polarization test performed at a current density of 10 mA/cm^2, which reveals a potential of 548 mV vs Hg/HgO. Combining this value with the OER equilibrium potential of 401 mV vs NHE (equals to 303 mV vs Hg/HgO), NiFe LDH demonstrated an excellent overpotential of 245 mV to reach an anodic current density of 10 mA/cm^2. This value is comparable to the 240 mV overpotential reported by Luo et al [7], and higher than the 224 mV overpotential reported by Li et al [10].

A Tafel plot (Figure 2.15) constructed from the experimental LSV data shows a Tafel slope of 48.4 mV/dec, which is less than the 52.8 mV/dec reported by Li et al [10], and the 50 mV/dec reported by Lu et al [9], demonstrating an excellent performance of our prepared electrode.

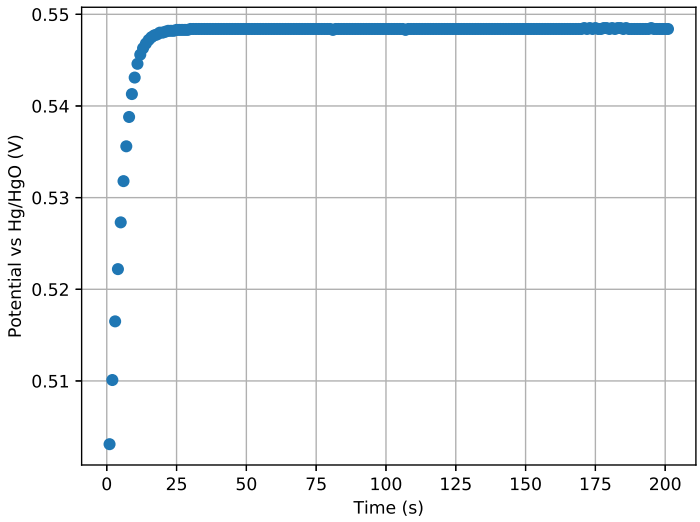

Figure 2.14: Galvanostatic polarization test performed for the OER electrode at a current density 10 mA/cm^2.

Numerous efforts have been made towards the analysis and interpretation of the Tafel slope values in terms of the OER mechanism. Doyle et al [25] suggested that either the formation of the peroxide (HOO) or the peroxo (OO) intermediates is rate limiting for a Tafel slope of 40 mV/dec on hydrous iron oxide films in basic electrolytes. Fan et al [11] indicated that the formation of HOO is rate limiting for NiV LDH with a Tafel slope of 50 mV/dec, and the formation of the O intermediate is rate limiting for NiFe LDH with a Tafel slope of 64 mV/dec. In addition, Louie et al [37] stated that a Tafel slope of 40 mV/dec is most likely associated with the formation of peroxide intermediate reaction as rate limiting.

The 48.4 mV/dec Tafel slope obtained in this work may indicate that either the formation of O, HOO or OO intermediates in steps 2, 3, and 4, respectively, is the rate determining step, with step 3 being the most probable. Further investigation

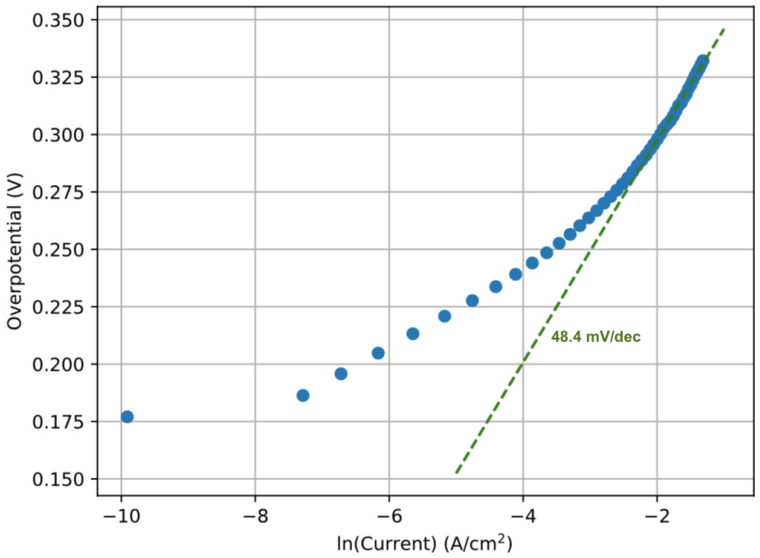

Figure 2.15: Tafel plot for NiFe LDH as a OER electrode.

of the reaction mechanism is discussed in section 2.6.2.

The OER Nyquist plots in Figure 2.16 show two distinctly identified semicircles: the former is related to the active material porous structure, arising from the resistance of the ionic conducting paths in the pores filled with the electrolyte [33]. The latter semicircle in the OER Nyquist plot is related to the charge transfer limitations in the electrode/electrolyte interface.

Figure 2.17 shows the equivalent electrical circuit used to fit the EIS spectra [38], with the fitting results given in Table 2.5. Ideally, the film porous structure resistance R_{f} should be independent of potential, however, EIS fitting results (presented in Table 2.5) demonstrated a slight decrease in the resistance of the first RC loop with increasing potential, which aids in increasing the overall OER rate as potential increase. On the other hand, R_{ct} is highly dependent on the potential, suggesting that the second RC loop is related to the charge transfer limitations.

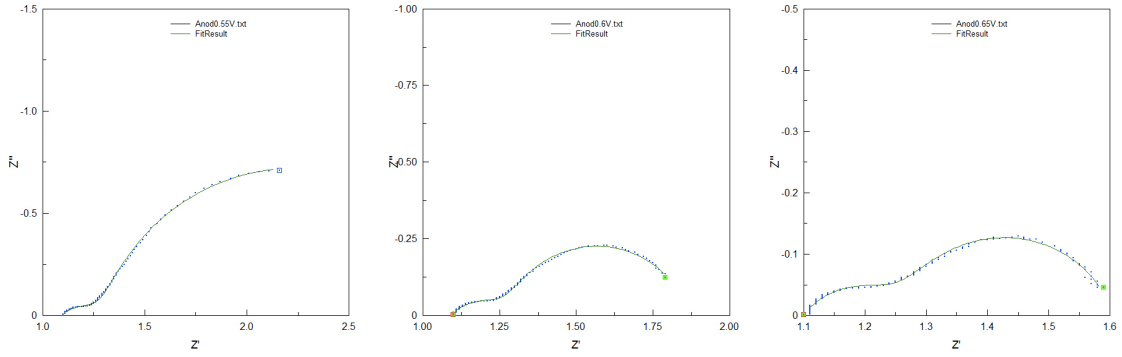

(a) (b) (c)

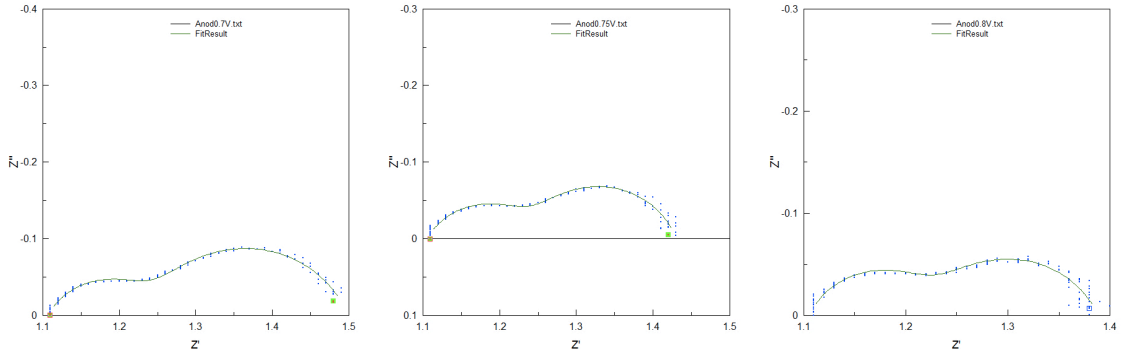

(d) (e) (f)

Figure 2.16: Nyquist plots of EIS measurements obtained for the OER at 0.55 V (a), 0.6 V (b), 0.65 V (c), 0.7 V (d), 0.75 V (e), and 0.8 V (f) vs Hg/HgO.

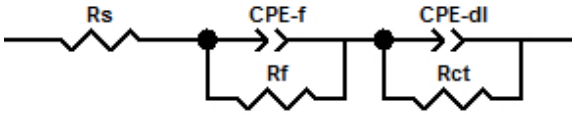

Figure 2.17: The equivalent circuit used for the OER EIS data fitting.

The constant phase element (CPE) in Figure 2.17 is introduced to improve the theoretical fit of the EIS spectra. A CPE is often used to represent a non-ideal capacitor, indicated by a depressed semi-circle behavior in Nyquist plot, which can be attributed to heterogeneities and porous surfaces [39]. The CPE contains two parameters: CPE-P corresponding to its capacitance value in the absence of frequency dispersion, and an exponent CPE-T (or α) $\leq$1, with a value of 1 for ideal capacitors [25].

When a CPE is used in a circuit, the real capacitance value can be evaluated. The capacitance associated with the film resistance C_{f} can be calculated using the common Brug equation [40], [41]:

$$C_{\mathrm{f}} = \left[CPET_{\mathrm{f}} \left(\frac{1}{R_{\mathrm{s}}} + \frac{1}{R_{\mathrm{f}}} \right)^{\alpha-1} \right]^{\frac{1}{\alpha}} \tag{2.9}$$

The double layer capacitance C_{dl} can be calculated from the modified Brug equation [supplementary information of [33]], [39] for a two-CPE equivalent electric circuit similar to Figure 2.17:

$$C_{\mathrm{dl}} = \left[CPET_{\mathrm{dl}} \left(\frac{1}{R_{\mathrm{s}} + R_{\mathrm{f}}} + \frac{1}{R_{\mathrm{ct}}} \right)^{\alpha-1} \right]^{\frac{1}{\alpha}} \tag{2.10}$$

The identified capacitance values C_{f} and C_{dl} are presented in Table 2.6.

Table 2.5: EIS fitting results to the equivalent electric circuit in Figure 2.17 for the OER and the corresponding relative errors %.

V (V)	R_s (Ω)	R_f (mΩ)	R_{ct} (mΩ)	CPE_f-T (mFs$^{\alpha-1}$cm^{-2})	α_f	CPE_{dl}-T (mFs$^{\alpha-1}$cm^{-2})	α_{dl}
0.55	1.085 ± 0.2	237.9 ± 3.8	1853 ± 1.5	329.5 ± 9.0	0.43 ± 3.5	919.1 ± 0.6	0.83 ± 0.7
0.60	1.090 ± 0.2	202.9 ± 2.9	576.2 ± 1.2	163.5 ± 9.0	0.51 ± 2.7	760.1 ± 1.0	0.82 ± 0.8
0.65	1.099 ± 0.1	173.5 ± 2.8	335.1 ± 1.5	97.6 ± 9.5	0.58 ± 2.4	693.7 ± 1.4	0.79 ± 1.0
0.70	1.107 ± 0.1	138.2 ± 2.8	254.6 ± 1.6	42.7 ± 10.4	0.68 ± 2.1	652.0 ± 1.7	0.74 ± 1.2
0.75	1.105 ± 0.1	139.2 ± 3.7	185.9 ± 2.7	42.8 ± 13.9	0.67 ± 2.9	644.6 ± 3.0	0.76 ± 1.9
0.80	1.105 ± 0.1	122.8 ± 4.2	160.6 ± 3.2	31.3 ± 15.1	0.72 ± 2.9	672.1 ± 3.6	0.72 ± 2.3

Table 2.6: Identified capacitance values obtained from EIS fitting results and Equations (2.9) and (2.10).

V (V)	C_{f} (mF)	C_{dl} (mF)
0.55	8.67	856.69
0.60	5.26	584.83
0.65	4.58	442.33
0.70	3.61	324.97
0.75	3.24	315.66
0.80	3.46	269.58

2.6.2 Theoretical Models Describing the Electrode Kinetics

For the OER, the reaction rates can be expressed as:

$$\nu_1 = k'_1\Theta_{\mathrm{S}} - k'_{-1}\Theta_{\mathrm{OH}} \tag{2.11}$$

$$\nu_2 = k'_2\Theta_{\mathrm{OH}} - k'_{-2}\Theta_{\mathrm{O}} \tag{2.12}$$

$$\nu_3 = k'_3\Theta_{\mathrm{O}} - k'_{-3}\Theta_{\mathrm{HOO}} \tag{2.13}$$

$$\nu_4 = k'_4\Theta_{\mathrm{HOO}} - k'_{-4}\Theta_{\mathrm{OO}} \tag{2.14}$$

$$\nu_5 = k_5\Theta_{\mathrm{OO}} - k_{-5}\Theta_{\mathrm{S}} \tag{2.15}$$

where:

$$k_i' = k_i \exp\left(\frac{(1-\beta_i)F\eta}{RT}\right) = k_i^o[OH^-] \exp\left(\frac{(1-\beta_i)F\eta}{RT}\right), i = 1, ..., 4$$

$$k_{-i}' = k_{-i} \exp\left(\frac{-\beta_i F\eta}{RT}\right) = \begin{cases} k_{-i}^o[H_2O] \exp\left(-\beta_i F\eta/RT\right), i = 2, 4 \\ \\ k_{-i}^o \exp\left(-\beta_i F\eta/RT\right), i = 1, 3 \end{cases}$$

$$k_5 = k_5^o$$

$$k_{-5} = k_{-5}^o \frac{P_{O_2}}{P^o}$$

Similar to the HER, the steady state current density and the inverse of Faradaic resistance of the OER can be characterized by:

$$r_2 = j/F = (\nu_1 + \nu_2 + \nu_3 + \nu_4) \tag{2.16}$$

$$R_F^{-1} = \left(\frac{\partial j}{\partial E}\right)_\Theta = F\left(\left(\frac{\partial \nu_1}{\partial E}\right)_\Theta + \left(\frac{\partial \nu_2}{\partial E}\right)_\Theta + \left(\frac{\partial \nu_3}{\partial E}\right)_\Theta + \left(\frac{\partial \nu_4}{\partial E}\right)_\Theta\right) \tag{2.17}$$

Due to the complex behavior of the OER in which various reaction intermediate species are formed, the derivation of the intermediates surface fractional coverage as a function of the reaction rate constants was challenging. To obtain expressions for the fractional surface coverage of each intermediate involved in the OER, a material balance is performed on each intermediate, with the steady state converge assumed, to obtain five algebraic equations, in which four are linearly independent:

$$\Theta_{\mathrm{S}} = \frac{\left(k'_2 + k'_{-1}\right)\Theta_{\mathrm{OH}} - k'_{-2}\Theta_{\mathrm{O}}}{k'_1} \tag{2.18}$$

$$\Theta_{\mathrm{OH}} = \frac{\left(k'_3 + k'_{-2}\right)\Theta_{\mathrm{O}} - k'_{-3}\Theta_{\mathrm{HOO}}}{k'_2} \tag{2.19}$$

$$\Theta_{\mathrm{O}} = \frac{\left(k'_4 + k'_{-3}\right)\Theta_{\mathrm{HOO}} - k'_{-4}\Theta_{\mathrm{OO}}}{k'_3} \tag{2.20}$$

$$\Theta_{\mathrm{HOO}} = \frac{\left(k'_5 + k'_{-4}\right)\Theta_{\mathrm{OO}} - k'_{-5}\Theta_{\mathrm{S}}}{k'_4} \tag{2.21}$$

Which an be solved simultaneously with:

$$\Theta_{\mathrm{S}} + \Theta_{\mathrm{OH}} + \Theta_{\mathrm{O}} + \Theta_{\mathrm{HOO}} + \Theta_{\mathrm{OO}} = 1 \tag{2.22}$$

To obtain:

$$\Theta_{\mathrm{HOO}} = m\Theta_{\mathrm{OO}} \tag{2.23}$$

$$\Theta_{\mathrm{O}} = j\Theta_{\mathrm{OO}} \tag{2.24}$$

$$\Theta_{\mathrm{OH}} = (ej - fm)\Theta_{\mathrm{OO}} \tag{2.25}$$

$$\Theta_{\mathrm{S}} = \left(c(ej - fm) - dj\right)\Theta_{\mathrm{OO}} \tag{2.26}$$

Where:

$$m = \left(\frac{a - h(bd - bce)}{1 - bcf - g(bd - bce)} \right) \tag{2.27}$$

$$j = \left(\frac{g(a - h(bd - bce))}{1 - bcf - g(bd - bce)} - h \right) \tag{2.28}$$

$$a = \frac{k'_5 + k'_{-4}}{k_4} \tag{2.29}$$

$$b = \frac{k'_{-5}}{k_4} \tag{2.30}$$

$$c = \frac{k'_2 + k'_{-1}}{k_1} \tag{2.31}$$

$$d = \frac{k'_{-2}}{k_1} \tag{2.32}$$

$$e = \frac{k'_3 + k'_{-2}}{k_2} \tag{2.33}$$

$$f = \frac{k'_{-3}}{k_2} \tag{2.34}$$

$$g = \frac{k'_4 + k'_{-3}}{k_3} \tag{2.35}$$

$$h = \frac{k'_{-4}}{k_3} \tag{2.36}$$

Substituting Equations 2.23-2.36 in 2.22 yields a single variable equation that can be solved analytically for Θ_{OO}, which can then be substituted into Equations 2.23-2.26 to obtain analytic expressions for the intermediates fractional surface coverage as a function of all reaction rate constants and the potential.

2.6.3 Evaluation of OER Rate Constants

A least squares procedure is performed to fit the theoretical current density model with experimental LSV results, and the chemical reaction rate constants for the OER are obtained (Table 2.7). The least squares problem formulation is similar

to the HER (2.8), with a cost function of 4.53×10^{-9} at the optimal solution. The resulting kinetic model shows an excellent agreement between theoretically calculated and experimental current density and Faradaic resistance values (Figure 2.18).

Table 2.7: Chemical rate constants k_i (mol cm^{-2} s^{-1}) and partial standard chemical rate constants k_i^o (cm s^{-1}) obtained for OER.

k_1	k_{-1}	k_2	k_{-2}	k_3	k_{-3}	k_4	k_{-4}	k_5	k_{-5}
2.75e-4	1.61e-8	6.80e-2	1.0e-10	1.08e-9	9.59e-1	1.16e-4	1.29e-3	2.89e-4	9.83e-1
k_1^o	k_{-1}^o	k_2^o	k_{-2}^o	k_3^o	k_{-3}^o	k_4^o	k_{-4}^o	k_5^o	k_{-5}^o
2.75e-1	1.61e-8	6.80e1	1.80e-9	1.08e-6	9.59e-1	1.16e-1	2.32e-2	2.89e-4	9.83e-1

Examining the kinetic parameters in Table 2.7 reveals that step 3, formation of the peroxide intermediate HOO, is the rate limiting step, which validates the analysis performed on the measured Tafel slope.

Since a steady state coverage of the individual reaction intermediates is assumed, it follows that the five reaction rate values are equal at any potential, with an exponentially increasing behavior similar to the current-potential characteristics, as shown in Figure 2.19(a). This is also supported by the sequential behavior of the OER, i.e. the consecutive formation of the adsorbed OER intermediates, as opposed to having two competing reaction pathways as is the case with the HER.

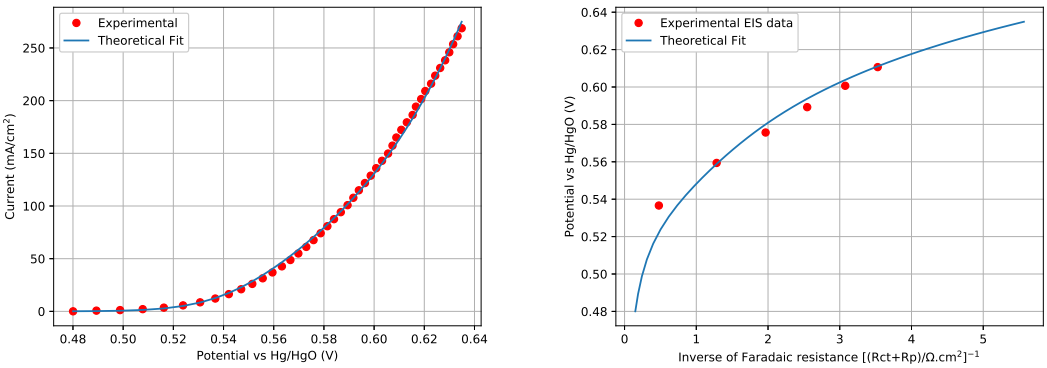

(a) (b)

Figure 2.18: Experimental and simulated results of the OER current density (a) and inverse of Faradaic resistance (b) versus potential.

A plot of the surface coverage reveals a high coverage value of the adsorbed O species that is close to unity (Figure 2.19(b)), a consequence of step 3 as rate limiting. Examining Figure 2.19(b) reveals that at higher potential, Θ_{O} begins to decrease as a result of a small increase in Θ_{OO} value. This result is reasonable owing to k_5^o value in Table 2.7 being the second smallest value compared to the remaining rate constants, and the fact that the chemical rate ν_5 is less dependent on the potential compared to the remaining electrochemical reaction rates.

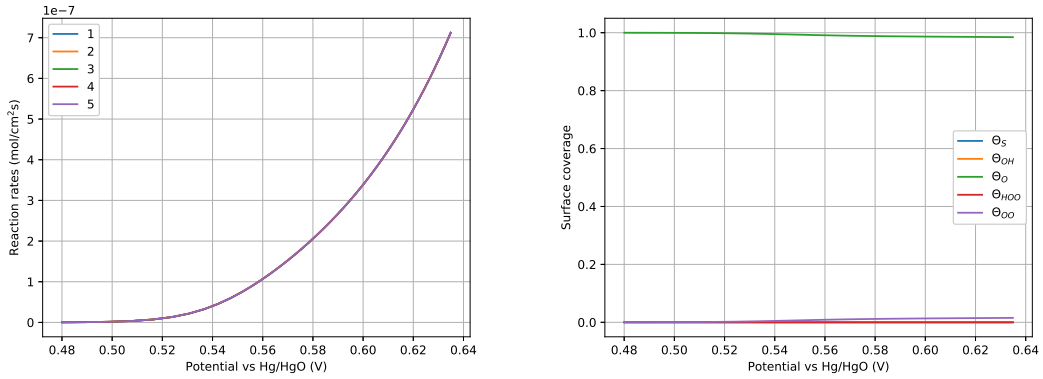

(a) (b)

Figure 2.19: OER reaction rates for the identified kinetic parameters (a) and intermediate species fractional surface coverage (b) versus potential.

2.7 Combined Electrolysis Cell Modeling

The anode and cathode kinetic results can be combined to represent the total electrolysis cell using Equation (2.37)

$$V_{\text{cell}} = 1.23 + \eta_{\text{a}} + \eta_{\text{c}} + I_{\text{cell}} \times R_{\text{cell}} \tag{2.37}$$

where η_{a} and η_{c} are the anode and cathode overpotentials, respectively, corrected for the IR drop, and R_{cell} is the total cell electrolyte resistance. R_{cell} is not the same as the two solution resistance values R_{s} obtained from the anode or cathode EIS fitting results. In fact, it can be assumed that R_{cell} is the sum of the two resistances due to the differences in the three- and two-electrode set up used in the electrochemical measurements. To illustrate, the electrolyte resistance estimated from the three-electrode cell corresponds to the solution resistance between the working and reference electrodes [42], which is approximately half the distance between the elec-

trodes in the electrochemical cell used.

Figure 2.20(a) demonstrates a good agreement between experimental cell LSV results and the current-voltage characteristics resulting from Equation (2.37) using the identified kinetic model. It can be noticed that the theoretical model deviates somewhat as the current increases, with approximately $5\%-7\%$ difference between the experimental and theoretical current value. Since the magnitude of the current deviation increases with potential, this behavior can be attributed to overestimation of the total cell solution resistance R_{cell}. If the value of R_{cell} is decreased by 5%, the theoretical results would result in a perfect fit with experimental values, as shown in Figure 2.20(b). The overestimated R_{cell} value obtained from combining the anode and cathode experimental results can be credited to the position of the reference electrode, causing a physical barrier between the two electrodes in the three-electrode cell set up. The cell LSV data, however, were measured by applying the potential directly between the anode and cathode, without the presence of the reference electrode in the cell.

The electrolysis cell characteristics reveal significant electrocatalytic activity of the prepared films towards water electrolysis. A current density of 10 and 100 mA/cm^2 can be reached at 1.7 and 2.1 V, respectively. This result is based on a 1 M KOH electrolyte resistance through a distance of approximately 3-4 cm between the electrodes. However, the commercial electrolyzers stacks have much smaller electrolyte path and higher concentrations (approximately 25-30% KOH) [6], significantly reducing the uncompensated resistance of the cell.

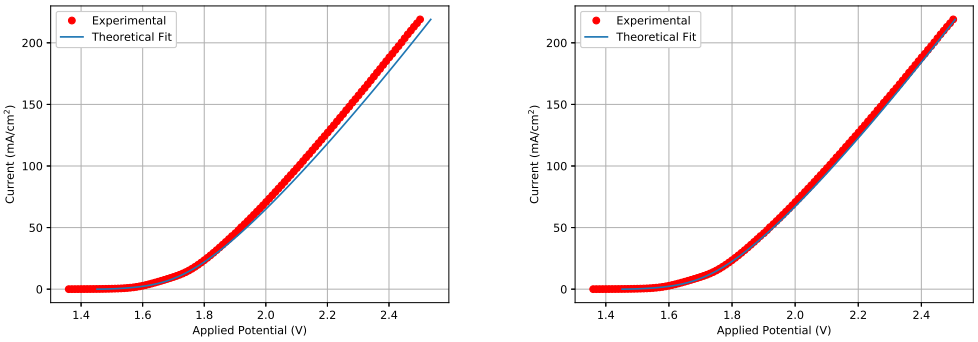

(a) (b)

Figure 2.20: Experimental and simulated cell current versus applied potential (a), and with 5% lower R_{cell} (b).

Coupling the cathode and anode kinetics results is essential for accurately predicting the total cell performance, specially when integrating the system with sustainable energy sources. Since most commercial electrolyzers operate at elevated temperatures (typically 80 °C) [43], this kinetics analysis offers an advantage of evaluating the reaction rate constants at different process design parameters, such as electrolyte concentration or temperature (by assuming exponential dependence of reactions rate constants on the temperature following Arrhenius Law).

Even though NiFe LDH demonstrated an excellent electrocatalytic activity towards OER, the electrochemical results presented in this work prove that the catalyst performance must still be enhanced toward the HER. Recent progress has demonstrated the ability to enhance the activity of NiFe LDH to reach a cathodic overpotential of as low as 29 and 34 mV at 10 mA/cm^2 by incorporating active metal atoms in the catalyst such as Ru and Ir [17], [18], allowing superior electrolysis cell performance.

2.8 Concluding Remarks

The kinetics and reaction mechanism of HER and OER on a NiFe LDH catalyst were investigated. Linear sweep voltammetry (LSV) and electrochemical impedance spectroscopy (EIS) measurements were taken, and the results were then fitted to a theoretical model relating current density and Faradaic resistance to the chemical reaction rate constants of the HER and OER.

The kinetics parameters of the HER demonstrated the Heyrovsky step as rate controlling, a result that is validated by the measured 38.4 mV/dec Tafel slope. Furthermore, the parameter fitting results reveled the dependency of the HER mechanism on applied potential. At lower end of potential range, the mechanism of HER starts with a Volmer step, followed by a parallel Tafel and rate controlling Heyrovsky step. At higher potential, the contribution of the Tafel step becomes negligible, with the mechanism being a consecutive combination of Volmer and rate controlling Heyrovsky steps. The OER kinetics demonstrated the formation of the adsorbed peroxide (HOO) as the rate determining step, which is in agreement with the 48.4 mV/dec Tafel slope observed. In higher potential regions, Θ_{O} decreases as a result of increasing Θ_{OO} value, due to the low value of k_5^o, and the fact that the chemical rate ν_5 is less dependent on the potential compared to the remaining electrochemical reactions rates.

Understanding the true kinetic behavior of a system allows for a better process design and operation control, especially when certain attributes in the process changes, such as temperature or electrolyte concentration.

Chapter 3: PV-Electrolysis-Battery Coupled System

3.1 Introduction

Generally, two primary approaches are known for solar hydrogen production: the direct use of solar energy to split water in a photoelectrochemical (PEC) cell, and photovoltaic (PV) solar cell powered electrolyzers. Currently, the latter approach is more practical because of higher solar to hydrogen (STH) efficiencies, attributable to its higher technical state of maturity [43]. In addition, PEC water splitting still faces challenges generating sufficient photovoltages while reaching acceptable STH efficiencies and demonstrating electrode material stability [43].

In this chapter, we focus on modeling and optimizing an integrated PV-electrolysis-storage battery system for optimal hydrogen production. The output of the PV module is direct current (DC) at a controlled output voltage and hence nearly insusceptible to variations in solar irradiance levels [6]. This feature is an asset to the electrolyzer design, which requires a fixed input voltage for consistent operations. The PV output current, however, is influenced by the irradiance variations, which can ultimately affect the hydrogen production rate in the electrolyzer unit. However, the operational mode of the electrolyzer is assumed to follow a fixed current mode, requiring the battery to discharge in situations in which the PV

currents are insufficient.

Fortunately, the decreasing trend in the cost of electricity produced by PV solar cells is an additional advantage for PV powered electrolysis systems [44]. In the United States, the PV system cost benchmark for commercial applications has fallen from a value of $5.36 in 2010 to $1.85 in 2017 per Watt DC [45]. In addition, the commercial scale levelized cost of energy (LCE), defined as the costs associated with producing 1 kWh of energy, has also decreased from values in the range (0.32-0.42) $/kWh in 2010, down to values between (0.09-0.12) $/kWh in 2017 [45]. This cost is expected to even reach values under 0.03 $/kWh in the future for renewable energy sources such as PV and wind [44].

For our integrated system, the PV modules provide the required energy to power the electrolyzers, while using the excess power to charge the battery during peak PV power production. The battery in return will provide the power necessary for uninterrupted operation of electrolyzers at night. Cloud cover data for College Park city in Maryland, USA is available for the year 2017. Hence, both diurnal and seasonal weather variability are included in the model, and an optimal sizing of individual system elements will be demonstrated.

The coupled system is assumed to be connected to the grid to ensure uninterrupted operation of electrolyzer during seasonal weather variations. During times where the power generated from the PV modules is insufficient to fully meet the electrolyzer and battery charge/discharge load, power will be supplied by the grid. On the contrary, excess power will be sold to grid in cases where the power generated by the PV modules exceeds the integrated system power requirements. A schematic

diagram of the coupled system is presented in Figure 3.1.

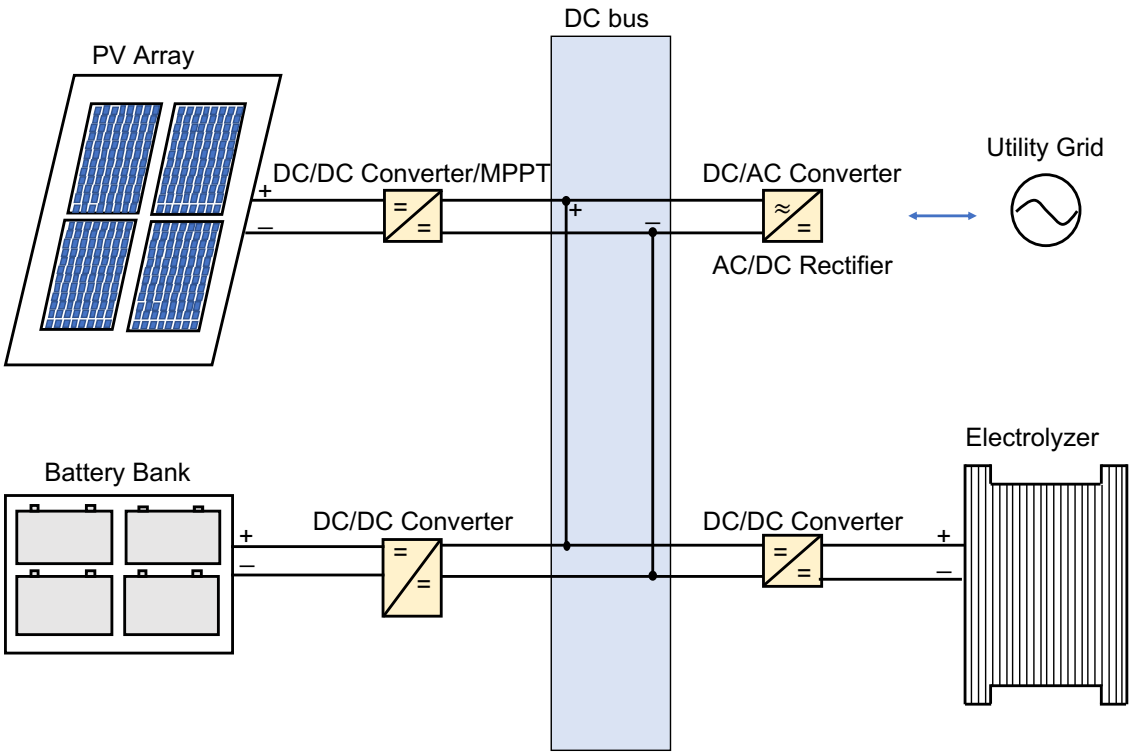

Figure 3.1: A schematic diagram of the coupled system.

To achieve maximum design and operation sustainability, we aim that the coupled system meets a *net-zero* energy throughout the whole year. Since the proposed system is designed for commercial scale applications (with hydrogen production rate in the range 5-120 Normal m^3/h), reaching a value of exactly zero is highly improbable. Instead, the coupled system can be assumed to meet a *net-zero* energy when the system meets a cut-off value of $\pm 5\%$ relative to the daily plant power consumption.

3.1.1 Literature Review

Research efforts are still underway to optimize the design and operation of sustainable hydrogen production systems. Gibson and Kelly [46] investigated a coupled PV-electrolysis system, in which they examined different system designs to reach optimal solar to hydrogen (STH) efficiency. They tested multiple commercial PV modules and concluded that directly coupling the two systems leads to optimal efficiency in cases where the PV modules are specifically designed to have a maximum power voltage (V_{mp}) that matches the electrolyzer operating voltage. In other cases where there is a mismatch between the PV modules output voltage and the electrolyzer operating voltage, incorporating a DC-DC converter in the circuit is beneficial to reach acceptable STH efficiencies.

A hybrid system consisting of PV modules and wind turbines (WT) to power an electrolyzer is simulated in Khalilnejad et al [47]. Achieving an optimal design of WT and PV systems to maximize hydrogen production, while minimizing excess energy generated was the primary focus. The simulation was intended to support the operation of an off-grid electrolyzer load for a diurnal period (24 h simulation time) in Miami city.

Aside from the promising usage of hydrogen in fuel cells for transportation applications, hydrogen can serve as a solar energy storage medium in stand-alone systems, providing backup power in cases of diurnal weather and long-term seasonal variations [43]. Lagorse et al [48] proposed a stand-alone street lighting hybrid system consisting of PV cells, storage battery, and hydrogen powered fuel cells. The

integration of fuel cells is essential in cases where the battery is unable to provide necessary power due to long-term seasonal variations. For Geneva, Switzerland, the optimal system sizing chosen to minimize the system cost, was able to power the street light all year round.

Hassan et al [49] also investigated a similar hybrid energy system for grid connected residential applications. The system consists of PV modules as the primary source of energy, coupled with a storage battery bank and a hydrogen storage system (electrolyzer, fuel cell, and hydrogen storage tanks) to cover dynamic load scenarios. They proposed different operation modes of the system based on the charging/discharging states of the battery and hydrogen storage systems. The hybrid system was able to meet the dynamic load demands with excellent grid stability. The results, however, were only simulated over 24 h period in a typical summer day in Islamabad.

Integrating renewable power resources, especially wind and PV systems, with battery storage systems has also been established to meet a certain demand load. Hongxing et al [50] presented an optimal design model for a hybrid PV-WT-Battery system to power a telecommunication relay station on a remote island in China. The model objective was to minimize the annualized cost of the system, while maximizing the system reliability using the weather data of year 1989 in Hong Kong city.

3.1.2 Motivation and Goals

An integrated PV-electrolysis-battery system is presented with the goals of identifying optimal system design. The PV modules provide the necessary power to run the electrolyzer, while charging the battery during daytime. The battery will subsequently provide power necessary to ensure uninterrupted operation of the electrolyzer during night. Diurnal and seasonal weather variations are also included, and are used to optimize individual system elements. The system is connected to the electric grid to allow continuous operation. The simulation is implemented in Python environment, and is run for the calendar year 2017 in College Park city, Maryland.

The analysis goal is to identify the optimal system configuration necessary to maximize the hydrogen production rate, minimize total annual cost of the system (ACS), minimize the levelized cost of energy (LCE), while meeting an annual grid net-energy within $\pm 5\%$ relative to the daily plant power consumption.

3.2 PV Module Modeling

3.2.1 Solar Irradiance Modeling

The solar constant E_{sc} ($= 1366$ W/m^2) is the maximum direct solar irradiation reaching the Earth's surface if none of the radiation is absorbed or scattered by the atmosphere. The effect of Earth's atmosphere is a key factor to consider since a significant fraction of the solar irradiance is either absorbed or scattered by molecules

and particles in the atmosphere, leading to the definition of two important irradiance components; direct (E_D) and diffuse (E_F). Direct irradiance refers to the direct sun beams reaching Earth, while the diffuse component corresponds to the fraction of the solar irradiance scattered by the atmosphere, but eventually reaching the Earth's surface. The global irradiance E_G is then defined as the summation of the direct and diffuse components.

The air mass (AM) corresponding to the effective amount of our atmosphere through which sunlight must pass before reaching the PV modules is approximated by [51]

$$AM = \frac{0.89^z}{\cos\zeta} \qquad \text{for } z < 3 \text{ km}$$

where z is the site elevation in km, and ζ is the zenith angle, the angle made between a line segment extending between the Earth and sun and local vertical (with $\zeta = 0$ when the sun is directly overhead).

The direct irradiance reaching a surface that is aligned perpendicular to Sun's rays can be approximated by [51]

$$E_{D^\perp} = E_{sc} \times 0.73^{AM^{0.678}} \tag{3.1}$$

From measured data, it is reasonable to assume that the diffuse component constitutes approximately 10% of the global normal irradiance, and hence the global normal irradiance can be calculated from

$$E_{G^\perp} = E_{D^\perp} + E_F = 1.11 E_{D^\perp} \tag{3.2}$$

Equation (3.2) only provides the direct global irradiance at solar noon. To include the projection effect and the time of the day, Equation (3.3) can be used [51][1].

$$E_G(t_d, \phi, \theta) = [(0.11 + \cos\,\zeta)\, E_{D^\perp}] \times H(\cos\,\zeta) \tag{3.3}$$

with

$$\cos\zeta = -\vec{n_i} \cdot \vec{s} \tag{3.4}$$

$$\vec{s} = 0\vec{x} + 1\vec{y} + 0\vec{z} \tag{3.5}$$

$$\vec{n_i} = n_{x_i}\vec{x} + n_{y_i}\vec{y} + n_{z_i}\vec{z} \tag{3.6}$$

$$n_{x_i} = \cos\lambda_y\, \sin\phi\, \sin\theta_i + \sin\lambda_y\, (\cos\delta\, \sin\phi\, \cos\theta_i + \sin\delta\, \cos\phi) \tag{3.7}$$

$$n_{y_i} = -\sin\lambda_y\, \sin\phi\, \sin\theta_i + \cos\lambda_y\, (\cos\delta\, \sin\phi\, \cos\theta_i + \sin\delta\, \cos\phi) \tag{3.8}$$

$$n_{z_i} = -\sin\delta\, \sin\phi\, \cos\theta_i + \cos\delta\, \cos\phi \tag{3.9}$$

$$ast_i = 24\,(i/n_{ast}) \tag{3.10}$$

$$\theta_i = 2\pi\,(n_{ast} - i)\,/n_{ast} - 2\pi\,(t_d/365) \tag{3.11}$$

$$\phi = 2\pi\,(90^o - \phi^o\mathrm{N})\,/360^o \tag{3.12}$$

where $\vec{n_i}$ is the vector normal to and pointing out of the PV module surface, $\vec{s}$ is the solar radiation vector directed along y-axis, $\lambda_y = 2\pi t_d/365$ is an angle representing Earth's mean orbit at t_d, t_d is the number of days past the most recent winter solstice, ϕ is the latitude in degrees measured north of the equator, θ is the longitude, δ is the Earth's declination at $t_d = 0$ (equals to 23.44^o), ast is the apparent solar time

[1]The global irradiance model is implemented in Python environment by Prof. Raymond Adomaitis, as a toolbox for the research group.

(with $ast = 12$ at solar noon, and $ast = 0, 24$ at midnight), and H is the Heaviside function and is used to prevent negative irradiance values on the night-side of the planet. Detailed derivation of these equations is provided in [51].

When a PV module is tilted with an angle θ_{tilt} towards the South Pole, $\phi_{tilt} = \phi + \theta_{tilt}$ is used in Equations (3.7), (3.8), (3.9), and (3.12) instead of ϕ to calculate $\vec{n}_{i,tilt}$ and $\cos\zeta_{tilt}$. The global irradiance can then be calculated from:

$$E_G(t_d, \phi, \theta) = [H(\cos\,\zeta_{tilt})E_{D^\perp}\cos\,\zeta_{tilt} + 0.11E_{D^\perp}] \times H(\cos\,\zeta) \tag{3.13}$$

The $H(\cos\,\zeta_{tilt})$ term is added to account for cases where the PV module is tilted away from the Sun's radiation during daylight (with $\cos\,\zeta_{tilt} < 0$ and $\cos\,\zeta > 0$), and hence only receives the diffuse component of the irradiance.

3.2.1.1 Effect of Cloud Cover

The above model calculates the global irradiance falling on a PV module surface given its orientation, at any location as a function of time of the day. However, the effect of cloud cover is not yet addressed. For a completely cloudy day, it is reasonable to assume that only the diffuse part of the irradiance constitutes the global solar irradiance, with 20% the intensity of the direct normal irradiance [52]

$$E_{\text{cloudy}} = 0.2 \times E_D^\perp \tag{3.14}$$

Since the clouds cover is typically represented as a fraction between 0 and 1, a simple weighted average is assumed such that the irradiance value is equal to E_G for sunny days ($CloudsCover = 0$), and E_{cloudy} for a completely cloudy day ($CloudsCover = 1$).

$$E_{\text{total}} = CloudsCover \times E_{\text{cloudy}} + (1 - CloudsCover) \times E_{\text{G}} \tag{3.15}$$

An hourly weather forecast for the 2017 year is acquired by executing an API request from the Dark Sky API website [53]. Hourly cloud cover data then can be extracted from the weather forecast data. Figures 3.2 and 3.3 provide the cloud cover data for College Park, MD for the entire year, and for the first week of the year, respectively, compared to the total solar irradiance calculated E_{total}, showing the inverse correlation between the two.

3.2.2 PV Module Characteristics

Let us consider an array of M parallel rows of PV cells, each row containing N cells connected in series; this constitutes a basic PV module. If each cell in the module performs identically, the module performance model can be written in terms of the diode equation

$$I = M \left\{ -I_{ph} X(t) + I_o \left[\exp\left(q \frac{V/N - (I/M)R_s}{\beta k_B T} \right) - 1 \right] + \frac{V/N - (I/M)R_s}{R_{sh}} \right\} \tag{3.16}$$

where $X(t)$ is the dimensionless concentrating factor proportional to the global irradiance so that $X(t) = E_{\text{total}}(t)/(1000\ \text{W/m}^2)$. The diode ideality factor $\beta \in [1, 2]$ approaches unity under ideal performance conditions. The series R_s and shunt R_{sh}

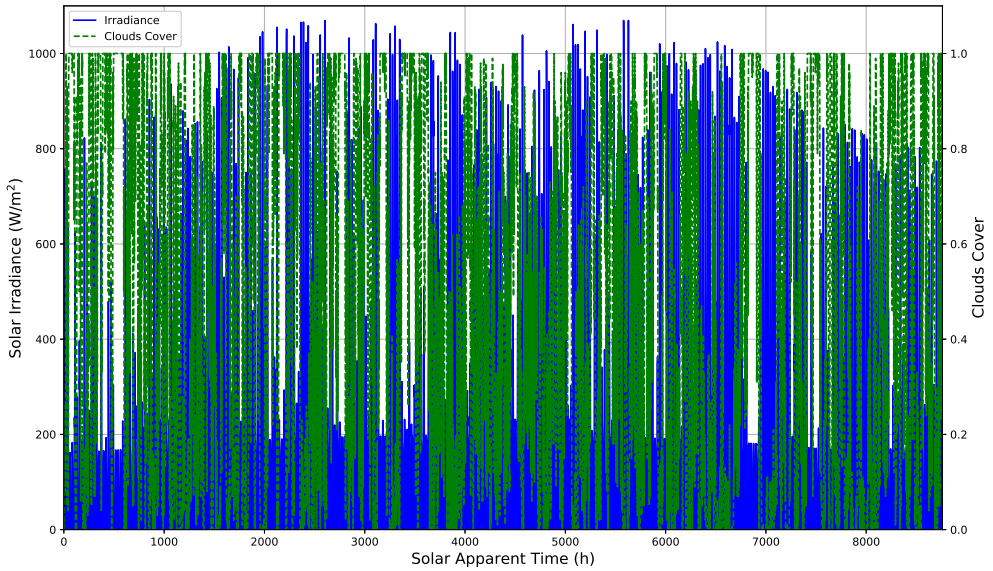

Figure 3.2: Hourly cloud cover data from Dark Sky API for College Park, MD for 2017 and the solar irradiance E_{total} calculated at a module tilt angle of 35°.

resistances approach 0 and positive infinity, respectively, for an ideal PV cell. I_o and I_{ph} are the dark saturation and photo-currents, respectively.

The PV module considered in this work is the SunPower SPR-X21-345 [54], with its specifications given in Table 3.1 with $M = 1$ and $N = 96$, noting that these characteristics apply to the *entire* module, not the individual cells.

Examining (3.16) we see that we have five unknown parameters: β, I_o, I_{ph}, R_s, and R_{sh} and four data points (V_{oc}, I_{sc}, V_{mp}, and I_{mp}) that, in combination with (3.16), effectively produce four independent equations. The first equation is the diode equation (3.16) evaluated at P_{mp}:

$$I_{mp} = M\left\{-I_{ph} + I_o\left[\exp\left(q\frac{V_{mp}/N - (I_{mp}/M)R_s}{\beta k_B T}\right) - 1\right] + \frac{V_{mp}/N - (I_{mp}/M)R_s}{R_{sh}}\right\}$$

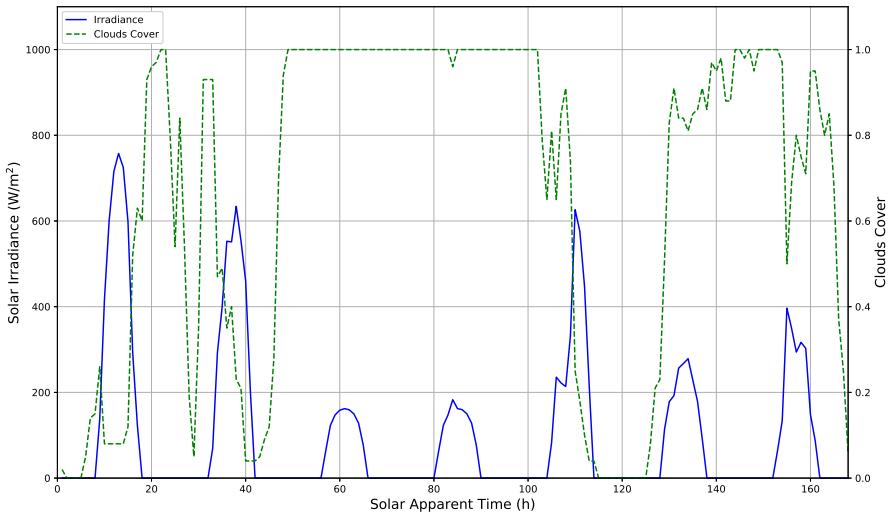

Figure 3.3: Hourly cloud cover data from Dark Sky API for College Park, MD for the first week of 2017 and the solar irradiance E_{total} calculated at a module tilt angle of 35°.

the second is the P_{mp} condition itself:

$$0 = \frac{d}{dV_{mp}} V_{mp} M \left\{ -I_{ph} + I_o \left[\exp\left(q \frac{V_{mp}/N - (I_{mp}/M)R_s}{\beta k_B T} \right) - 1 \right] + \frac{V_{mp}/N - (I_{mp}/M)R_s}{R_{sh}} \right\}$$

the third corresponds to the short-circuit condition:

$$I_{sc} = M \left\{ -I_{ph} + I_o \left[\exp\left(-q \frac{I_{sc} R_s}{M \beta k_B T} \right) - 1 \right] - \frac{I_{sc} R_s}{M R_{sh}} \right\}$$

and the forth the open-circuit condition:

$$0 = M \left\{ -I_{ph} + I_o \left[\exp\left(q \frac{V_{oc}}{N \beta k_B T} \right) - 1 \right] + \frac{V_{oc}}{N R_{sh}} \right\}$$

Table 3.1: SunPower SPR-X21-345 module specifications [54] under AM1.5 conditions normalized to 1000 W m^{-2} irradiance and 25 ^{o}C. At the maximum power point $P_{mp} = V_{mp}I_{mp}$. Open-circuit voltage is V_{oc} and short-circuit current is I_{sc}.

N	A (m^2)	V_{oc} (V)	I_{sc} (A)	V_{mp} (V)	I_{mp} (A)	P_{mp} (W)
96	1.63	68.2	6.39	57.3	6.02	345

As such, the system is underdetermined; to identify the additional conditions required to determine a set of model operating parameters, we define the *regularization* equations

$$\beta = 1, \quad R_s = 0, \quad \frac{1}{R_{sh}} = 0$$

based on the ideal conditions of each parameter. This now gives us seven equations and five unknowns. Therefore, we use an iterative non-linear procedure to find the parameter values *on a per-cell basis*; results are shown in Figure 3.4 and presented in Table 3.2. These parameters are then substituted in the diode equation (3.16) to determine the $I - V$ and $P - V$ characteristic curves at each point during the day according to the different value of the concentration factor $X(t)$.

Table 3.2: SunPower SPR-X21-345 module parameter fitting results on a per-cell basis.

I_{ph} (A)	I_o (A)	R_s (Ω)	R_{sh} (Ω)	β
6.39	6.28×10^{-12}	6.70×10^{-3}	2.00×10^{3}	1

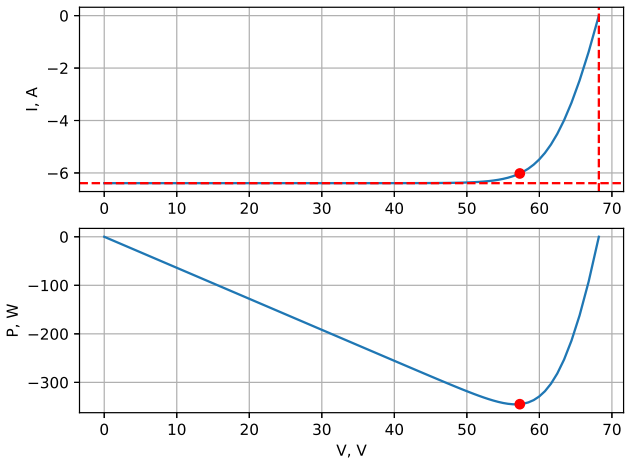

Figure 3.4: SunPower SPR-X21-345 Module parameter fitting results (the negative sign corresponds to power produced by the PV module). The maximum power point is denoted in red, and V_{oc}, I_{sc}, V_{mp}, P_{mp}, and I_{mp} are listed in Table 3.1

.

As described earlier, PV systems are ideal power supplies for electrolyzers. This is mainly because the output voltage of the PV modules can be controlled to relatively constant values as illumination levels change. This is particularly valuable for fast transients, such as the sudden reduction of irradiance due to a passing cloud. Furthermore, the use of a DC-DC converter and optimizer ensures that the output power is at the maximum power point (P_{mp}, V_{mp}, I_{mp}). In this analysis, we assume the electrolyzer follows a constant-current operational mode, which requires a constant and steady source of voltage. Hence, the mean value of the non-zero V_{mp} entries throughout the year is chosen as the operational voltage of the electrolyzer. Figure 3.5 shows V_{mp} for the year, with the mean value $V_{mp,mean}$ calculated to be 55.6 V.

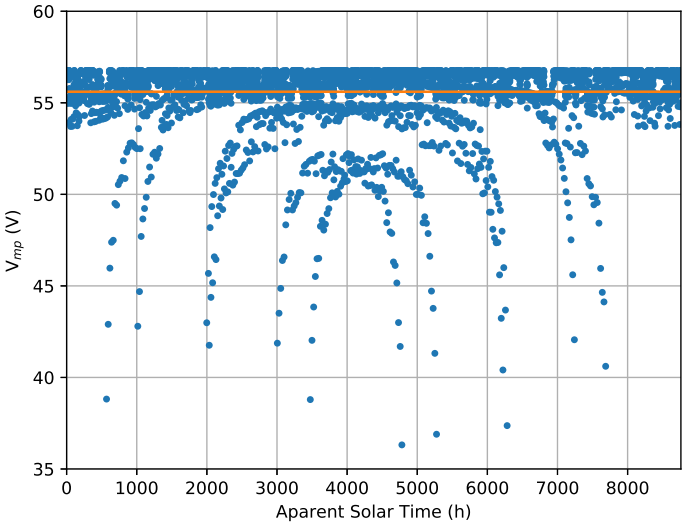

Figure 3.5: Non-zero values of the V_{mp} (i.e., during daylight operation of the PV module), with the mean value calculated.

3.2.3 Optimal Module Tilt

To optimize PV module performance, we investigate the influence of module tilt angle on the output power of the PV module. A set of tilt values between 0-90° is used in the PV model, and the summation of P_{mp} produced throughout the year is calculated for each module tilt value. Figure 3.6 shows the values of P_{mp} harvested during the 2017 year, with an optimal module tilt of 35°. This value is chosen for the remainder of the analysis in this chapter.

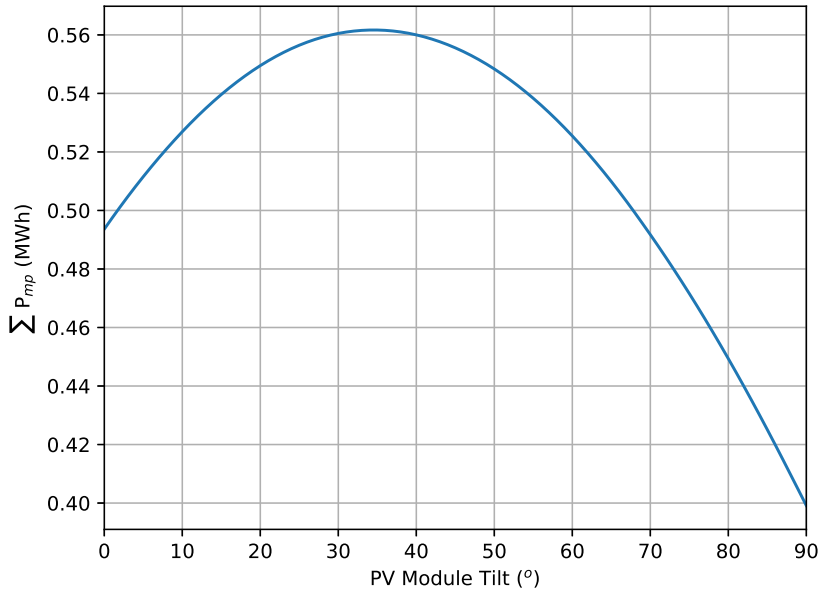

Figure 3.6: The effect of module tilt on P_{mp} value harvested during 2017 showing an optimal tilt of 35°.

3.3 Electrolyzer Design

Since the early discovery of water electrolysis in 1800 [55], different types of electrolyzers have been developed. Some are still in the research and development (R&D) phase while others are more mature and commercially available. The main three types are: alkaline electrolyzers, proton exchange membrane (PEM) electrolyzers, and solid oxide electrolyzers (SOE). Currently, two low temperature electrolyzers dominate the market: alkaline and PEM electrolyzers [44].

Alkaline electrolysis is the most mature technology among the three. It was first established in 1800 when Nicholson and Carlisle discovered the electrolytical splitting of water [55]. Alkaline electrolysis technology consists of two electrodes

(anode and cathode) immersed in an aqueous electrolyte, separated by a thin microporous diaphragm divider. The diaphragm allows the transport of the hydroxide ion from the cathode to the anode, while serving as a physical barrier to separate the product hydrogen and oxygen gases, preventing the formation of an explosive mixture [44].

Conventional alkaline electrolyzers typically operate at pressures of 1-30 bar and temperatures between 70 to 100° C [56]. Most commercial alkaline electrolyzers operate at 80° C [43], [55], [56]. Water is nominally split at current densities between 100 to 400 mA/cm^2 in an aqueous KOH electrolyte with concentrations between 25-35 wt% [44]. Higher current densities are avoided as they will increase internal ohmic losses due to the electrolyte [6], [44].

PEM electrolyzers feature a zero-gap membrane architecture in which a solid polymer electrolyte, such as Nafion, is sandwiched between two porous electrode layers [44]. Similar to the function of the diaphragm in alkaline electrolyzers, the solid polymer electrolyte allows the transfer of protons, while physically separating the evolved gases. PEM electrolyzers typically operate at higher temperatures up to 120° C, and pressure values in the range 20-50 bar [43] [57]. They have an advantage over the alkaline electrolyzers in that the design is more compact, and that deionized water is used instead of the hazardous KOH electrolyte [46].

PEM electrolyzers can reach higher current densities, between 600 to 2000 mA/cm^2 [44]. This is mainly due to the cell design, forcing the gas bubbles to be formed on the outer sides of the cell, minimizing ohmic losses in the electrolyte due to bubble formation at high currents. In addition, the compactness of the cell

design helps in shortening the distance traveled by ions in the electrolyte, which also minimizes ohmic losses (the distance traveled in PEM polymer is on the order of 100-200 μm as opposed to several millimeters in alkaline electrolyzers) [44]. However, PEM electrolyzers are known to be associated with higher investment, operating, and maintenance costs, with a factor of 1.5 to 2 times the state-of-art commercial alkaline electrolyzers [57], [58].

SOE use steam instead of liquid water as the process input, and typically operate at higher temperatures in the range 700-900° C, and pressures between 1-15 bar [57]. They are the most promising technology due to their high efficiency, potentially reaching up to 100%, but they are still in the R&D stage [57].

When discussing SOE, one has to mention the advantages of water electrolysis at elevated temperatures. As temperature is increased, the equilibrium voltage required to split water decreases from a value of 1.23 V at 300 K to 0 V at temperatures higher than 2000 K, where the water dissociation reaction becomes spontaneous without any applied voltage [43]. The elevated temperature of PEM electrolyzers (120° C) relative to alkaline electrolyzers (80° C) is insufficient to produce a noticiable decrease in the required equilibrium water splitting potential, and the efficiencies of both are 65-70% [43], [57]. However, with high temperature steam electrolysis at 800-900° C, the efficiency can reach values greater than 90% [43].

The alkaline water electrolyzers are sufficiently developed and qualified to carry out hydrogen production from renewable energy sources at high production rates. However, to completely satisfy the requirement of the increasing hydrogen economy, higher electrolyzer capacities are required [4]. PEM electrolyzers are commercially

available, yet their cost is high and they are limited to lower capacity applications compared to alkaline electrolysis units [4], [57]. As a result of this comparative analysis, we will consider an alkaline water electrolysis unit in this work.

3.3.1 Alkaline Electrolysis

In practice, two major designs are available for alkaline electrolysis: monopolar and bipolar configurations. A schematic diagram of each type is shown in Figure 3.7.

A monopolar alkaline water electrolyzer design consists of a number of individual electrolysis cells (M) electrically connected in parallel. Each cell consists of an anode and cathode, separated by a porous membrane required to ensure the separation of hydrogen and oxygen gases produced while allowing the transport of hydroxide ions through the electrolyte.

Due to the parallel wiring configuration of cells in a monopolar stack, it generally operates at low voltage and high current. Therefore, in large-scale applications, multiple stacks (N) are connected in series to ensure the total applied voltage is reasonably distributed over each stack, which eventually reduces ohmic losses caused by reaching high limiting current values [6].

In bipolar designs, the active electrodes (positive and negative) are connected to different sides of a conducting metal plate (or a bipole), and they are geometrically and electrically connected in series [6], [56]. A bipolar stack consisting of N cells wired in series typically operate at higher voltage and lower currents, hence, multiple

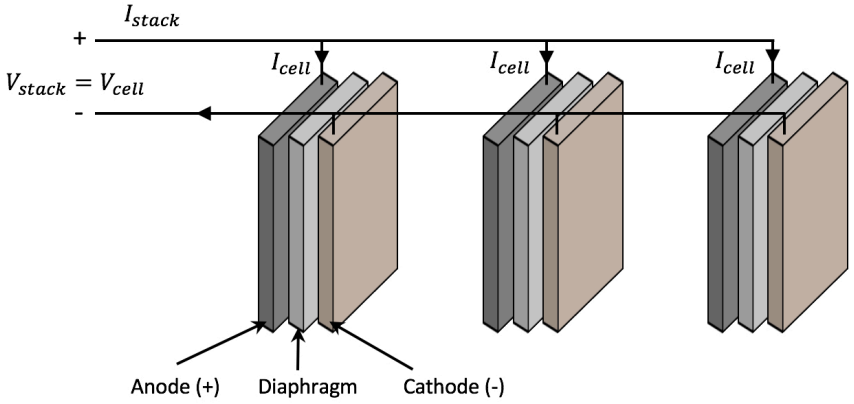

(a)

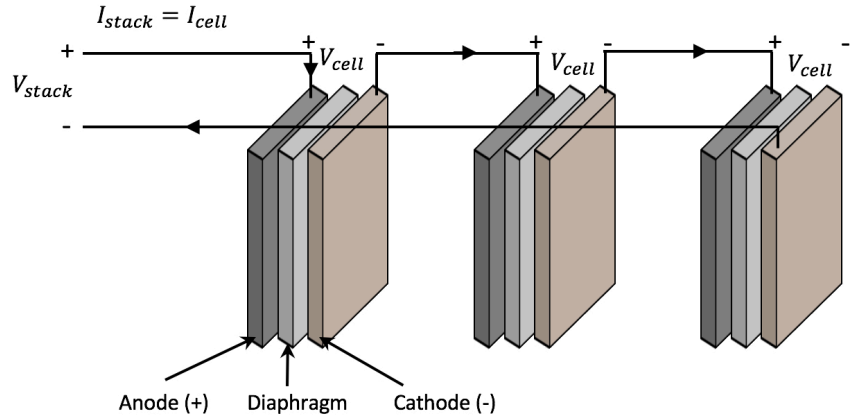

(b)

Figure 3.7: A schematic of a monopolar (a) and a bipolar (b) alkaline electrolyzer design. Adapted from [58].

stacks M connected in parallel are required for large-scale applications.

The bipolar design has an advantage in that it is more compact and offers shorter current paths than the monopolar design. However, becasue of this system's compactness and higher operating pressure, a more sophisticated design is necessary, leading to higher manufacturing costs [56]. Nevertheless, most commercial alkaline electrolyzers follow the bipolar configuration, hence, a bipolar electrolyzer design is considered in this work.

The diaphragm choice has critical implications for the electrolyzer design and operation. The diaphragm must have high ionic conductivity, while being stable in strong alkaline solutions and high temperatures. For this work, we choose Zirfon Perl [59], a high quality separator membrane for alkaline water electrolysis. This membrane is durable in strong alkaline solutions (up to 6 M KOH), and up to 110° C. It has high number of OH^- groups at alkaline pH and low ionic resistance, allowing higher current values to be reached. Some of the important technical specifications of this membrane are listed in Table 3.3.

State-of-art commercial alkaline electrolyzers have a cell area of less than 3.6 m^2, and an electrolyte gap (the distance traveled by ions in the electrolyte) of several millimeters [44], [57]. Hence, our design assumes a cell area of 0.5 m^2, an electrolyte gap of 5 mm, an operating temperature of 80° C, and a 25 wt% KOH electrolyte.

Table 3.3: Physical and operational specifications of the Zirfon Perl membrane [59].

Specification	Value
Ionic resistance (at 30° C in 30 wt% KOH)	0.3 Ωcm^2
Max temperature	110° C
Max electrolyte strength	30 wt%
Thickness	500 $\pm$ 50 μm

3.3.2 Electrolysis Cell Characteristics

In Chapter 2, we investigated the mechanism and kinetics of both OER and HER on NiFe LDH films deposited on Ni foam substrates. We combined the results and analysis of linear sweep voltammetry (LSV) and electrochemical impedance spectroscopy (EIS) to reveal valuable insight on the reaction kinetics and mechanism occurring at each electrode. The results identified from the anode and the cathode were then combined to fit the electrochemical cell experimental data.

Now that the electrolyzer design is set, we can investigate the electrolysis cell characteristics at the nominal set of design parameters. It is well known that most reaction rate constants of solution reactions vary with temperature according to Arrhenius law:

$$\ln k \propto -\frac{1}{T} \tag{3.17}$$

The electrolyzer is assumed to operate at 80° C, and Equation (3.17) can be used to recalculate the values of the partial standard reaction rate constants in Tables 2.3 and 2.7, that were originally evaluated at room temperature. Tables 3.4 and 3.5 list the calculated rate constants for the HER and OER at 80° C.

Table 3.4: Chemical rate constants k_i (mol cm^{-2} s^{-1}) and partial standard chemical rate constants k_i^o (cm s^{-1}) for HER at 80° C.

k_V	k_{-V}	k_H	k_{-H}	k_T	k_{-T}
1.27e-05	4.40e-09	7.63e-09	1.29e-4	5.89e-06	1.00
k_V^o	k_{-V}^o	k_H^o	k_{-H}^o	k_T^o	k_{-T}^o
1.42e-4	1.41e-06	8.54e-08	4.14e-2	5.89e-06	1.00

Table 3.5: Chemical rate constants k_i (mol cm^{-2} s^{-1}) and partial standard chemical rate constants k_i^o (cm s^{-1}) for OER at 80° C.

k_1	k_{-1}	k_2	k_{-2}	k_3	k_{-3}	k_4	k_{-4}	k_5	k_{-5}
2.75e-4	1.61e-8	6.80e-2	1.0e-10	1.08e-9	9.59e-1	1.16e-4	1.29e-3	2.89e-4	9.83e-1
k_1^o	k_{-1}^o	k_2^o	k_{-2}^o	k_3^o	k_{-3}^o	k_4^o	k_{-4}^o	k_5^o	k_{-5}^o
3.40e-1	3.08e-7	33.98	4.93e-8	1.03e-5	9.66e-1	1.65	4.31e-2	1.10e-3	9.86e-1

In addition to its effect on the reaction kinetics, temperature has a crucial influence on the electrolyte resistivity: higher temperatures promote higher ionic conductivity in the electrolyte. A 25 wt% KOH electrolyte at 80° C has an ionic conductivity of 1.302 S/cm [60]. With a 5 mm electrolyte path and 0.5 m^2 electrode area, we can calculate the electrolyte total ohmic resistance as:

$$\begin{aligned} R_{solution} &= \frac{1}{\text{Conductivity}} \times \frac{\text{Electrolyte Path}}{\text{Electrode Area}} \\ &= \frac{1}{1.302 \text{ S/cm}} \times \frac{0.5 \text{ cm}}{5000 \text{ cm}^2} \\ &= 7.68 \times 10^{-5} \ \Omega \\ R_{membrane} &= \frac{R_{ionic}}{A_{membrane}} = \frac{0.3 \ \Omega\text{cm}^2}{5000 \text{ cm}^2} \\ &= 6 \times 10^{-5} \ \Omega \\ R_{\Omega} &= R_{solution} + R_{membrane} \\ &= 1.368 \times 10^{-4} \ \Omega \end{aligned}$$

The molarity of a 25 wt% KOH electrolyte can be calculated from [60]:

$$M = \frac{(\text{wt\% KOH}) \times \rho}{100 \times \text{M}_{\text{wt}}} \tag{3.18}$$

$$\rho = \text{A} \ \exp\left(0.0086 \times \text{wt\%}\right) \tag{3.19}$$

At 80° C, the parameter A in Equation (3.19) is equal to 971.89 kg/m^3 [60], resulting in a molarity of 5.37 M, and an OH^- ion concentration of 5.37×10^{-3} mol/cm^3.

To obtain the current-voltage characteristics of a single electrolysis cell in a stack, Equation 2.37 is mainly used for this purpose, along with Equations 2.4 and

2.7 to express the HER kinetics, and Equations 2.16 and 2.22-2.36 to express the OER kinetics. Because of the implicit and complicated nature of these equations, the determination of the IV characteristics was not straight forward. Instead, a Newton based method must be implemented for the individual evaluation of the OER, HER, and electrolysis cell characteristics.

Starting with a vector of I values from 0 to 600 mA/cm^2, we first determine the OER and HER overpotential values (numerically using Newton's method) associated with each value of the current. Given the value of the total ohmic resistance, we then apply Equation 2.37 to calculate the total cell voltage and obtain the cell IV characteristics. The resulted IV curve is shown in Figure 3.8.

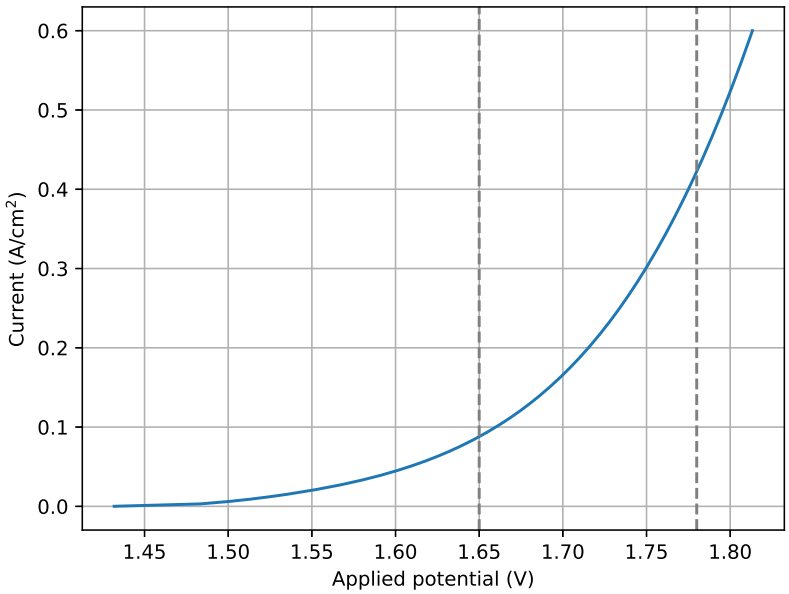

Figure 3.8: Current-voltage characteristics of the electrolysis cell at 80 C. The dash lines define the electrolysis cell operating range, approximately between 100-400 mA/cm^2.

Figure 3.8 is crucial in the design and operation of the electrolyzer unit. It will be used to calculate the current of a single cell in the stack, at a given voltage determined by the PV module performance. To lower system losses associated with the cell ohmic resistance, conventional alkaline electrolyzers typically operate at current densities between 100-400 mA/cm^2 [6], [44]. This operating range defines upper and lower bounds on the numbers of cells N connected in series in an electrolyzer stack. At this operating range of current densities, the design voltage for each cell should be kept between 1.65-1.78 V, as seen in Fig. 3.8. Hence, for the coupled system design optimization purposes, a feasible set of N values is defined as:

$$\frac{V_{mp,mean}}{1.78} \leq N \leq \frac{V_{\text{mp,mean}}}{1.65} \tag{3.20}$$

This results in a feasible set of N values of [32, 33, 34] cells connected in series.

3.3.3 Power of the Electrolyzer

Since the output voltage of the PV modules is DC and is nearly constant with illumination level [43], the electrolyzer is assumed to follow a fixed current operational mode. For a fixed N cells wired in series, and M stacks connected in parallel, the total power of the electrolyzer at any time is equal to:

$$P_e = M \times N \times V_{\text{cell}} \times I_{\text{cell}} \tag{3.21}$$

The total hydrogen production rate (mol/s) can be calculated from:

$$n_{\text{H}_2} = \frac{M \times N \times I_{\text{cell}}}{2 \times F} \tag{3.22}$$

Gas flow rates are typically reported as normal cubic meters per hour (Nm^3/h). The volumetric production rate can be calculated using [56]:

$$V_{H_2} = n_{H_2} \times \nu_{std} \times 3600 \tag{3.23}$$

where ν_{std} is the volume of an ideal gas at standard conditions. Another important metric in the electrolyzer design is the specific energy consumption (SEC). SEC refers to the amount of energy needed in kWh to produce 1 Nm^3 of hydrogen, and can be calculated as

$$SEC = \frac{P_e}{V_{H_2}} \tag{3.24}$$

The state-of-art commercial alkaline electrolyzers typically have a SEC value of 4.2-4.8 kWh/Nm^3 [57].

3.4 Battery Design

Lead acid rechargeable batteries are the most common energy storage devices associated with PV system applications [48]. With a high efficiency of at least 80% [48], low self-discharge, low cost, high availability (due to large well-established market worldwide), lead acid batteries are strong competitive in the rechargeable batteries market, even against the fast developing Li-ion batteries. Despite the high weight of the lead acid batteries, they remain an excellent candidate for stationary renewable system applications where the weight has negligible influence on the performance. Li-ion batteries with higher cycle life and lighter in weight are more associated with applications where the battery weight is a significant factor in the

design and operation, such as laptops, automotive, and mobile phones. However, they are more expensive than lead acid batteries.

Sustainability is another advantage of lead acid batteries. Recycling of lead acid batteries has been established with recycling rates up to 100% [61]. The lead in these batteries is easily separated from the plastic and acid, and all of these components can be recovered and re-used with low recycling energy input [61]. This is not the case for Li-ion batteries where the recycling rates are much lower [61].

A battery model is proposed in (3.25), which is simple yet capable of accurately predicting the stored battery energy at any point in time. The electrolyzer unit is assumed to be operating at constant current mode, therefore, for a fixed system design, the battery state of charge (SOC) is solely dependent on the solar irradiance and weather conditions. The battery SOC is a measurement that is commonly reported when discussing the battery state change with time, and takes values between 0% (empty) and 100% (fully charged). The battery, therefore, will only charge when the PV modules are producing excess power, and are required to discharge when the PV power is insufficient to operate the electrolyzer system.

Considering a lead acid battery with an energy efficiency η_b of 85% [61], the battery operation can be expressed from energy standpoint:

$$\frac{dE_b}{dt} = \begin{cases} \eta_b \left(P_{PV}(t) - P_e(t)\right), & P_{PV}(t) \geq P_e(t) \\ \left(P_{PV}(t) - P_e(t)\right), & P_{PV}(t) < P_e(t) \end{cases} \tag{3.25}$$

with

$$SOC(t) = \frac{E_b(t)}{Cap} \times 100 \tag{3.26}$$

where E_b is the energy stored in the battery, Cap is the battery capacity, and P_{PV} and P_e are the PV power produced, and electrolyzer power consumed, respectively. The first case in (3.25) corresponds to a charging state, and the second case is a discharging state. To extend the life of a lead acid battery, it should not be completely depleted. Instead, a minimum limit on the battery energy should be applied. The battery depth of discharge (DoD) is defined as the percentage of the discharged energy of the battery to the total battery capacity. In this model, a DoD of 70% is applied as the minimum limit constraint on the battery [62].

For each design configuration investigated, a constraint on the battery capacity is applied, in which the capacity should be able to provide continuous operation of the electrolyzer for at least 12 continuous hours when fully charged. This is to ensure the feasibility of the solution based on our analysis goal. Minimizing the system cost might force the algorithm to choose a design where the battery capacity is too small compared to the plant hydrogen production capacity. These cases correspond to situations where the battery is only able to provide continuous operation for few hours, i.e., only one or two hours of operation. This case will require purchasing enormous amounts of energy from the grid, which can off-set limited battery capacity on days with high irradiance. To illustrate, the small battery size compared to the power generated by the PV modules will allow it to fully charge rapidly, and the excess energy will be sold back to the grid, resulting in a net-zero grid energy. However, we aim to avoid these scenarios since they contrast the objective of this work, which is to only rely on the grid power in rare cases where the weather variations have substantial influence the output power of the PV modules.

3.5 Integrated System

3.5.1 Economic Model

3.5.1.1 System Cost

Our economic model is derived from the annualized cost of the system (ACS), which mainly consists of the annualized costs of PV ($C_{\mathrm{a,pv}}$), electrolyzer ($C_{\mathrm{a,e}}$), and battery ($C_{\mathrm{a,bat}}$). The cost of grid electricity ($C_{\mathrm{a,grid}}$) also is included in the analysis. The ACS can be calculated using:

$$ACS = C_{\mathrm{a,pv}} + C_{\mathrm{a,e}} + C_{\mathrm{a,bat}} + C_{\mathrm{a,grid}} \tag{3.27}$$

For each component in the coupled system, the annualized cost is the summation of the capital cost (C_{aCapital}), replacement cost (C_{aRep}), and the operation and maintenance cost ($C_{\mathrm{aO\&M}}$). Hence, the total annualized cost of the j^{th} component can be written as:

$$C_{\mathrm{a},j} = C_{\mathrm{aCapital},j} + C_{\mathrm{aO\&M},j} + C_{\mathrm{aRep},j} \tag{3.28}$$

The annualized capital cost for the PV modules and electrolyzer can be calculated using [50]

$$C_{\mathrm{Capital},j} = U_j \times P_j \tag{3.29}$$

$$CRF_j = \frac{i(1+i)^{n_j}}{(1+i)^{n_j} - 1} \tag{3.30}$$

$$C_{\mathrm{aCapital},j} = C_{\mathrm{Capital},j} \times CRF_j \tag{3.31}$$

where the subscript j is used to denote the component (PV, electrolyzer). $C_{\mathrm{Capital},j}$

is the capital investment and installed cost ($), U_j is the unit capital cost ($/kW), P_j is the power produced or consumed (kW), CRE_j is the capital recovery factor (necessary to calculate the annual worth from the present value), i is the real discount rate, and n_j is the lifetime of the j^{th} component. P_{pv} is the nominal power produced by each module (=0.345 kW [54]) multiplied by the number of PV modules (M_{pv}).

For the battery capital cost, the P_j is Equation 3.32 is replaced with the battery capacity (Cap), and the unit capital cost U_{bat} is given in $/kWh:

$$C_{\text{Capital,bat}} = U_{\text{bat}} \times Cap \tag{3.32}$$

$$CRF_{\text{bat}} = \frac{i(1+i)^{n_{\text{bat}}}}{(1+i)^{n_{\text{bat}}} - 1} \tag{3.33}$$

$$C_{\text{aCapital,bat}} = C_{\text{Capital,bat}} \times CRF_{\text{bat}} \tag{3.34}$$

The annualized O&M costs for the PV modules and electrolyzer can be determined from:

$$C_{\text{aO\&M},j} = U_{\text{O\&M},j} \times P_j \tag{3.35}$$

The battery annualized O&M costs is:

$$C_{\text{aO\&M,bat}} = U_{\text{O\&M,bat}} \times Cap \tag{3.36}$$

In this work, we assume the project lifetime equals to the PV system lifetime of 30 years [45], hence, no replacement cost is considered for the PV system. Alkaline electrolysis plants have a lifetime up to 30-50 years; however, stack replacements are often required before reaching this lifetime [57]. Most state-of-art commercial alkaline electrolyzers have a stack lifetime between 78,840 and 96,000 hr, equivalent to 9.2-11.2 years (with 8,585 operational hour per year) [63], [64]. Considering a

stack lifetime of 10 years, replacements are required twice during the lifetime of the project. With a stack replacement cost of 50% of the capital installed cost [63], the annualized replacement cost is calculated using:

$$C_{\text{Rep,e}} = RF_{\text{Rep,e}} \times C_{\text{Capital,e}} \tag{3.37}$$

$$C_{\text{aRep,e}} = CRF_e \times \left(C_{\text{Rep,e}}(1+i)^{-10} + C_{\text{Rep,e}}(1+i)^{-20}\right) \tag{3.38}$$

where RF is the replacement cost factor. Lead-acid batteries typically have a lifetime of 15 years, after which the battery bank is replaced. With a replacement factor (RF) of 100%, we can calculate the annualized replacement cost using Equation (3.40). The economic parameters used in this analysis are given in Table 3.6.

$$C_{\text{Rep,bat}} = RF_{\text{Rep,bat}} \times C_{\text{Capital,bat}} \tag{3.39}$$

$$C_{\text{aRep,bat}} = CRF_{\text{bat}} \times C_{\text{Rep,bat}}(1+i)^{-15} \tag{3.40}$$

The U.S. Energy Information Administration reported the cost of electricity for commercial applications in the state of Maryland of 0.1075 $/kWh [65]. Hence, to calculate the grid annualized cost, the cost of electricity is multiplied by the net-energy consumption for the year:

$$C_{\text{a,grid}} = 0.1075 \times \text{Net Energy} \tag{3.41}$$

$C_{\text{a,grid}}$ can either take a positive or a negative value, depending on the sign of the yearly net-energy balance for each configuration considered in the optimization study. A positive sign of the net grid energy is assigned when excess energy is sold to the grid, and negative for energy supplied by the grid.

Table 3.6: The economic parameters used in this analysis. A real discount rate i of 6.9% is assumed in this analysis for 2017 [45].

	PV	Electrolyzer	Battery
U_j	1850 ($/kW) [45]	1300 ($/kW) [57]	500 ($/kWh) [61]
$U_{\mathrm{O\&M},j}$ (/year)	21 ($/kW) [45]	2.5% $\times U_{\mathrm{e}}$ ($/kW) [57]	3% $\times U_{\mathrm{bat}}$ ($/kWh) [50], [62]
n_j (year)	30 [45]	10 [63]	15 [61]

3.5.1.2 Levelized Cost of Energy

The levelized cost of energy (LCE) is a concept frequently discussed when comparing alternative energy producing systems, particularly with renewables such as solar or wind. It also is used as a benchmark to evaluate different system configurations and to determine the optimal design. LCE can be defined as the cost associated with producing 1 kWh of energy. It can be calculated by dividing the total annualized costs of the hybrid system ($/yr) by the total energy produced by the PV system (kWh/yr) [66]:

$$LCE = \frac{C_{\mathrm{a,pv}} + C_{\mathrm{a,bat}}}{E_{\mathrm{an}}} \tag{3.42}$$

3.5.2 Problem Formulation

In this work, we seek to design and optimize the coupled system with the goals of maximizing hydrogen production rate while minimizing the total cost associated with the system design. This implicitly requires finding the right design configuration necessary to ensure high hydrogen production rate, while minimizing excess power production and system physical dimensions. To promote sustainability, the optimal design will be required to have an annual net-grid energy balance that falls within $\pm 5\%$ relative to the daily plant power consumption. In addition to minimizing the combined system cost, minimizing the LCE also is included to ensure the optimality of the design.

The optimization variables considered are the number of PV modules connected in parallel (M_{pv}), number of electrolysis cells in each stack (N), number of stacks in the electrolyzer unit (M), and battery capacity (Cap). The design variables values, given in Table 3.7, define a feasible set of 2,364,120 possible configurations to consider in the optimization problem. The chosen M_{pv} and Cap ranges are intended to cover the maximum and minimum electrolyzer power demand at the ranges of N and M presented in Table 3.7.

3.5.3 Coupled System Model Algorithm

After acquiring the cloud cover data for a specific year, we initialize the set of design configurations based on the variables given in Table 3.7. For each design configuration, the algorithm proceeds as a loop with incremental hourly time-steps

Table 3.7: Range and step size of decision variables considered in the optimization problem

	N	M	M_{pv}	Cap (kWh)
Minimum value	32	1	100	200
Maximum value	34	10	10000	20000
Step size	1	1	50	50

for the entire year. At each time, the irradiance model is run to evaluate the concentration factor X, which can be used in the PV diode equation to calculate V_{mp}, I_{mp}, and P_{mp}. V_{mp} is used along with an input value of N to evaluate the electrolysis cell operating voltage (V_{cell}), which determines the operating current (I_{cell}) based on Fig. 3.8. The electrolyzer total operating power (P_{e}) and the hydrogen production rate ($V_{\mathrm{H_2}}$) are then evaluated using Equations (3.21) and (3.23). The battery operating state and energy level are then evaluated using (3.25), using an initial SOC value of 50% at t=0.

Battery model initial conditions are defined by setting the maximum and minimum operating limits for the investigated design configuration ($E_{\mathrm{bat,max}} = Cap$, $E_{\mathrm{bat,min}} = (1 - DoD) \times Cap$). For each time step, if $P_{\mathrm{pv}} \geq P_{\mathrm{e}}$, then the battery is charging, and the charge level at the next point in time is calculated using (3.25). Before moving to the next time step, we check if the new battery charge is greater

than the battery capacity, if so, the excess power will be sold to the grid, assuming a converter efficiency of 90%. If $P_{\mathrm{pv}} < P_{\mathrm{e}}$, the battery is in discharge mode, and the new charge level at the next time step is calculated accordingly. The next charge level is checked against the minimum charge constraint to ensure the battery is not depleted beyond the 70% DoD assigned; if this is the case, power must be supplied by the grid (with a 90% converter efficiency). The net grid energy NGE is evaluated at the end of the year, and the annual relative net grid energy $RNGE$ is then calculated using:

$$RNGE = 100 \times \frac{NGE}{24 \times P_e} \tag{3.43}$$

The cost analysis then is performed to determine the total annualized system cost (ACS) and the levelized cost of energy LCE associated with each design configuration.

The design configuration feasible set was refined as the simulation progresses. Because the main target is to achieve an annual net grid energy balance ($RNGE$) within ±5% relative to the daily plant power consumption, redundant design configurations were eliminated during the simulation process. A cutt-off value on the $RNGE$ of ±100% was applied to eliminate redundant design configurations and to reduce simulation time. For example, if a specific configuration (N, M, M_{pv}, Cap) resulted in a high negative value of $RNGE$ (such as $RNGE = -1000\% < -100\%$), the electrolyzer designs with greater power consumption (higher values of M) are ignored for this configuration. In other cases where the simulation of a specific design demonstrated a high positive net-grid energy ($RNGE > 100\%$), higher values of

M_{pv} are ignored for this design. In addition, for infeasible designs where the battery capacity does not meet the minimum requirement to power the electrolyzer for 12 continuous hours, lower values of capacities are considered redundant, and hence, can be ignored. With this, we were able to only simulate 6.4% design configurations among the 2,364,120 feasible set.

Figure 3.9 presents a flowchart of the algorithm implemented for each design configuration considered in the optimization process.

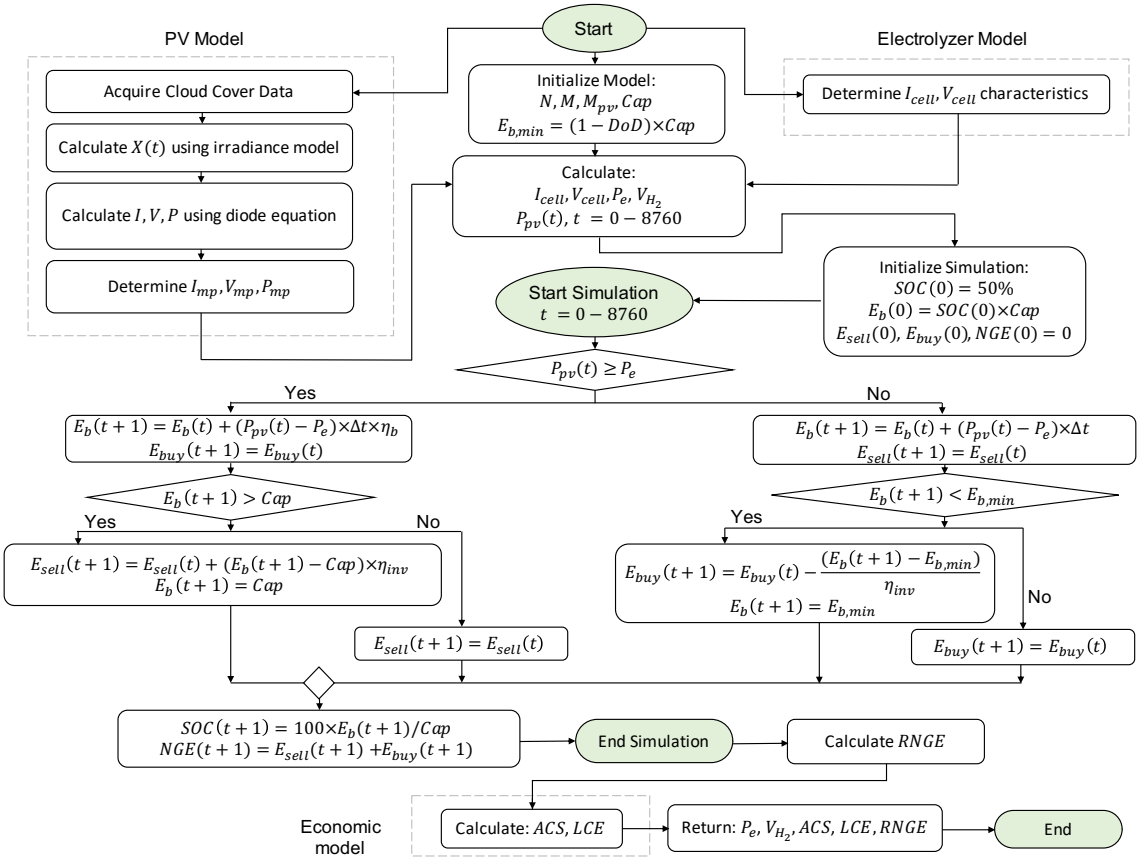

Figure 3.9: Flowchart of the algorithm used for each design configuration considered in the optimization problem.

3.6 Simulation Results

3.6.1 Optimal System Design

The simulation results yielded 179 design configurations with an annual net grid energy ($RNGE$) within ±5% relative to daily electrolyzer power consumption. Among these solutions, 13 were chosen as the Pareto-Frontier for the multi-objective optimization problem and are shown in Figure 3.10. The Pareto-Frontier is a set of non-dominated solutions, and is typically generated for a multi-objective optimization problems, where finding a single best solution is improbable. For each member of this set, no other solution is completely better in terms of optimizing both objective functions. Each point in Figure 3.10 corresponds to a specific design, and is labeled to denote the design configuration.

Figure 3.10 reveals a clear trade-off between the two conflicting objectives: maximizing the hydrogen production rate requires higher system cost. This result is expected since higher plant capacity requires more energy input, hence, higher system physical dimensions. However, we are still able to identify a set of Pareto points that guarantees maximizing the production rate while minimizing the total annual system costs. The 13 Pareto points are reported in Table 3.8.

Because this is a mixed-integer optimization problem in which some of the decision variables can only take integer values, the Pareto front plotted in Figure 3.10 is not smooth. A refined smoother line can be obtained as the step size of the decision variables approaches zero. However, because of the non-linear relation

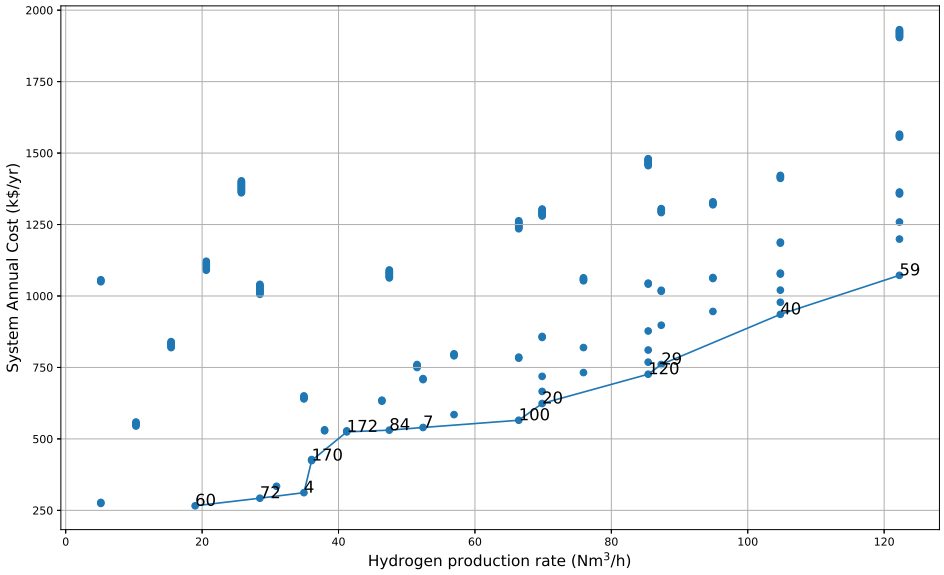

Figure 3.10: Hydrogen production rate and total annual system cost for the 179 design configurations with a yearly relative net grid energy within ±5% relative to daily power consumption, showing the 13 Pareto-Frontier points. The numbered points are the Pareto optimal designs, and are listed in Table 3.8.

between I_{cell} and V_{cell} and their dependency on N, a completely smooth or straight line is highly improbable.

Table 3.8: The set of Pareto points optimizing the multi-objective problem in this analysis (Continued on next page).

Point ID	N	M	Cap (kWh)	M_{pv}	P_e (kW)	V_{H_2} (Nm^3/h)	ACS (k$/y)	LCE ($/kWh)	$RNGE$ (%)	NGE (kWh)	SEC (kWh/Nm^3)
4	32	2	1900	2650	145.2	34.9	311.9	0.192	-4.14	-144.2	4.16
7	32	3	3950	3900	217.9	52.4	540.0	0.229	4.81	251.7	4.16
20	32	4	3800	5300	290.5	69.9	623.9	0.192	-4.14	-288.4	4.16
29	32	5	4450	6650	363.1	87.3	760.3	0.186	1.71	148.7	4.16
40	32	6	5700	7950	435.7	104.8	935.8	0.192	-4.14	-432.7	4.16
59	32	7	6350	9300	508.3	122.2	1072.3	0.188	0.12	14.5	4.16
60	33	2	2500	1350	76.5	19.0	265.9	0.333	4.12	75.7	4.03
72	33	3	2200	2050	114.8	28.5	292.5	0.236	-0.76	-20.9	4.03

Point ID	N	M	Cap (kWh)	M_{pv}	P_e (kW)	V_{H_2} (Nm^3/h)	ACS (k$/y)	LCE ($/kWh)	$RNGE$ (%)	NGE (kWh)	SEC (kWh/Nm^3)
84	33	5	4300	3400	191.3	47.4	530.6	0.260	-1.53	-70.3	4.03
100	33	7	3350	4900	267.8	66.4	565.3	0.188	0.84	53.9	4.03
120	33	9	4300	6300	344.4	85.4	726.3	0.188	-2.28	-188.6	4.03
170	34	7	3650	2500	141.1	36.1	424.2	0.284	-4.93	-167.0	3.91
172	34	8	4750	2850	161.3	41.2	524.6	0.310	-2.78	-107.8	3.91

Examining the values tabulated in Table 3.8 reveals similarities between the points 4, 20, and 40. Since the number of electrolyzer stacks (M) in point 20 is doubled compared to point 4, it follows that the M_{pv} and Cap values are doubled as well to conserve optimality of the design. As a result, the $RNGE$ and LCE are equal for all three designs. This conclusion is significant because it enables the design of arbitrary plant capacities by multiplying a Pareto optimal point by a factor, while guaranteeing the new design still lies within the Pareto front. However, this conclusion cannot be generalized to multiples of N, since the electrolysis cell current-voltage relation is nonlinear, and so would not result in an optimal design. Additionally, for safety requirements (mainly to prevent the current from reaching excessive values), the value of N must be specified based on the PV module output voltage.

Typically, a plant design process begins by specifying a target hydrogen production capacity followed by a detailed economic and technical analysis. Hence, Table 3.8 can be used as a design guide, since it provides a range of possible plant capacities and the optimal design configurations.

Table 3.8 also reveals the specific energy consumption (SEC) values in the electrolyzer unit for each design. The reported values are promising since they are slightly better than the state-of-art commercial electrolyzer values (4.2-4.8 kWh/Nm^3 [57]), demonstrating the potential performance of the Ni-Fe LDH alkaline electrolyzer unit. It is also notable that SEC is affected by the number of cells in each stack of the electrolyzer (N). This can be derived by examining equations (3.21), (3.23), and (3.24), which reveal a dependency of the SEC on the operat-

ing voltage of each cell (V_{cell}). As N increases, V_{cell} decreases, resulting in a slight decline in the SEC value.

On the other hand, Figure 3.11 shows that higher hydrogen production rates yield lower LCE. This can be understood by Equation (3.42), which indicates that increasing the hydrogen production rate requires higher input energy (E_{an}). It should be noted that the increase in (E_{an}) exceeds the observable increase in the PV and battery costs, resulting in a decline in the LCE as the system physical dimensions increase. However, at high hydrogen production capacities, the increase in required battery capacity leads to higher system costs, which can exceed the increase in the annual energy produced throughout the year. Supporting evidence for this conclusion is provided by the slight increase in the LCE value in Figure 3.11(b) between points 29 and 59. These two points are the optimal designs for this graph as they maximize V_{H_2} while minimizing LCE, and they are already a subset of the Pareto Front reported in Table 3.8. The trade-off between the ACS and LCE illustrated in Figure 3.12, resulting in the Pareto front shown in Figure 3.12(b), which is a subset of the Pareto set reported in Table 3.8. This implies that optimizing the systems cost and hydrogen production rate implicitly ensures the LCE is also minimized.

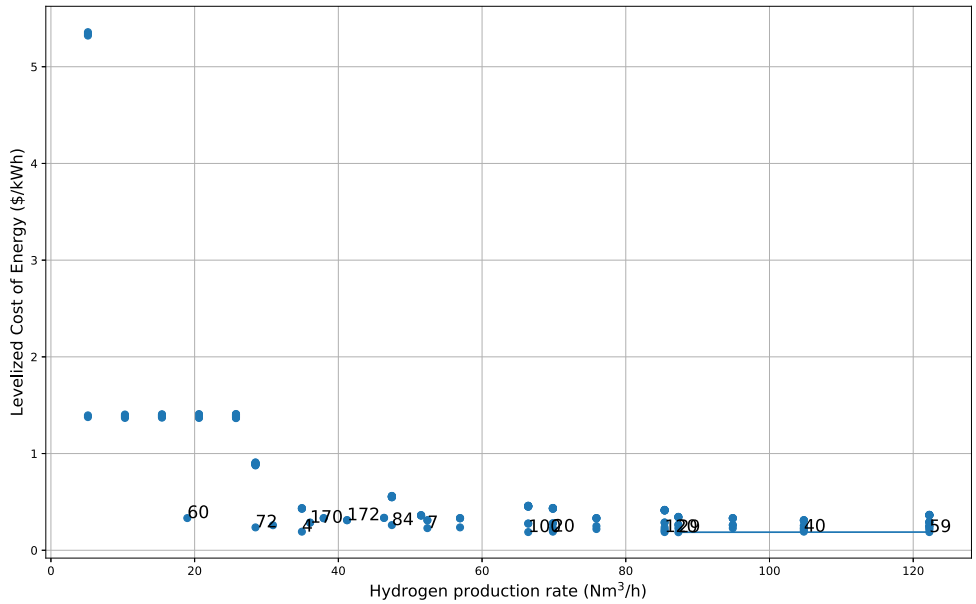

(a)

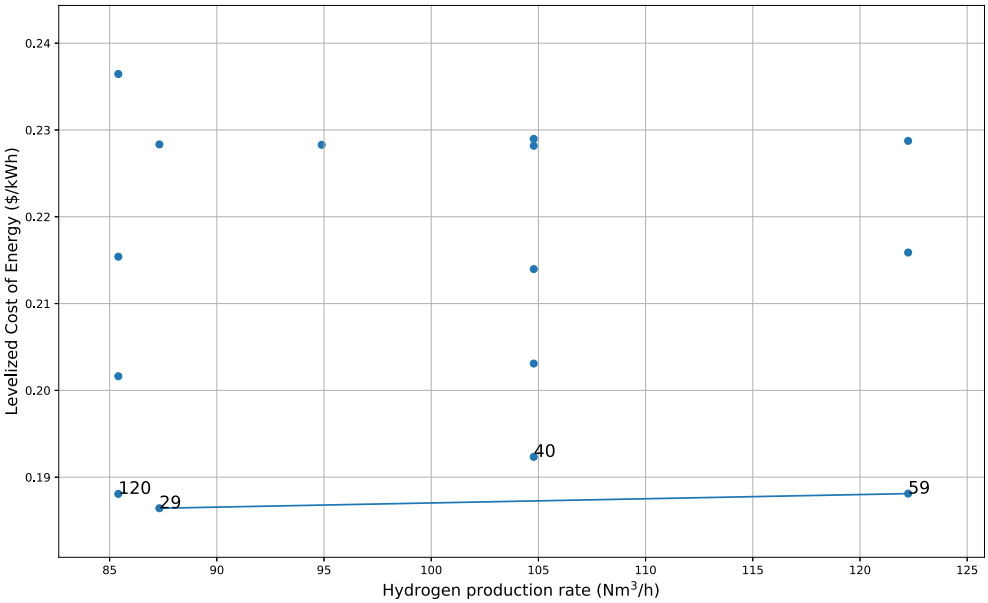

(b)

Figure 3.11: Hydrogen production rate and LCE for the design configurations with an annual net grid energy within ±5% relative to daily power consumption (a), and a closer look on the Pareto front (b). The numbered points are the Pareto optimal designs, and are listed in Table 3.8.

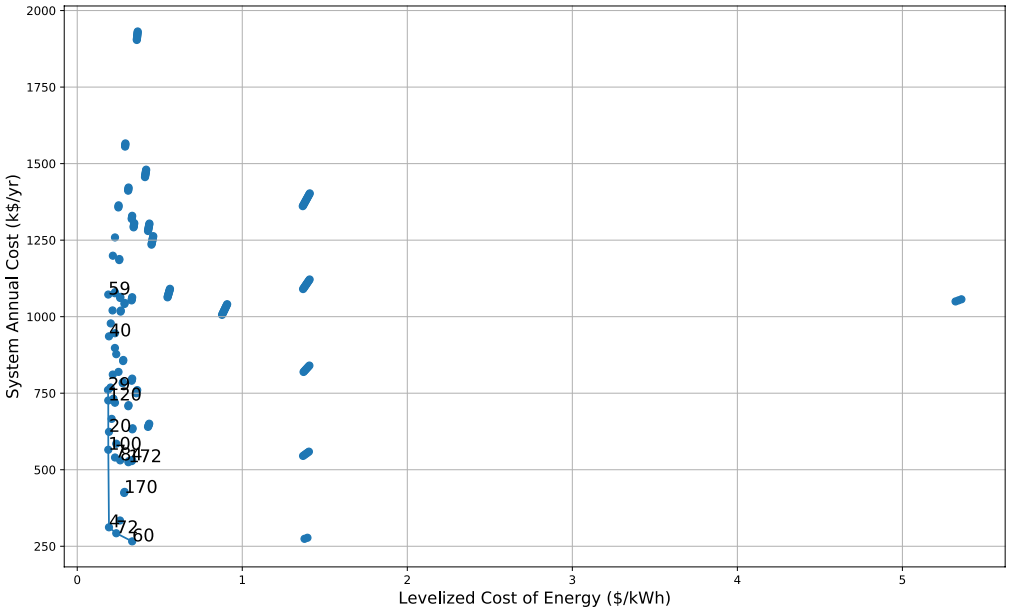

(a)

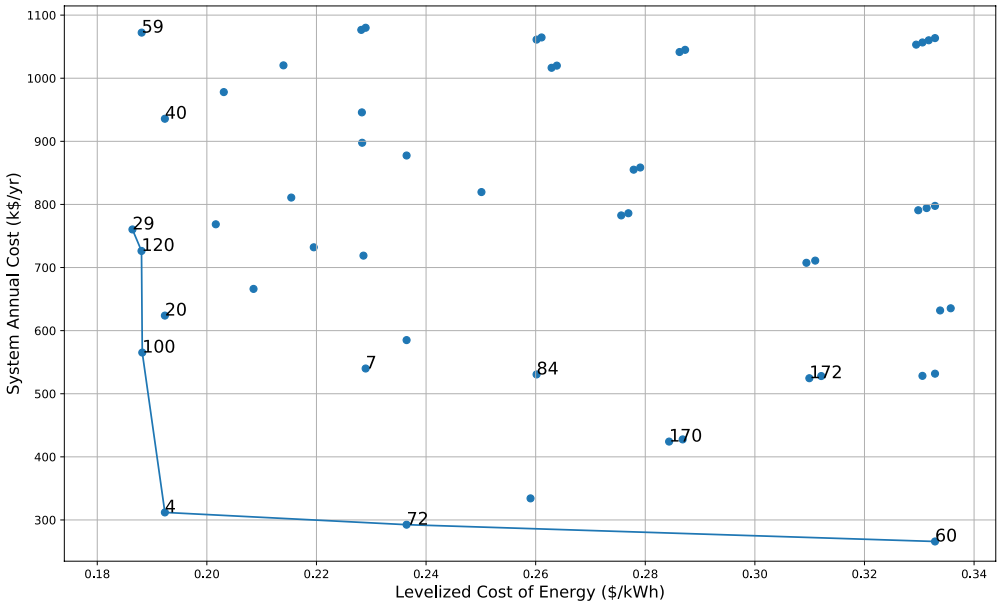

(b)

Figure 3.12: LCE and the annual system cost for the design configurations with a yearly net grid energy within ±5% relative to daily power consumption (a), and a closer look on the Pareto front (b). The numbered points are the Pareto optimal designs, and are listed in Table 3.8.

3.6.2 Optimal Design and Relative Net-Grid Energy

Figures 3.13, 3.14, and 3.15 show the spread of the optimal solutions, plotted as red circles, with respect to the $RNGE$. Since the electricity cost is less expensive, one would expect that optimal solutions minimizing the cost are always associated with negative values of $RNGE$ close to the cut-off value of -5%. However, Figure 3.14 reveals the independency of the Pareto optimal set costs on the $RNGE$. That is, the optimal Pareto points are well spread over the entire $RNGE$ domain of $\pm 5\%$. This assures the effectiveness of the analysis in finding the optimal system design.

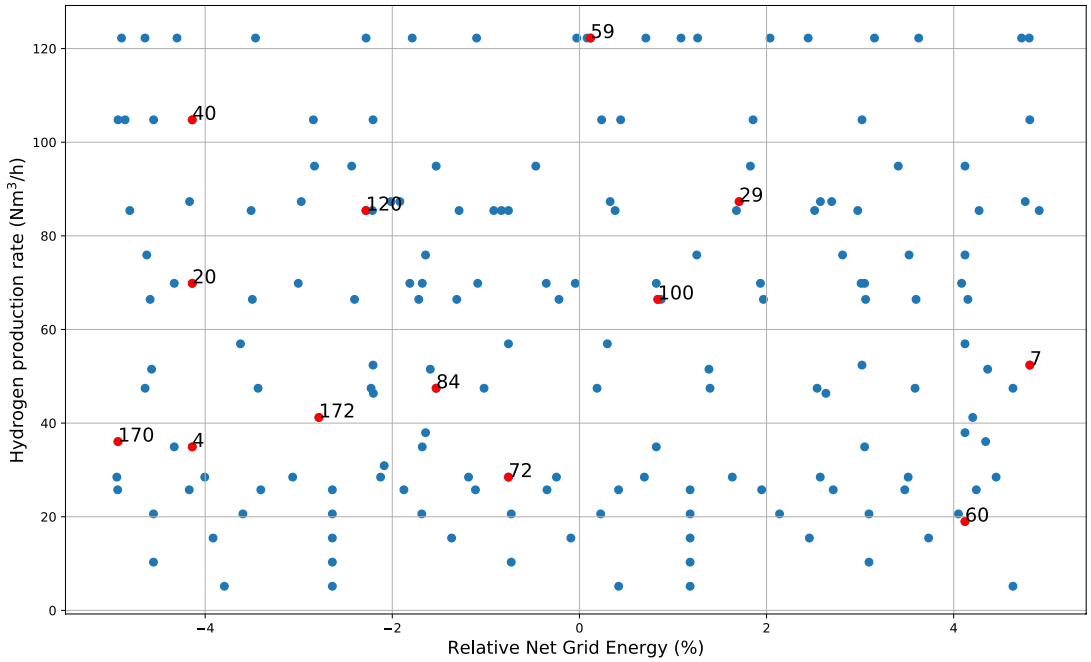

Figure 3.13: Hydrogen production rate and the relative net grid energy, showing the 13 Pareto-Frontier points in red.

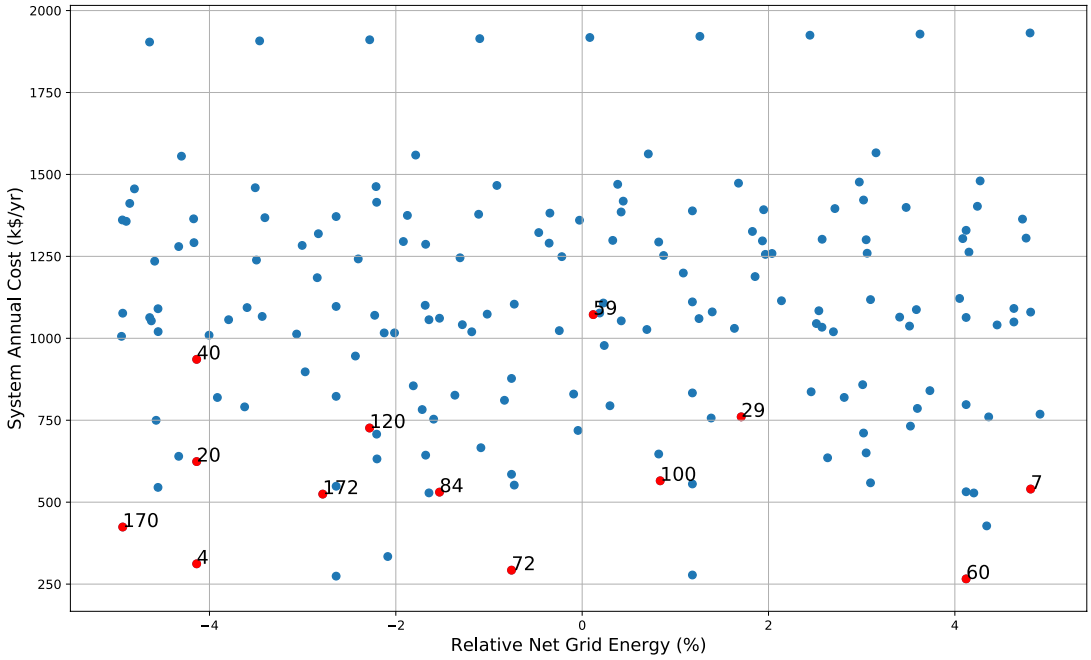

Figure 3.14: Annual cost and the relative net grid energy, showing the 13 Pareto-Frontier points in red.

The spread of solution set can be attributed to the minimum constraint forced on the battery capacity, requiring it to power the electrolyzer for at least 12 continuous hours. This ensures that the system does not compensate the battery capacity and withdraws enormous amounts of energy from the grid to minimize the total cost.

Another reason for the solution spread over the entire $RNGE$ domain of $\pm 5\%$ is the trade-off between the M_{pv} and Cap. To illustrate, let us consider the two optimal points 29 and 120 in Tables 3.8 and 3.9. These two points have approximately the same hydrogen production rate (87.3 and 85.4 Nm^3/h, respectively), however the cost break down for each design is slightly different. Looking at Table 3.9, if we

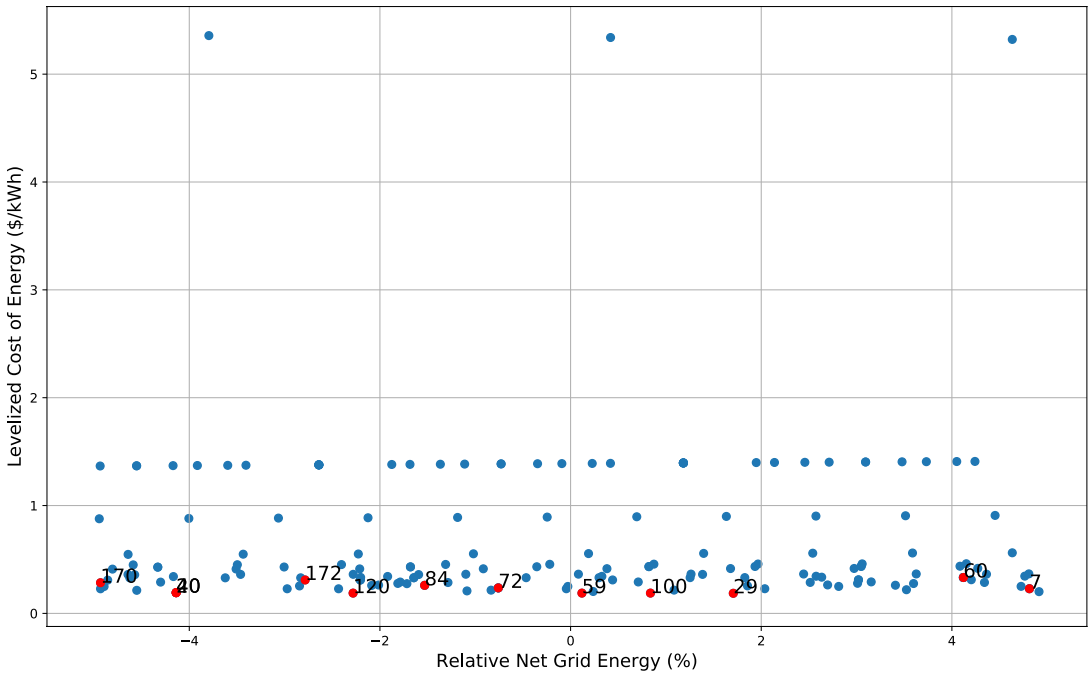

Figure 3.15: LCE and the relative net grid energy, showing the 13 Pareto-Frontier points in red.

only consider the annualized costs associated with PV modules and battery bank, both points agree on having a PV cost % that is higher than battery cost %. However, point 29 has a slightly higher PV cost % than point 120, and hence point 29 is associated with a positive $RNGE$ value. This analysis is also valid for the points (20, 100) and (7, 84) shown in Table 3.9. This is only true in cases where both points demonstrate higher PV cost % than battery cost %, or higher battery cost % than PV cost %. In other cases where the two points do not report similar PV-battery cost breakdown, no definite conclusion can be derived. This case corresponds to points (4, 170) in Table 3.9, where both points report a negative $RNGE$ value.

Table 3.9: Cost breakdown for selected optimal points based on PV and Battery costs only.

Point ID	PV Cost %	Battery Cost %	$RNGE$ %
29	55.5	44.5	1.71
120	55.1	44.9	-2.28
20	53.8	46.2	-4.14
100	55.0	45.0	0.84
7	45.2	54.8	4.81
84	39.8	60.2	-1.53
4	53.8	46.2	-4.14
170	36.4	63.6	-4.93

However, we cannot derive a similar conclusion just by comparing the actual values of the battery capacity and number of PV modules. The relation between $RNGE$ and both M_{pv} and Cap is rather complicated and cannot be generalized. Nevertheless, a detailed discussion on the isolated effect of each of these variables on the $RNGE$ and other objective functions will be discussed in section 3.6.3.

Figure 3.16 shows a 3D plot combining the hydrogen production rate, ACS, and LCE, with Pareto Front points shown in red. These point form the Pareto plane that minimize LCE and ACS, while maximizing V_{H_2}.

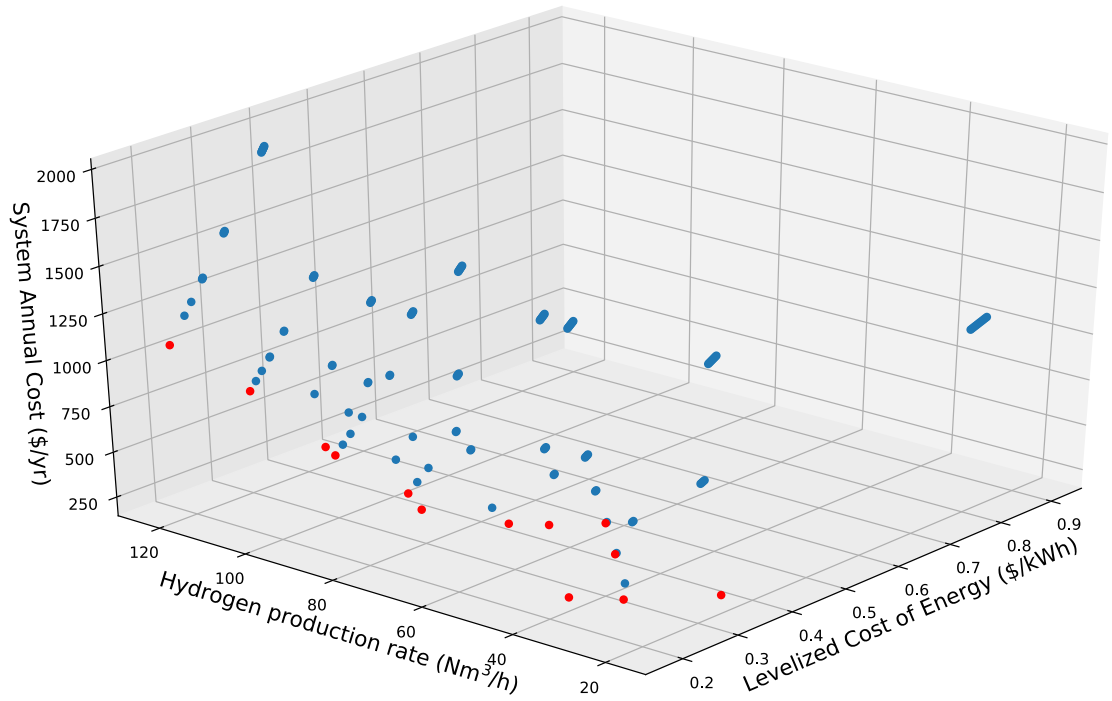

Figure 3.16: Hydrogen production rate, annual cost, and levelized cost of energy, with the optimal Pareto points in red.

3.6.3 Influence of Decision Variables

In the following, we discuss the effect of each decision variable on the ACS, V_{H_2}, LCE, and $RNGE$, while keeping other variables fixed.

3.6.3.1 Battery Capacity

Obviously, increasing the battery capacity for a specific fixed design will increase the ACS. The LCE will increase as well, because increasing the capacity only increases the numerator in Equation (3.42). However, V_{H_2} will not be influenced as it only depends on the electrolyzer design variables N, M.

The influence of battery capacity on the $RNGE$ depends on the system design elements that remain fixed. That is, the influence mainly depends on the system energy requirements and energy supplied by the PV modules. To illustrate, if the energy generated by PV modules is insufficient (relatively low M_{pv} values), then the $RNGE$ increases as Cap increases, as seen in Figures 3.17(a) and 3.17(b). This is because higher Cap values will be associated with higher initial battery energy at the start of the simulation (since SOC_i=50%). Hence, less energy will be supplied by the grid throughout the year, causing the $RNGE$ to reach higher values. This also is confirmed by the fact that designs with higher Cap maintain higher SOC values throughout the year, requiring less grid energy.

For fixed designs with relatively high energy production, the $RNGE$ behavior will be different, as shown in Figures 3.17(c) and 3.17(d). As the Cap increases, the initial battery energy increases, and the SOC will be maintained at higher values throughout the simulation. Hence, the system will tend to sell energy to the grid rather than to acquire. The $RNGE$ behavior will then reach a maximum before it starts decreasing. As the Cap excessively increases, it will be more challenging to fully charge the battery, and less energy will be sold, as energy is only sold to the grid when the battery is fully charged.

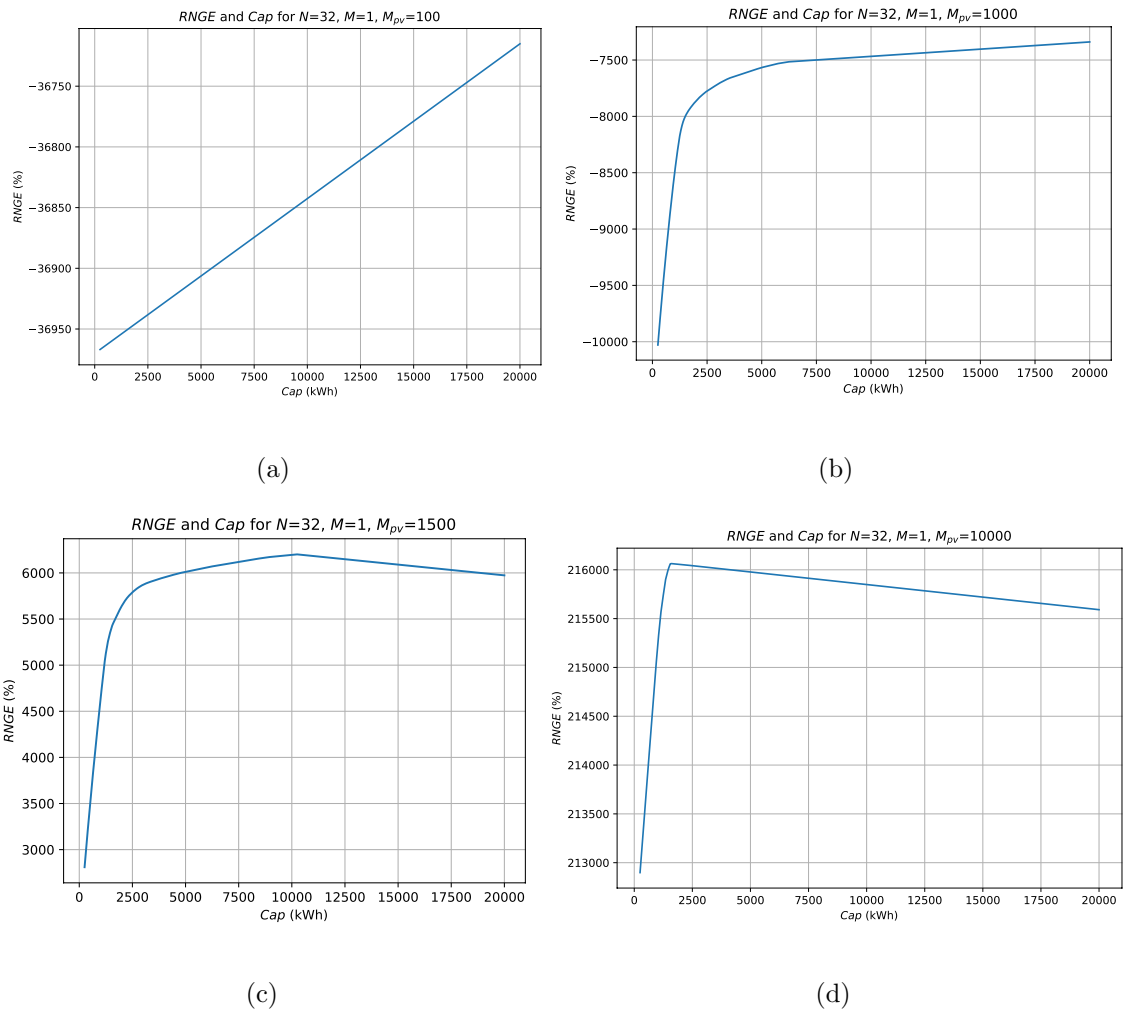

(a) (b)

(c) (d)

Figure 3.17: Effect of changing the battery capacity at fixed system design, for M_{pv} of 100 (a), 1,000 (b), 1,500 (c), and 10,000 (d).

3.6.3.2 Number of PV modules

For a fixed design, the LCE will decrease exponentially as M_{pv} increases. This can be supported by examining Equation (3.42), where both $C_{\mathrm{a,pv}}$ and E_{an} increase linearly with increasing M_{pv}. The $RNGE$ will increase as a result of increasing M_{pv}, as more energy will be produced, and hence, for a fixed design, more energy will be sold to the grid and less energy is purchased from the grid. Similar to Cap, M_{pv} does not affect the hydrogen production rate, as it is assumed to be solely dependent on the electrolyzer design.

For the system annualized cost, Figure 3.18 shows an increasing trend of the cost with increasing M_{pv}, hitting a minimum at lower M_{pv} values. At small M_{pv} values, the system in incapable of generating sufficient power for the electrolyzer, and an enormous amount of energy must be supplied by the grid, causing high total system cost. As M_{pv} slightly increases, the ability to meet the system's energy requirements increases. At this point, the increase in the PV system cost is less than the decrease in the cost of electricity supplied by the grid, leading to a reduced overall system cost. The curve reaches a minimum, before the additional PV cost added to the system off-sets the savings in electricity costs, and as a result, the total cost starts rising. This behavior is independent of the system design kept fixed (i.e., similar behavior is noticed for all fixed values of N, M, and Cap).

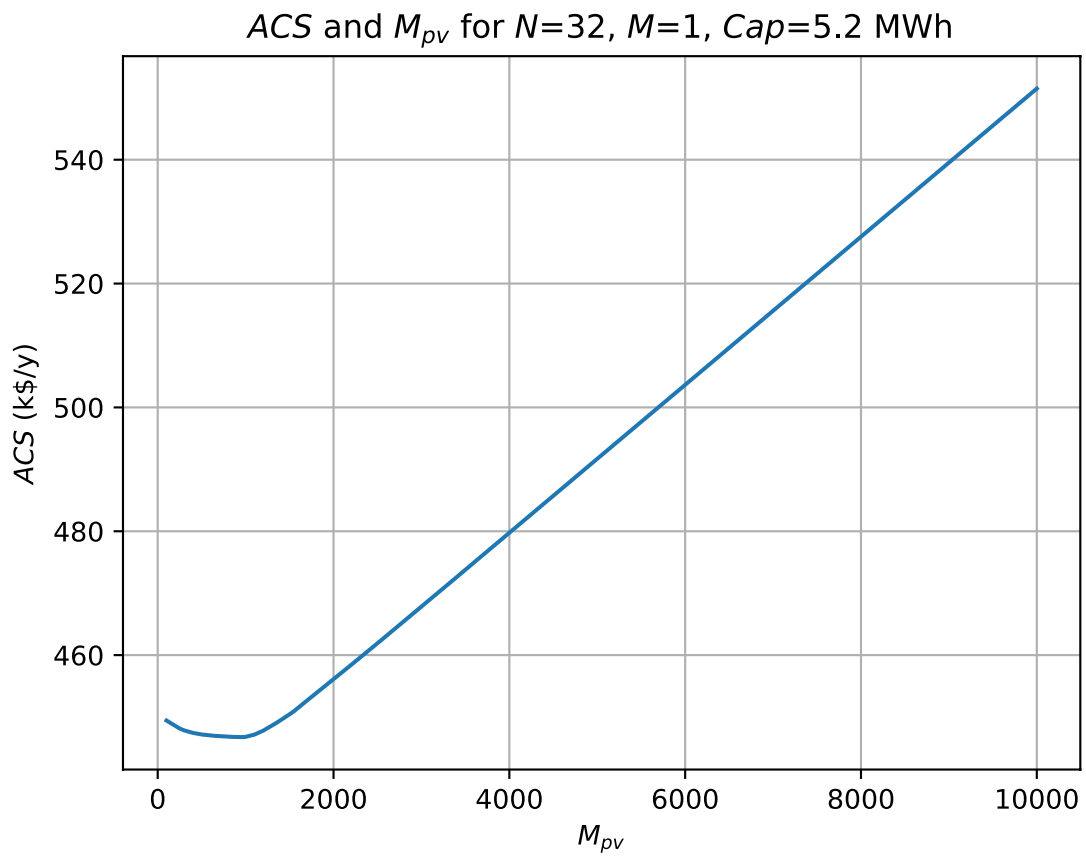

Figure 3.18: Effect of number of PV modules M_{pv} on the total annualized system cost ACS.

3.6.3.3 Electrolyzer Cells and Stacks

Looking at Equation (3.42), the electrolyzer design variables N and M have no direct influence on the LCE. However, this conclusion is for a fixed system design, and should not be confused by the relation between $V_{\mathrm{H_2}}$ and LCE in Figure 3.11, where the entire system design is different for each point in the plot.

As the number of stacks M increases, both $V_{\mathrm{H_2}}$ and ACS increase linearly. Nevertheless, the $RNGE$ decreases exponentially. This exponential decrease is due

to the linear increase in both NGE and P_e in Equation 3.43.

For an increasing number of cells N, the behavior is reversed. Increasing N will reduce V_{cell}, and consequently I_{cell} will reduce according to Figure 3.8. P_e and V_{H_2} will be more influenced by the decrease in I_{cell} and V_{cell}, rather than the slight increase in N values (from N=32 to 33 or 34). As less P_e is needed for higher N values, the $RNGE$ will increase and ACS will decrease.

3.6.4 Performance of Optimal Design

For each point in the Pareto Front, we can investigate the its performance throughout the year. We take point 4 in Table 3.8 as an example in this section. Figure 3.19 shows the relation between P_e, P_{pv}, and E_b. It can be observed that the battery charges in cases where the PV power is in excess, and discharges when PV power is insufficient. The battery SOC is shown in Figure 3.20.

Figure 3.21 reveals the energy sold to and bought from the grid, in addition to the NGE and battery energy. As seen, energy is sold to the grid at fully charged states, and is acquired from the grid when the battery reaches its DoD. Figure 3.22 combines the grid energy and the coupled system operating conditions (P_e, P_{pv}, and E_b).

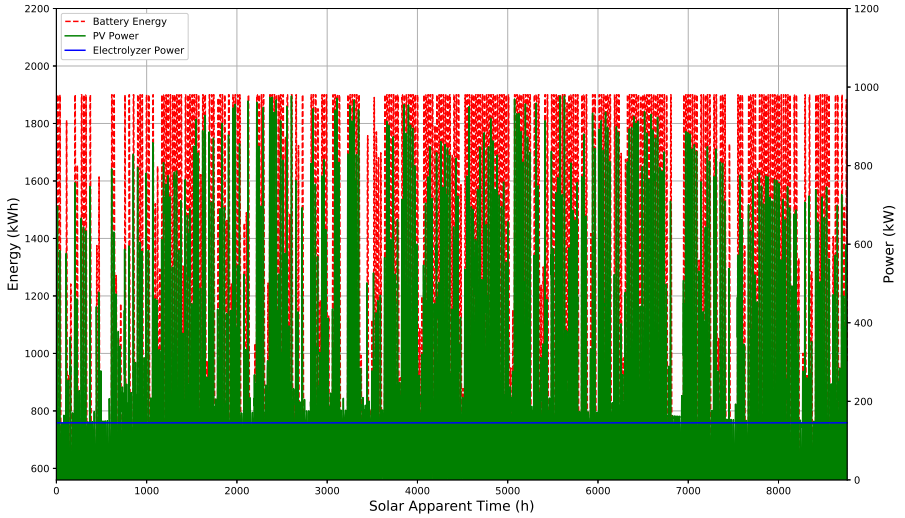

(a)

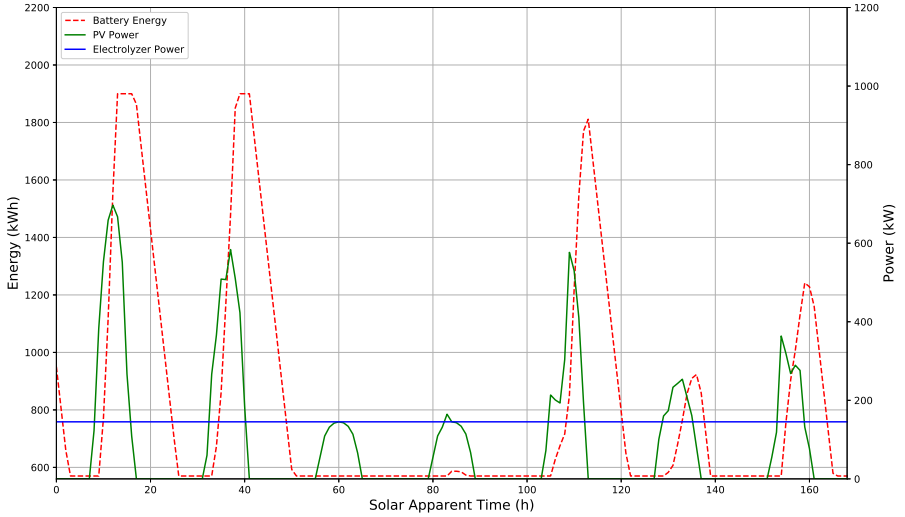

(b)

Figure 3.19: Simulation results for point 4 in Table 3.8 showing P_e, P_{pv}, and E_b for 2017 (a), and the first week of 2017 (b).

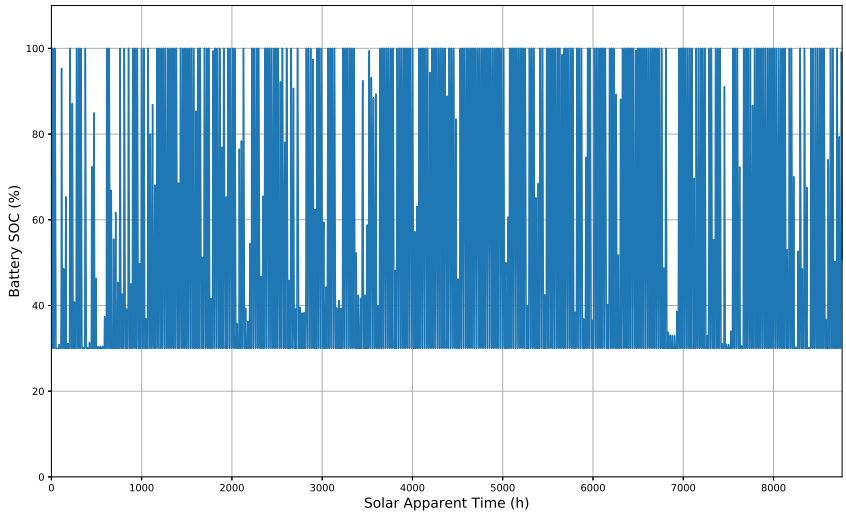

(a)

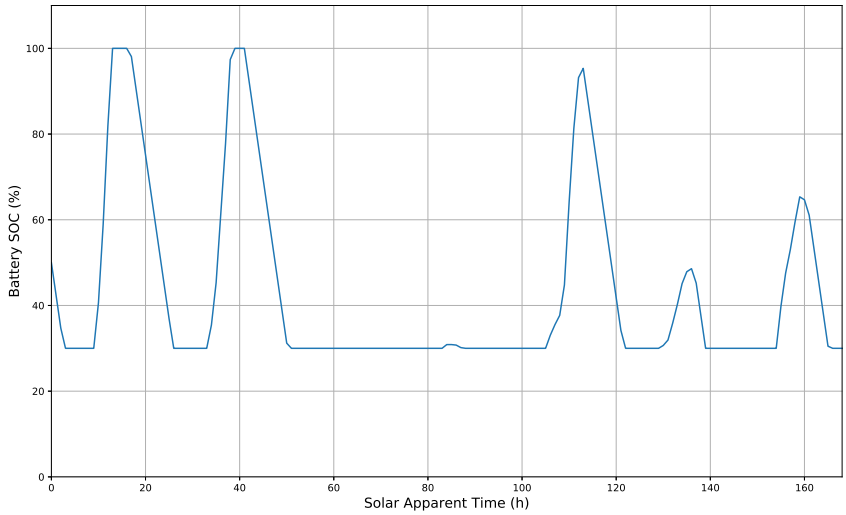

(b)

Figure 3.20: Simulation results for point 4 in Table 3.8 showing the battery *SOC* for 2017 (a), and the first week of 2017 (b).

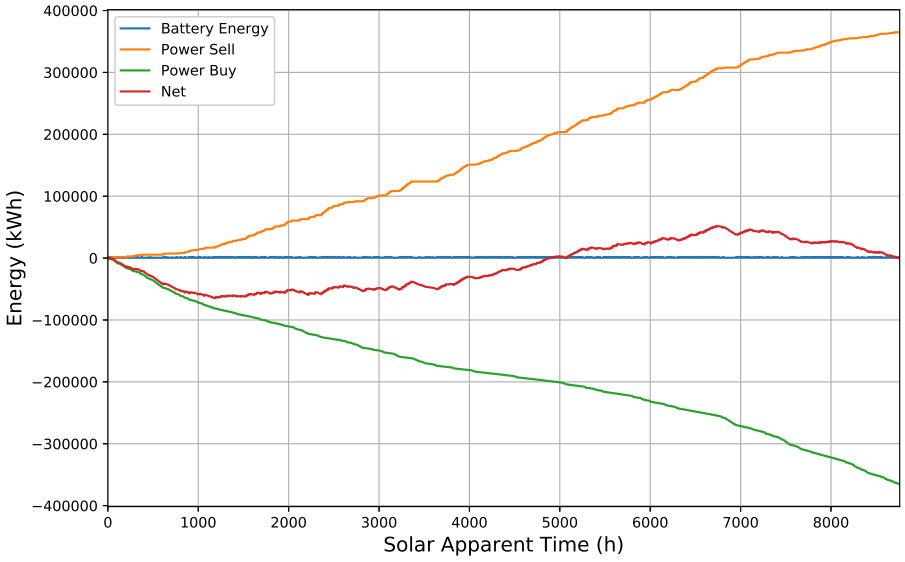

(a)

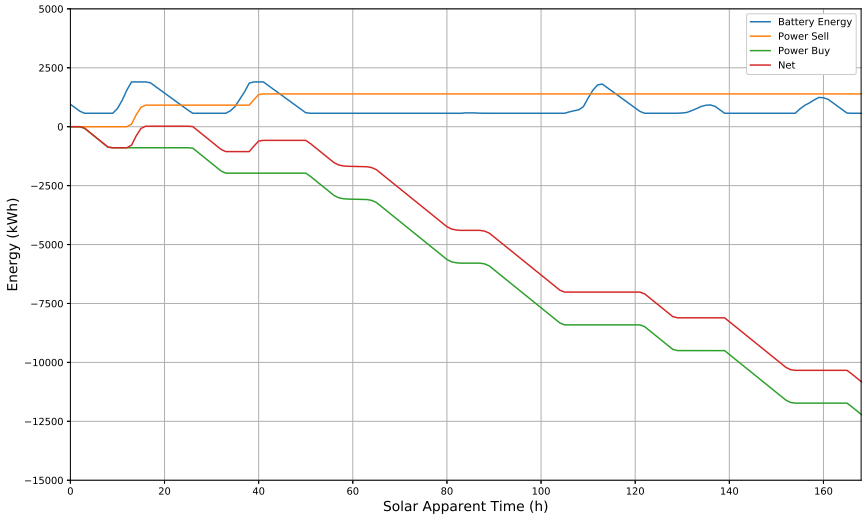

(b)

Figure 3.21: Simulation results for point 4 in Table 3.8 showing the battery energy and the grid energy for 2017 (a), and the first week of 2017 (b).

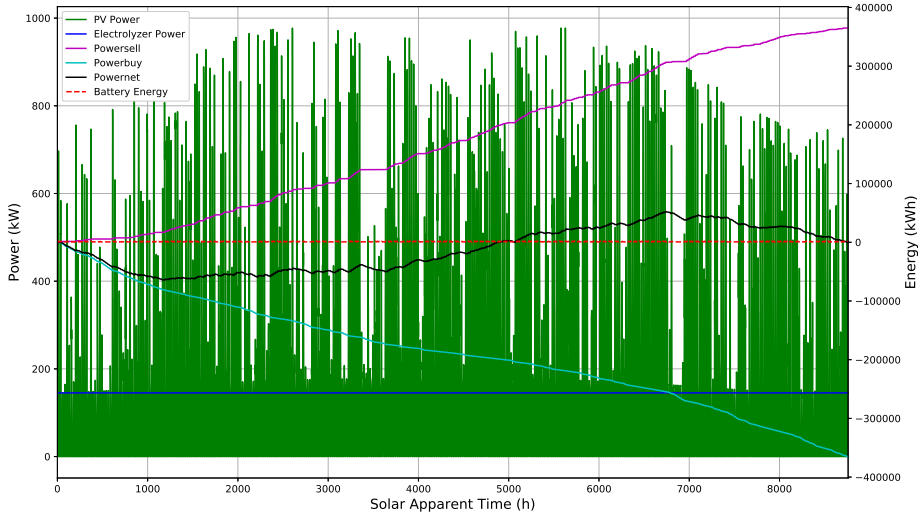

(a)

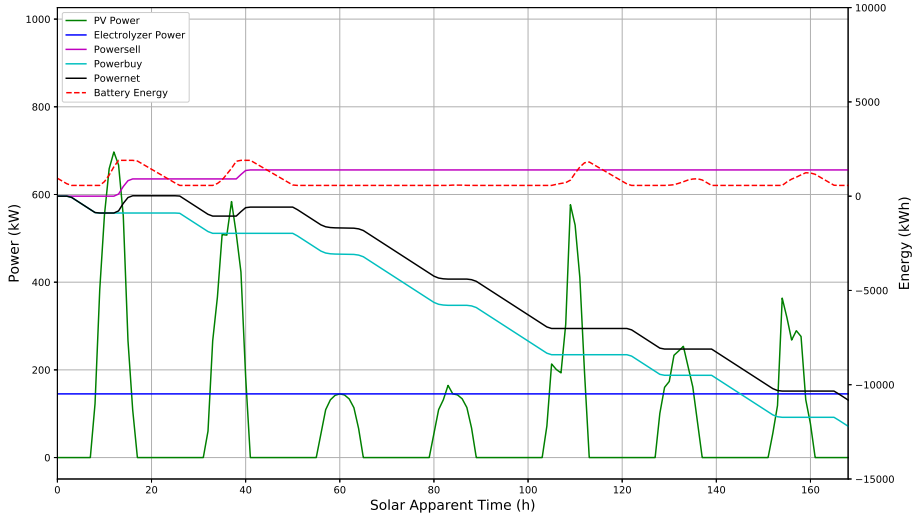

(b)

Figure 3.22: Simulation results for point 4 in Table 3.8 for 2017 (a), and the first week of 2017 (b).

3.6.5 Safety Considerations in Hydrogen Systems

This work mainly focuses on addressing some of the challenges and limitations in hydrogen production stage. In addition to production, challenges in hydrogen storage, transportation, and distribution must be tackled simultaneously before the hydrogen economy can function at grid-scale level applications [3]. If this work is to be expanded to include other components such as hydrogen storage or delivery, then safety is an important issue to address.

One of the main challenges in hydrogen transportation and distribution is that the current infrastructure is mainly used to transport natural gas. As a transition step toward a completely hydrogen based supply chain, hydrogen can be added and mixed with natural gas to be transferred in the current pipelines [3]. The main uncertainty is the amount of hydrogen that can be added safely, which depends on the characteristics of the natural gas and the design of appliances used in a specific region [3].

Additionally, hydrogen storage can face safety issues regarding overpressure, underpressure, overflow, or even dangerously low levels, which might induce risks of combustion, explosion, pressure build-up, implosion or hydrogen leak [67]. As such, prevention strategies must be followed and implemented in the operation and design of integrated hydrogen storage systems [67].

3.7 Concluding Remarks

In this chapter, a coupled PV-electrolysis-battery system was studied with the goals of determining optimal system design and operation. The model takes into account the weather variations in College Park, MD for the calendar year 2017. The primary aim of the analysis was to identify the system design characteristics (N, M, M_{pv}, and Cap) that maximizes hydrogen production rate, minimizes the system's annualized cost and the levelized cost of energy, while maintaining an annual net grid energy within $\pm 5\%$ relative to daily electrolyzer power consumption.

The simulation results yielded 179 design configuration with a $RNGE$ $\pm 5\%$, 13 of the designs were identified as Pareto optimal designs for this problem. The influence of the design variables on the objective functions was investigated and is presented in this work.

This computational platform to model integrated solar hydrogen systems can be extended to more complex hybrid systems. For instance, the use of wind power as a renewable energy source can be added to this problem to promote further sustainability, and drive the system to off-grid limits.

Chapter 4: MC Simulation for Optimal Solar Cells Configuration

4.1 Introduction

Current trends in electrical power generation and energy storage research highlight the promise of micro- and nano-scale devices [68], [69]. Performance issues arise when integrating these devices, as design and performance mismatch between devices can cause deviation from the expected performance in a highly nonlinear manner. The tera- and giga-scale levels of integration necessary for producing and storing macroscopic levels of energy from nano-scale devices necessitates device integration strategies that are resilient to the inevitable faults and variability that will arise in the individual devices. Thus, new computational tools are needed to support the design, integration, and (advanced) manufacturing of these energy systems. As a first step towards developing simulation-based design tools for the integration of nano-scale energy devices, we will examine the problem of determining the optimal strategy to integrate a large number of photovoltaic (PV) solar cells under shady or faulty conditions as a proxy for our primary simulation objective.

When one cell in an array of PV cells is shaded, its voltage polarity may reverse resulting in power consumption instead of production, leading to hotspot formation, reduced overall power, and even PV module damage. Bypass diodes can be used to

route current around shaded or faulty cells to partially recover the lost performance. In this chapter, we focus on modeling tools useful for optimizing the number and placement of these diodes within a PV cell array.

Singh et al. [70] investigated the effect of random shading levels and positions on the output of a PV cell array; the potential benefits of bypass diodes, however, was not included in their analysis. Vemuru et al. [71] examined the effect of random shading of a PV array on the output power. They concluded that the power of the randomly shaded array is reduced significantly when no bypass diodes are used, as apposed to having a fixed number of bypass diodes in the array for the same shading conditions. Silvestre et al. [72] used Pspice simulation environment to study the effect of bypass diodes configuration on a PV module. They presented a finite number of simulation cases in which selected cells were shaded, and demonstrated how the configuration of a fixed number of bypass diodes affected the results.

4.1.1 Motivation and Goals

In this work, we introduce the stochastic effects and uncertainty generated by shading, which simulate real-life operating conditions. The objective of this work is to develop computational tools to identify optimal configurations when integrating a large number of PV cells under shady or faulty conditions. Monte Carlo simulation is used to simulate a PV cell module under partially shaded conditions and to find the optimal number of bypass diodes needed to minimize performance losses. We use event-driven Monte Carlo simulation, in which each event corresponds to a separate

shading case. The number of shaded cells and their position in the PV module are considered random variables, and the model is evaluated under different shading levels (25%, 50%, 75%, and 100% shading).

An advantage of our choice of MC simulation is that it can be extended to any shading pattern caused by trees, falling tree leaves, standing birds, close-by buildings, and even passing clouds, once the statistical distribution of the shading effect is known or can be approximated. In nano-scale manufacturing, partial shading can occur due to tilting in some of the nano-wire solar cells, causing partial blocking of solar energy. Another potential mismatch in nano-scale devices is the production of defected nano-wire solar cells, with a short circuit junction. These cases correspond to a solar cell with low R_{sh} value, causing a short circuit in the nano-wire solar cell, and overall power losses.

Combining the cost attribute in addition to performance measures generates a multi-objective optimization problem. We then combine the information entropy weight and Technique for Order Preference by Similarity to Ideal Solution (TOPSIS) methods to make the final decision and determine the optimal number of bypass diodes under the different shading cases considered. The entropy weight is a computational technique that can be applied to evaluate the objective weight of each of the attributes in a multi-criteria decision making problem. The TOPSIS method uses the computed weights to evaluate the final optimal design, characterized by the shortest relative distance from the positive ideal solution.

4.2 Model and Simulation

4.2.1 Governing Equation

The PV module considered in this analysis consists of 96 PV cells connected in series, where strings (subsets of the full set) of solar cells are wired in parallel to a bypass diode, as shown in Figure 4.1. The diode equation, (4.1), is used to model the current-voltage characteristics of each PV cell.

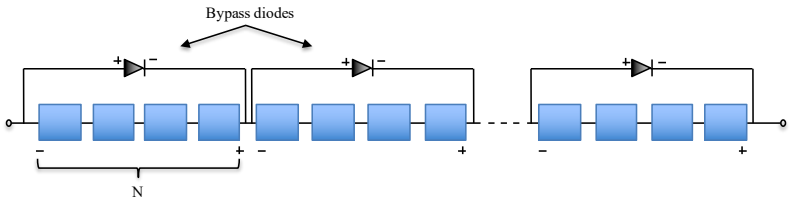

Figure 4.1: Schematic diagram showing the system's configuration.

$$I = XI_{ph} - I_o \left[\exp\left(\frac{V + IR_s}{mV_{th}} \right) - 1 \right] - \frac{V + IR_s}{R_{sh}} \tag{4.1}$$

The diode equation parameters and their values used in this analysis are presented in Table 4.1. These parameters are intended to approximate a SunPower SPR-X21-345 PV module. In this analysis, four shading cases are considered: 25% (X=0.75), 50% (X=0.5), 75% (X=0.25), and 100% (X=0).

4.2.2 Calculating the Current of a String with Shaded Cells

To calculate the current I of a string of N solar cells wired in series, we define C_t as a counter for the number of shaded solar cells in the string, V_1 the voltage

Table 4.1: Diode equation parameters and their values used in this analysis.

Parameter	Definition	Value	Unit
I_{ph}	Photocurrent	3.921	A/m^2
I_o	Dark saturation current	3.870×10^{-12}	A/m^2
R_s	Series resistance	1.092×10^{-2}	Ω
R_{sh}	Shunt resistance	2.516×10^{3}	Ω
m	Diode ideality factor	1	
V_{th}	Theoretical voltage ($k_B T/q$)	2.57×10^{-2}	V

across an unshaded cell, and V is the total voltage of the string to find the voltage across a shaded cell as

$$V_{sh} = \frac{V - (N - C_t)V_1}{C_t} \tag{4.2}$$

Substituting V_1 and V_{sh} into Equation (4.1), we obtain two diode equations: one for unshaded cells, and the other for shaded cells. Because the currents of PV cells connected in series are identical, we can set both equations equal to each other to find one function of I, V, and V_1. This equation can be solved numerically to find current values I at different string voltages V. However, for every V value we assume, we have two unknowns I and V_1; and hence, a two-dimensional iterative loop is used. For a known value of V, first we assume $I = 0$, and using a Newton procedure, we find the corresponding value of V_1. Then the inner loop will re-

calculate the value of I as a function of the previous V_1 and I values. The next iteration would use the most recent V_1 and I values to solve for V_1 again, and then I is re-examined in the inner loop. The stopping criteria corresponds to reaching converged V_1 and I values. This procedure is carried out for each value in the vector V, resulting in $I - V$ characteristics data for the shaded string.

4.2.3 Model Algorithm

We developed a MATLAB program to calculate the output maximum power point for each run of the MC simulation. At the start of the program, we have a vector of values for the voltage ranging from 0 to the open circuit voltage of the string.

For each value of the voltage, we calculate its corresponding current following the model presented in sections 4.2.1 and 4.2.2. The string with the highest current will force the shaded strings to pass the same current. As a result, the bypass diode will be activated if the shaded strings resulted in a negative voltage.

4.2.4 Monte Carlo Simulation

For the MC simulation, both the number of partially shaded solar cells and their position are considered random variables. The number of shaded cells is assumed to follow a uniform distribution ranging from 1 to 5 shaded cells, and the position of the shaded cells also follows a uniform distribution ranging from cell 1 to cell 96. The position of the shaded cell is important since it determines the number

of shaded cells in each string, and the number of strings with shaded cells.

For each run of the MC simulation, we start by initiating a vector of values for the voltage ranging from 0 to the open circuit voltage of the string. The main idea is to determine at each voltage point whether the bypass diode for each string would be activated or not under the shading conditions randomly provided. We assigned 4 shading cases: 25%, 50%, 75%, and 100% shading, and for each of these cases we have 12 scenarios representing the number of bypass diodes used (1, 2, 3, 4, 6, 8, 12, 16, 24, 32, 48, 96), and for every scenarios, we run the MC simulation for 10,000 shading events, each with different random number of shaded cells and random positions, to obtain the module maximum power point P_{mp}, its standard deviation, and standard error. A summary of the simulation algorithm for each run of the MC simulation is presented in the SysML activity diagram in Figure 4.2.

4.2.5 Effect of Bypass Diodes and Shading Factor

To examine the effect of the number of bypass diodes on the module performance, the module is simulated with only one shaded cell. As seen in Figure 4.3, as the number of bypass diodes increases, the output power will also increase, minimizing performance losses compared to the unshaded case. To illustrate, as more bypass diodes are used, the number of cells in each string is reduced. Hence, with partial shading across the PV module, fewer PV cells are bypassed resulting in P-V characteristics that are closer to the unshaded case. Hence, the effect of the shaded cell is minimized with increasing the number of bypass diodes.

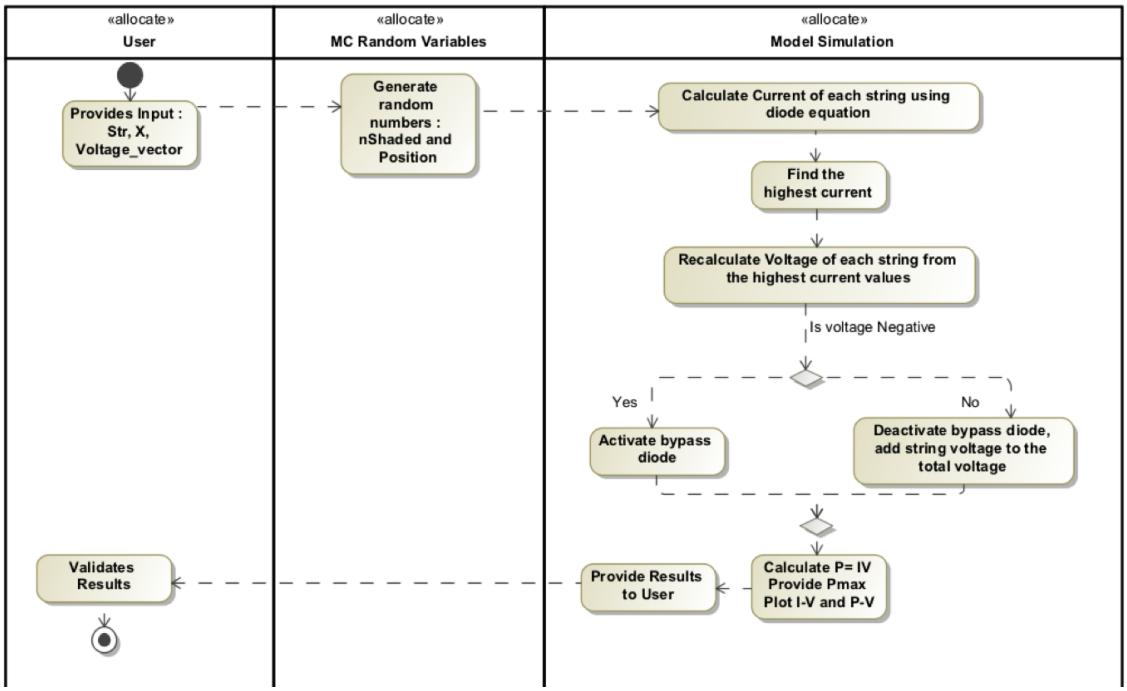

Figure 4.2: Algorithm used for each run of the MC simulation. Note that "Str" is the number of strings, which is equal to the number of bypass diodes.

As seen in Figure 4.3, the incorporation of bypass diodes in the PV module has an effect on the shape of the P-V characteristics. With partial shading of the PV module, multiple power peaks result, in contrast to one global peak in the unshaded case. The multiple peaks result form the addition of the voltage of the strings with shaded cells to the total module voltage. In other words, they result from the deactivation of the bypass diodes when the string with shaded cells is able to supply the required load current.

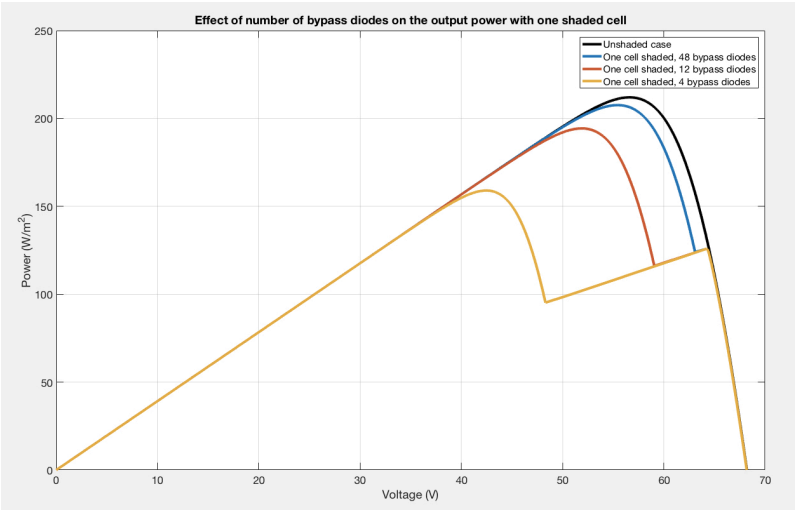

(a)

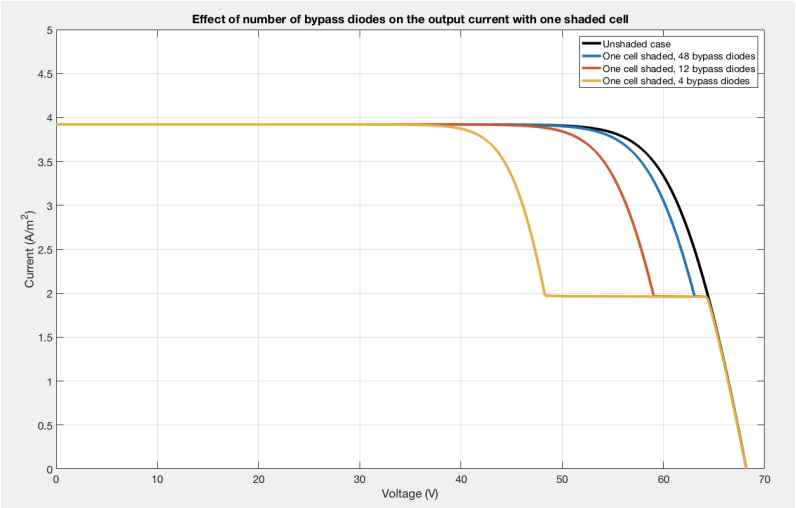

(b)

Figure 4.3: Effect of the number of bypass diodes on the module output power (a) and current (b) with one shaded cells and 50% shading (X=0.5).

Figure 4.4 demonstrates the effect of shading on the performance of the PV module, using a fixed number of bypass diodes. As the shaded cell experience greater shading %, its ability to deliver the required load current decreases, as presented in 4.4(b). This is shown in the delay in de-activating the bypass diodes, causing the second peak in the P-V module to occur at higher voltages.

The first power peak is generated by the unshaded strings, and the second peak is formed by both the unshaded and shaded strings. The highest peak represents the global peak, and it is taken as the P_{mp} for the module at this operating condition and design configuration. The position of this global peak is dependent on the shading conditions and number of bypass diodes. Generally, lighter shadings results in the global peak to be found at higher voltages, but it is also dependent on the number of bypassed diodes. Figure 4.5 demonstrates the effect of shading and number of bypass diodes on the position of the global peak. For a module with 2 bypass diodes, as in Figure 4.5(a), both 25% and 50% shading cases exhibit maximum power peaks at higher voltages. However, when the number of bypass diodes is raised to 6, as in Figure 4.5(b), we observe a shift of the global power peak of the 50% shading case to lower voltage.

4.2.6 MC Simulation Results

Figure 4.6 presents the mean value of P_{mp} that results with an increasing number of MC simulation cases for 8 bypass diodes and 50% shading. 10,000 runs were performed to ensure the mean value has reached steady state with an acceptable

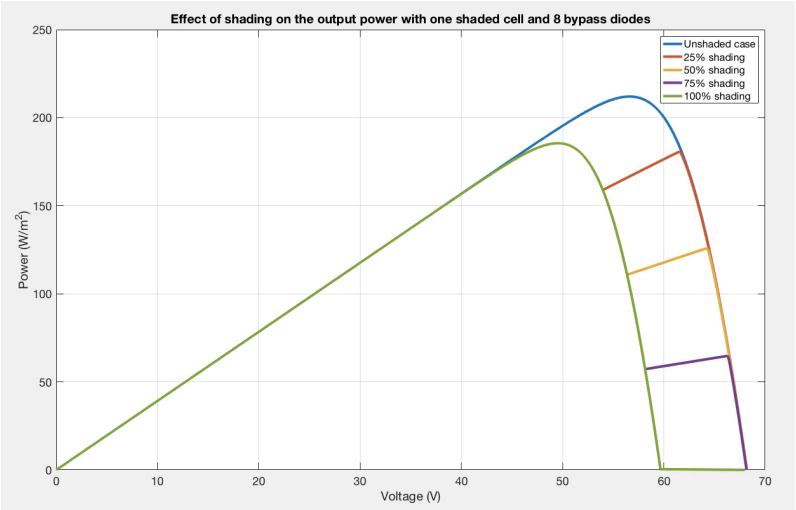

(a)

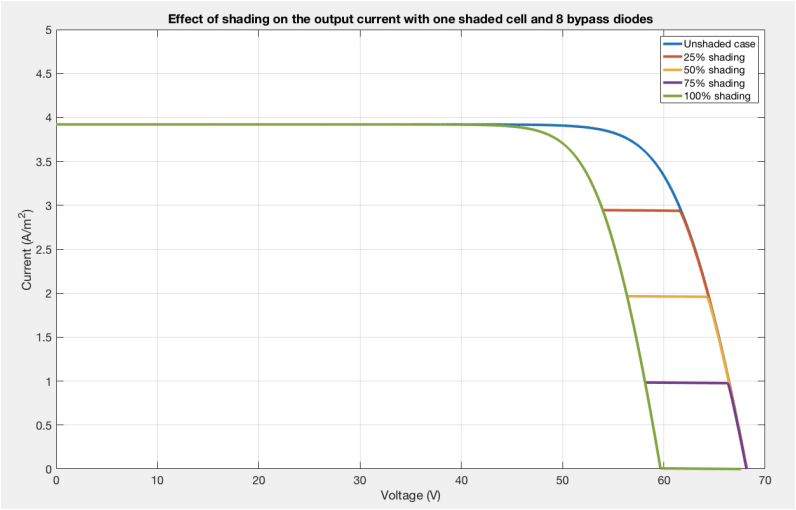

(b)

Figure 4.4: Effect of the shading factor on the output module power (a) and current (b) with one shaded cell and 8 bypass diodes.

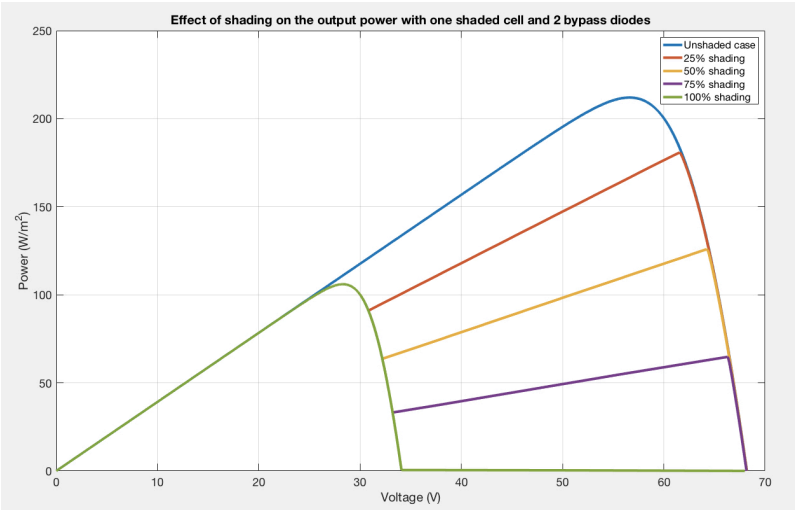

(a)

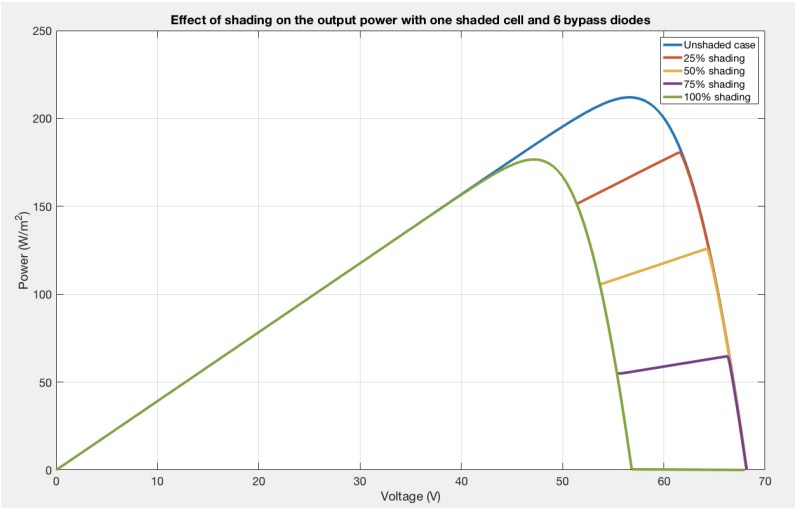

(b)

Figure 4.5: Effect of the shading factor and bypass diodes on the position of the global power peak, with 2 bypass diodes in (a), and 6 bypass diodes in (b).

standard error value.

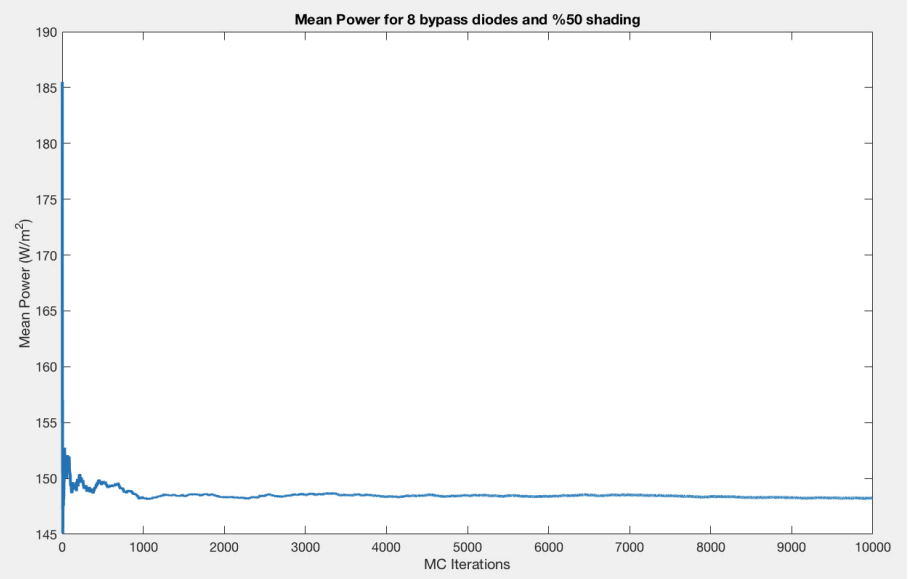

Figure 4.6: Evolution of mean value of P_{mp} with MC runs.

The MC simulation results are provided in Figure 4.7 and Tables 4.2, 4.3, 4.4, and 4.5. As the number of bypass diodes increases, the mean value of maximum power also increases. This result is expected since increasing the number of diodes decreases the number of illuminated PV cells bypassed. The effect of increasing the bypass diodes is substantial as the degree of shading increases. Even though increasing the number of bypass diodes may lead to increased leakage currents in these diodes, this negative effect is compensated by the positive benefits of adding the diodes [73].

Table 4.2: MC simulation results for the 25% shading case.

Bypass diodes	Mean P_{mp} (W/m^2)	SD P_{mp} (W/m^2)	SE P_{mp} (W/m^2)
1	179.98	0.506	5.1×10^{-3}
2	179.97	0.499	5.0×10^{-3}
3	179.97	0.498	5.0×10^{-3}
4	179.98	0.507	5.1×10^{-3}
6	179.97	0.500	5.0×10^{-3}
8	180.73	2.104	2.1×10^{-2}
12	181.93	5.108	5.1×10^{-2}
16	183.95	6.456	6.5×10^{-2}
24	188.30	8.145	8.1×10^{-2}
32	192.79	7.705	7.7×10^{-2}
48	199.05	5.246	5.3×10^{-2}
96	205.48	2.640	2.6×10^{-2}

Table 4.3: MC simulation results for the 50% shading case.

Bypass diodes	Mean P_{mp} (W/m^2)	SD P_{mp} (W/m^2)	SE P_{mp} (W/m^2)
1	125.15	0.42	4.2×10^{-3}
2	125.14	0.41	4.1×10^{-3}
3	128.96	7.02	7.0×10^{-2}
4	132.02	13.81	1.4×10^{-1}
6	139.71	18.46	1.8×10^{-1}
8	147.76	21.10	2.1×10^{-1}
12	164.15	19.26	1.9×10^{-1}
16	175.49	14.79	1.5×10^{-1}
24	186.88	10.29	1.0×10^{-1}
32	192.99	7.76	7.8×10^{-2}
48	199.18	5.35	5.4×10^{-2}
96	205.47	2.66	2.7×10^{-2}

Table 4.4: MC simulation results for the 75% shading case.

Bypass diodes	Mean P_{mp} (W/m^2)	SD P_{mp} (W/m^2)	SE P_{mp} (W/m^2)
1	64.47	0.24	2.4×10^{-3}
2	79.10	19.91	2.0×10^{-1}
3	86.66	31.55	3.2×10^{-1}
4	101.86	34.65	3.5×10^{-1}
6	126.33	33.21	3.3×10^{-1}
8	143.60	27.14	2.7×10^{-1}
12	163.89	19.46	1.9×10^{-1}
16	175.24	14.91	1.5×10^{-1}
24	186.92	10.19	1.0×10^{-1}
32	192.80	7.80	7.8×10^{-2}
48	199.10	5.29	5.3×10^{-2}
96	205.44	2.67	2.7×10^{-2}

Table 4.5: MC simulation results for the 100% shading case.

Bypass diodes	Mean P_{mp} (W/m^2)	SD P_{mp} (W/m^2)	SE P_{mp} (W/m^2)
1	0.19	0.112	1.1×10^{-3}
2	37.08	50.463	5.0×10^{-1}
3	70.55	49.042	4.9×10^{-1}
4	94.72	43.672	4.4×10^{-1}
6	125.93	33.550	3.4×10^{-1}
8	143.69	27.344	2.7×10^{-1}
12	164.15	19.306	1.9×10^{-1}
16	175.32	14.783	1.5×10^{-1}
24	186.86	10.274	1.0×10^{-1}
32	192.84	7.755	7.8×10^{-2}
48	199.11	5.244	5.2×10^{-2}
96	205.39	2.670	2.7×10^{-2}

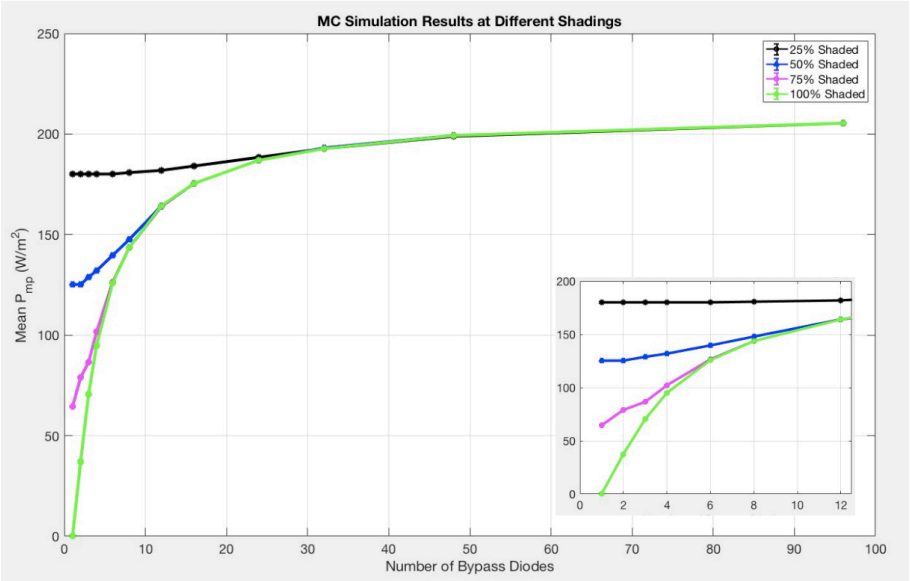

Figure 4.7: MC results for the four shading cases illustrating the benefit of increasing the number of bypass diodes.

4.3 Optimal Number of Bypass Diodes

Because the MC simulation clearly demonstrate the effectiveness of using the highest number of bypass diodes (Figure 4.7), we next consider the cost of adding the bypass diodes to make the final design decision. The cost of each diode is set to be \$1.5, an approximate cost of TEXAS INSTRUMENTS SM74611 smart bypass diodes. The TEXAS INSTRUMENTS smart diodes are chosen over the conventional P-N junction diodes or Schottky diodes to mitigate the issues with current leakage, power dissipation, and temperature rise in the bypass diodes [73].

The cost attribute added to the performance metric produces a multi-objective optimization problem. A trade-off design problem results from the cost of adding the bypass diodes versus the increase in the power generated under shady conditions.

For typical multi-criteria decision making problems, weights are assigned to each attribute to reflect the importance of the attribute and its influence on the optimal solution. Generally, two main categories of weighting methods exist: subjective and objective methods [74]. The subjective methods are based on the experience and preference of the decision maker [74]. The objective method determines the weights using mathematical models, and then evaluates the optimal solution using the computed weights [74].

4.3.1 Information Entropy Weight

One of the most well-known objective methods is the information entropy weight method. In information theory, entropy is the amount of uncertainty a criteria or attribute offers represented by a probability distribution [74], [75]. For a specific attribute, the entropy weight represents how much alternatives are similar to each other. The higher the entropy, the smaller the diversity in information carried by a specific attribute, the less information this attribute provides, and hence, the less weight is given to this attribute in the decision making process [74].

The entropy method typically starts by setting an $(m \times n)$ decision matrix, with m alternatives, and n attributes considered. In this work, $m = 12$, representing the 12 bypass diodes cases, and $n = 2$, with two attributes to consider: performance and cost.

$$D = \begin{bmatrix} x_{11} & x_{12} & \dots & x_{1n} \\ x_{21} & x_{22} & \dots & x_{2n} \\ \vdots & \vdots & \ddots & \vdots \\ x_{m1} & x_{m2} & \dots & x_{mn} \end{bmatrix} \tag{4.3}$$

where D is the decision matrix, and x_{ij} is the matrix element corresponding to the value of attribute j (i.e., mean P_{mp} and cost), for alternative i. To allow for comparison across the attributes, the information offered in matrix D must be normalized for each attribute to form the P matrix [75] with:

$$p_{ij} = \frac{x_{ij}}{\sum_{i=1}^{m} x_{ij}}, \quad j \in [1, \dots, n] \tag{4.4}$$

where p_{ij} are the normalized decision matrix (P) entries. The entropy (e), diversity (d), and objective weight (w) associated with each attribute then can be calculated using [75]:

$$e_j = \frac{-1}{\ln(m)} \sum_{i=1}^{m} p_{ij} \ln(p_{ij}), \quad i \in [1, \dots, m], \quad j \in [1, \dots, n] \tag{4.5}$$

$$d_j = 1 - e_j, \quad j \in [1, \dots, n] \tag{4.6}$$

$$w_j = \frac{d_j}{\sum_{j=1}^{n} d_j}, \quad j \in [1, \dots, n] \tag{4.7}$$

with $\sum_{j=1}^{n} w_j = 1$. The higher the diversity (d) in information contained by a criteria, the more important the criteria is for the problem, the higher the weight (w) assigned to this criteria.

4.3.2 Selection of Optimal Alternative

After determining the weights associated with the performance and cost attribute, we then apply the Technique for Order Preference by Similarity to Ideal Solution (TOPSIS) method to make the final design decision. TOPSIS was first proposed by Hwang and Yoon [76], and it is a ranking method based on calculating the Euclidean distances of a number of possible alternatives. This technique is based on identifying the positive ideal solution (PIS) and negative idea solution (NIS). The PIS is a chosen alternative that maximizes the benefit attributes and minimizes the cost attributes, whereas NIS is the opposite. The optimal alternative is characterized by the shortest distance to the PIS and the farthest distance from the NIS. The PIS (A^+) and NIS (A^-) are determined using [75]

$$A^+ = \left(p_1^+, p_2^+, \ldots, p_n^+\right) \tag{4.8}$$

$$A^- = \left(p_1^-, p_2^-, \ldots, p_n^-\right) \tag{4.9}$$

$$p_j^+ = \left\{\max_i p_{ij}, \quad j \in J_1; \quad \min_i p_{ij}, \quad j \in J_2\right\} \tag{4.10}$$

$$p_j^- = \left\{\min_i p_{ij}, \quad j \in J_1; \quad \max_i p_{ij}, \quad j \in J_2\right\} \tag{4.11}$$

where J_1 and J_2 are the sets of benefit criteria and cost criteria, respectively. The distance then can be evaluated as

$$d_i^+ = \sqrt{\sum_j^n w_j \left(p_j^+ - p_{ij}\right)^2}, \quad i \in [1, \ldots, m] \tag{4.12}$$

$$d_i^- = \sqrt{\sum_j^n w_j \left(p_j^- - p_{ij}\right)^2}, \quad i \in [1, \ldots, m] \tag{4.13}$$

and the relative closeness of each alternative to the ideal solution is

$$\zeta_i = \frac{d_i^-}{d_i^+ + d_i^-}, \quad i \in [1, \ldots, m] \tag{4.14}$$

The higher ζ_i, the better the alternative. Hence, the alternative with the highest relative closeness is chosen as the optimal solution.

4.3.3 Entropy Weight and TOPSIS Results

In the following section, we apply the entropy weight method combined with the TOPSIS method to evaluate the optimal design chosen for each shading case considered.

4.3.3.1 25% Shading

Using Table 4.2, and a diode cost of \$1.5, we construct the normalized decision matrix P, where each row represent a design alternative (number of bypassed diodes in Table 4.2), and the first and second column represent the PV module power and bypass diode cost, respectively.

$$P_{25\%} = \begin{bmatrix} 8.063 \times 10^{-2} & 3.968 \times 10^{-3} \\ 8.063 \times 10^{-2} & 7.937 \times 10^{-3} \\ 8.063 \times 10^{-2} & 1.190 \times 10^{-2} \\ 8.063 \times 10^{-2} & 1.587 \times 10^{-2} \\ 8.063 \times 10^{-2} & 2.381 \times 10^{-2} \\ 8.097 \times 10^{-2} & 3.175 \times 10^{-2} \\ 8.151 \times 10^{-2} & 4.762 \times 10^{-2} \\ 8.241 \times 10^{-2} & 6.349 \times 10^{-2} \\ 8.436 \times 10^{-2} & 9.524 \times 10^{-2} \\ 8.637 \times 10^{-2} & 1.270 \times 10^{-1} \\ 8.917 \times 10^{-2} & 1.905 \times 10^{-1} \\ 9.206 \times 10^{-2} & 3.810 \times 10^{-1} \end{bmatrix} \tag{4.15}$$

$$A^{+} = \begin{bmatrix} 9.206 \times 10^{-2} & 3.968 \times 10^{-3} \end{bmatrix} \tag{4.16}$$

$$A^{-} = \begin{bmatrix} 8.063 \times 10^{-2} & 3.810 \times 10^{-1} \end{bmatrix} \tag{4.17}$$

The entropy, diversity, and weight of each attribute is

$$e = \begin{bmatrix} 9.996 \times 10^{-1} & 7.513 \times 10^{-1} \end{bmatrix} \tag{4.18}$$

$$d = \begin{bmatrix} 3.958 \times 10^{-4} & 2.487 \times 10^{-1} \end{bmatrix} \tag{4.19}$$

$$w = \begin{bmatrix} 1.589 \times 10^{-3} & 9.984 \times 10^{-1} \end{bmatrix} \tag{4.20}$$

The distance and relative closeness of each alternative to the ideal solution are calculated and presented in Table 4.6.

Table 4.6: TOPSIS results for the 25% shading case.

Bypass diodes	d_i^+	d_i^-	ζ_i
1	4.553×10^{-4}	3.767×10^{-1}	9.988×10^{-1}
2	3.991×10^{-3}	3.727×10^{-1}	9.894×10^{-1}
3	7.943×10^{-3}	3.688×10^{-1}	9.789×10^{-1}
4	1.190×10^{-2}	3.648×10^{-1}	9.684×10^{-1}
6	1.983×10^{-2}	3.569×10^{-1}	9.474×10^{-1}
8	2.776×10^{-2}	3.489×10^{-1}	9.263×10^{-1}
12	4.362×10^{-2}	3.331×10^{-1}	8.842×10^{-1}
16	5.948×10^{-2}	3.172×10^{-1}	8.421×10^{-1}
24	9.120×10^{-2}	2.855×10^{-1}	7.579×10^{-1}
32	1.229×10^{-1}	2.538×10^{-1}	6.737×10^{-1}
48	1.864×10^{-1}	1.903×10^{-1}	5.053×10^{-1}
96	3.767×10^{-1}	4.555×10^{-4}	1.208×10^{-3}

The optimal solution for the 25% shading case corresponds to a PV module with 1 bypass diode, as seen in Table 4.6.

4.3.3.2 50% Shading

Similarly, using Table 4.3, we construct the normalized decision matrix P for the 50% shading case.

$$P_{50\%} = \begin{bmatrix} 6.509 \times 10^{-2} & 3.968 \times 10^{-3} \\ 6.508 \times 10^{-2} & 7.937 \times 10^{-3} \\ 6.706 \times 10^{-2} & 1.190 \times 10^{-2} \\ 6.866 \times 10^{-2} & 1.587 \times 10^{-2} \\ 7.265 \times 10^{-2} & 2.381 \times 10^{-2} \\ 7.684 \times 10^{-2} & 3.175 \times 10^{-2} \\ 8.537 \times 10^{-2} & 4.762 \times 10^{-2} \\ 9.126 \times 10^{-2} & 6.349 \times 10^{-2} \\ 9.719 \times 10^{-2} & 9.524 \times 10^{-2} \\ 1.004 \times 10^{-1} & 1.270 \times 10^{-1} \\ 1.036 \times 10^{-1} & 1.905 \times 10^{-1} \\ 1.069 \times 10^{-1} & 3.810 \times 10^{-1} \end{bmatrix} \tag{4.21}$$

$$A^{+} = \begin{bmatrix} 1.069 \times 10^{-1} & 3.968 \times 10^{-3} \end{bmatrix} \tag{4.22}$$

$$A^{-} = \begin{bmatrix} 6.508 \times 10^{-2} & 3.810 \times 10^{-1} \end{bmatrix} \tag{4.23}$$

The entropy, diversity, and weight of each attribute is

$$e = \begin{bmatrix} 9.932 \times 10^{-1} & 7.513 \times 10^{-1} \end{bmatrix} \tag{4.24}$$

$$d = \begin{bmatrix} 6.770 \times 10^{-3} & 2.487 \times 10^{-1} \end{bmatrix} \tag{4.25}$$

$$w = \begin{bmatrix} 2.650 \times 10^{-2} & 9.735 \times 10^{-1} \end{bmatrix} \tag{4.26}$$

The distance and relative closeness of each alternative to the ideal solution are calculated and presented in Table 4.7. Similar to the 25% shading, the 50% shading case optimal solution also corresponds to a PV module with 1 bypass diode, as seen in Table 4.7.

4.3.3.3 75% Shading

Equation (4.27) represents the normalized decision matrix for the 75% shading case.

Table 4.7: TOPSIS results for the 50% shading case.

Bypass diodes	d_i^+	d_i^-	ζ_i
1	6.800×10^{-3}	3.720×10^{-1}	9.820×10^{-1}
2	7.847×10^{-3}	3.680×10^{-1}	9.791×10^{-1}
3	1.016×10^{-2}	3.641×10^{-1}	9.728×10^{-1}
4	1.329×10^{-2}	3.602×10^{-1}	9.644×10^{-1}
6	2.035×10^{-2}	3.524×10^{-1}	9.454×10^{-1}
8	2.784×10^{-2}	3.446×10^{-1}	9.252×10^{-1}
12	4.321×10^{-2}	3.289×10^{-1}	8.839×10^{-1}
16	5.878×10^{-2}	3.133×10^{-1}	8.420×10^{-1}
24	9.007×10^{-2}	2.820×10^{-1}	7.579×10^{-1}
32	1.214×10^{-1}	2.506×10^{-1}	6.737×10^{-1}
48	1.840×10^{-1}	1.880×10^{-1}	5.054×10^{-1}
96	3.720×10^{-1}	6.801×10^{-3}	1.796×10^{-2}

$$P_{75\%} = \begin{bmatrix} 3.736 \times 10^{-2} & 3.968 \times 10^{-3} \\ 4.584 \times 10^{-2} & 7.937 \times 10^{-3} \\ 5.023 \times 10^{-2} & 1.190 \times 10^{-2} \\ 5.904 \times 10^{-2} & 1.587 \times 10^{-2} \\ 7.322 \times 10^{-2} & 2.381 \times 10^{-2} \\ 8.323 \times 10^{-2} & 3.175 \times 10^{-2} \\ 9.499 \times 10^{-2} & 4.762 \times 10^{-2} \\ 1.016 \times 10^{-1} & 6.349 \times 10^{-2} \\ 1.083 \times 10^{-1} & 9.524 \times 10^{-2} \\ 1.117 \times 10^{-1} & 1.270 \times 10^{-1} \\ 1.154 \times 10^{-1} & 1.905 \times 10^{-1} \\ 1.191 \times 10^{-1} & 3.810 \times 10^{-1} \end{bmatrix} \tag{4.27}$$

$$A^{+} = \begin{bmatrix} 1.191 \times 10^{-1} & 3.968 \times 10^{-3} \end{bmatrix} \tag{4.28}$$

$$A^{-} = \begin{bmatrix} 3.736 \times 10^{-2} & 3.810 \times 10^{-1} \end{bmatrix} \tag{4.29}$$

The entropy, diversity, and weight of each attribute is

$$e = \begin{bmatrix} 9.754 \times 10^{-1} & 7.513 \times 10^{-1} \end{bmatrix} \tag{4.30}$$

$$d = \begin{bmatrix} 2.457 \times 10^{-2} & 2.487 \times 10^{-1} \end{bmatrix} \tag{4.31}$$

$$w = \begin{bmatrix} 8.989 \times 10^{-2} & 9.101 \times 10^{-1} \end{bmatrix} \tag{4.32}$$

The distance and relative closeness of each alternative to the ideal solution are calculated and presented in Table 4.8.

Table 4.8: TOPSIS results for the 75% shading case.

Bypass diodes	d_i^+	d_i^-	ζ_i
1	2.450×10^{-2}	3.596×10^{-1}	9.362×10^{-1}
2	2.228×10^{-2}	3.559×10^{-1}	9.411×10^{-1}
3	2.198×10^{-2}	3.521×10^{-1}	9.412×10^{-1}
4	2.128×10^{-2}	3.483×10^{-1}	9.424×10^{-1}
6	2.339×10^{-2}	3.409×10^{-1}	9.358×10^{-1}
8	2.860×10^{-2}	3.334×10^{-1}	9.210×10^{-1}
12	4.226×10^{-2}	3.185×10^{-1}	8.828×10^{-1}
16	5.703×10^{-2}	3.035×10^{-1}	8.418×10^{-1}
24	8.713×10^{-2}	2.734×10^{-1}	7.583×10^{-1}
32	1.174×10^{-1}	2.433×10^{-1}	6.746×10^{-1}
48	1.779×10^{-1}	1.832×10^{-1}	5.073×10^{-1}
96	3.596×10^{-1}	2.450×10^{-2}	6.377×10^{-2}

Table 4.8 revealed that a PV module design with 4 bypass diodes reported the highest value of relative closeness ζ, and is therefore chosen as the optimal solution.

4.3.3.4 100% Shading

Equation (4.33) represents the normalized decision matrix for the 100% shading case.

$$P_{100\%} = \begin{bmatrix} 1.169 \times 10^{-4} & 3.968 \times 10^{-3} \\ 2.324 \times 10^{-2} & 7.937 \times 10^{-3} \\ 4.421 \times 10^{-2} & 1.190 \times 10^{-2} \\ 5.935 \times 10^{-2} & 1.587 \times 10^{-2} \\ 7.891 \times 10^{-2} & 2.381 \times 10^{-2} \\ 9.004 \times 10^{-2} & 3.175 \times 10^{-2} \\ 1.029 \times 10^{-1} & 4.762 \times 10^{-2} \\ 1.099 \times 10^{-1} & 6.349 \times 10^{-2} \\ 1.171 \times 10^{-1} & 9.524 \times 10^{-2} \\ 1.208 \times 10^{-1} & 1.270 \times 10^{-1} \\ 1.248 \times 10^{-1} & 1.905 \times 10^{-1} \\ 1.287 \times 10^{-1} & 3.810 \times 10^{-1} \end{bmatrix} \tag{4.33}$$

$$A^{+} = \begin{bmatrix} 1.287 \times 10^{-1} & 3.968 \times 10^{-3} \end{bmatrix} \tag{4.34}$$

$$A^{-} = \begin{bmatrix} 1.169 \times 10^{-4} & 3.810 \times 10^{-1} \end{bmatrix} \tag{4.35}$$

The entropy, diversity, and weight of each attribute is

$$e = \begin{bmatrix} 9.327 \times 10^{-1} & 7.513 \times 10^{-1} \end{bmatrix} \tag{4.36}$$

$$d = \begin{bmatrix} 6.725 \times 10^{-2} & 2.487 \times 10^{-1} \end{bmatrix} \tag{4.37}$$

$$w = \begin{bmatrix} 2.128 \times 10^{-1} & 7.872 \times 10^{-1} \end{bmatrix} \tag{4.38}$$

The distance and relative closeness of each alternative to the ideal solution are calculated and presented in Table 4.9. For the 100% shading case, Table 4.9 demonstrates an optimal solution of 6 bypass diodes, that is, one bypass diode connected to each group of 16 PV cells.

As we notice from the entropy and TOPSIS analysis results, the number of optimal bypass diodes increases as the shading percent increase. This is attributable to the pattern observable in Figure 4.7. The effect of increasing the number of bypass diodes on the generated power is substantial as the degree of shading becomes more significant. The diversity in the mean value of P_{mp} increases as the shading degree increases, resulting in a larger entropy weight being assigned to the power attribute. This is in agreement with results predicted by Equations (4.20), (4.26), (4.32), and (4.38). The optimal solution, however, can be different if the weight of the attribute is subjective, with pre-determined weights solely dependent on the decision makers' preference, judgment, or experience.

Table 4.9: TOPSIS results for the 100% shading case.

Bypass diodes	d_i^+	d_i^-	ζ_i
1	5.932×10^{-2}	3.345×10^{-1}	8.493×10^{-1}
2	4.879×10^{-2}	3.311×10^{-1}	8.716×10^{-1}
3	3.962×10^{-2}	3.281×10^{-1}	8.923×10^{-1}
4	3.369×10^{-2}	3.251×10^{-1}	9.061×10^{-1}
6	2.894×10^{-2}	3.189×10^{-1}	9.168×10^{-1}
8	3.042×10^{-2}	3.126×10^{-1}	9.113×10^{-1}
12	4.052×10^{-2}	2.995×10^{-1}	8.808×10^{-1}
16	5.352×10^{-2}	2.862×10^{-1}	8.424×10^{-1}
24	8.115×10^{-2}	2.592×10^{-1}	7.615×10^{-1}
32	1.092×10^{-1}	2.321×10^{-1}	6.800×10^{-1}
48	1.655×10^{-1}	1.785×10^{-1}	5.189×10^{-1}
96	3.345×10^{-1}	5.932×10^{-2}	1.507×10^{-1}

4.4 Concluding Remarks

A computational algorithm was developed for optimizing PV cell network design. In this study, the effect of using bypass diodes in a PV module with shaded cells was examined. Ideally, it was found that the optimal situation corresponds to having one bypass diode connected to each cell in the module; however, by factoring in diode cost, it was found that using fewer bypass diodes was economically more practical.

Combining information entropy weight with TOPSIS methods enabled us to determine the optimal design for each shading case. It was found that as the shading degree increases, the diversity in the generated power increases, and as a result, the performance attribute was assigned a higher weight. Hence, as the shading increases, the optimal solution shifts towards having a higher number of bypass diodes. For the 25% and 50% shading, the analysis suggests an optimal design of one bypass diode in the PV module. However, 4 and 6 bypass diodes were found to be the optimal design for the 75% and 100% shading cases, respectively.

Our algorithm can find the optimum configuration of bypass diodes for any module with PV cells wired in series. The MC simulation allows for consideration of different shading patterns once the statistical distribution of the shading effect is approximated. The approach developed in this work can be extended to include randomly distributed manufacturing and other defects.

Chapter 5: Conclusions and Future Work

Theoretical and experimental based analysis approaches were combined in Chapter 2 to investigate the kinetics and mechanism of OER and HER on the active NiFe LDH electrodes. Both LSV and EIS measurements were taken, and the results were fitted to a theoretical model representing the current density and Faradaic resistance. The chemical reaction rate constants of the OER and HER were identified as a result of the fitting procedure. The kinetics parameters of the HER identified the Heyrovsky step as rate controlling, with a dependency of the mechanism on the potential. At lower end of potential range, the Volmer step initiates the HER, followed by parallel Tafel and Heyrovsky steps. At higher potential, the HER mechanism was a consecutive combination of Volmer and Heyrovsky step, with negligible contribution of the Tafel step. The OER results pointed to the formation of the adsorbed peroxide (HOO) step as rate controlling.

Understanding the kinetic and mechanistic behavior of a system is crucial to improving process design and operation control. A key contribution of this work is that the level of modeling detail enables predicting the effect of variations in certain process parameters such as operational temperature and electrolyte concentration.

In addition to process design implications, this work can be employed for catalyst design principals. The kinetic approach presented in this work enables the identification of the rate determining step, giving insight into the reaction mechanism. It is known in the literature that shifting the rate controlling step to a later stage in the mechanism provides lower Tafel slope values and a higher electrocatalytic activity [27]. To illustrate, if analysis of a catalyst reveals the Volmer adsorption step for the HER as rate controlling with a Tafel slope of 120 mV/dec, then tailoring catalyst design to enhance the adsorption step can be beneficial in optimizing catalytic performance.

In Chapter 3, we applied the electrolysis cell current-voltage characteristics expression derived in the previous chapter to optimize a commercial scale hydrogen production electrolyzer unit. A computational algorithm was presented to model and optimize the design of an integrated PV-Electrolysis-Battery system, with the goals of maximizing hydrogen production and minimizing system's cost while having an annual net-grid energy that falls within $\pm 5\%$ relative to daily electrolyzer power consumption. The approach investigated a total of 2,364,120 design configurations, 13 of which were identified as Pareto optimal designs for this problem.

The computational algorithm presented can be extended to more complex hybrid systems. Unlike most studies that run the simulation for only a single day, our model is simulated over one year to include both diurnal and seasonal weather variations, enhancing the applicability of the optimal designs in real life.

Computational tools were presented in Chapter 4 to identify optimal design configurations when integrating a large number of PV cells under shady or faulty conditions. Event driven Monte Carlo simulation was used to simulate the stochastic effects of partial shading of some cells in the PV module.

To identify the optimal number of bypass diodes in the PV module, a multi-objective optimization problem was investigated to minimize both the system's performance losses caused by PV cell mismatch and the added cost of bypass diodes. Information entropy weight and TOPSIS methods were combined to identify the optimal number of bypass didoes for each shading case considered. It was found that as the shading increases, the optimal solution shifts towards a having higher number of bypass diodes. A key contribution of this work is that this computational platform can be extended towards developing simulation-based design tools for the integration of nano-scale energy devices.

5.1 Suggestions for Future Work

5.1.1 Integrating Wind as Energy Source

It would be interesting to include wind energy as an additional renewable energy source to power the electrolyzer. With the inclusion of wind energy, the coupled system can be designed to be a stand alone system (i.e., off-grid). Design variables can be extended to include the number of wind turbine (WT) towers.

Because this would be a stand alone system, the optimization objective would be to maximize the system's reliability by minimizing the probability that the hybrid power system (PV, WT, Battery) is unable to provide sufficient power supply to the electrolyzer. Additionally, the overall objective would include maximizing the hydrogen production rate and minimizing the total system's cost. Because wind energy generally is at its minimum when solar irradiance is at its peak and relatively high at night [47], it would be interesting to study the interplay between PV and WT sizing and their effect on hydrogen production and the system's reliability and cost.

5.1.2 Species Concentration Profile in the Electrolyte

Understanding the dynamics of species concentration spacial profiles in the electrolyte between the electrodes is important for process design and operation. This is particularly valuable for direct-coupled PV-electrolysis stand alone systems (e.g, a stand alone car fueling station). In these systems, the fast transients, such as the sudden reduction of irradiance due to a passing cloud, can have an impact on the electrolyzer operation. Now that the reaction kinetics at the electrodes surface have been identified in Chapter 2, we can investigate the dynamics and time scale of species concentration profile under sudden changes before the system returns to its steady state operation.

5.1.3 Dynamic Model for the Electrolyzer

Another direction for future work is the development of a dynamic model for the electrolyzer to investigate the impact of diurnal irradiance variations as well as irradiance dynamics resulting from passing clouds. It would be interesting to understand the timescales of the electrolyzer compared to changes in irradiance. Additionally, a nice objective of this work would be to evaluate whether it is more economical to provide battery backup to smooth the faster time scale irradiance disturbances or if the electrolyzer system is robust to those dynamics.

5.1.4 Energy Optimization: International Space Station Case Study

Currently, the PV modules are the main energy source in the International Space Station (ISS). The PV modules generate sufficient energy to cover the fixed and variable loads in the station, while charging the battery bank. The battery operate the station during times of low irradiance. Electrolysis cells are used to produce oxygen gas for convenient air quality for the crew. Currently, the produced hydrogen gas from water electrolysis is vented to space [77].

Researchers are investigating a regenerative fuel cell (RFC) system to store energy on the ISS. The system can operate in electrolysis mode powered by solar cells, and fuel cell mode to produce electricity, water and heat [78].

Given the fixed and variable loads in the ISS, an energy optimization problem can be investigated. The problem has interesting dynamics given the 90-minute orbit of the ISS resulting in continuous changes in the irradiance angle of incidence,

the complete shading of the earth's shadow, and the reflected light from the Earth and Moon.

Bibliography

[1] Hosseini, S. E. and M. Abdul Wahid, "Hydrogen Production from Renewable and Sustainable Energy Resources: Promising Green Energy Carrier for Clean Development", *Renewable & Sustainable Energy Reviews* **57** (2016) 850-866.

[2] Staffell, I., D. Scamman, A. V. Abad, P. Balcombe, P. E. Dodds, P. Ekins, N. Shah and K. R. Ward, "The role of hydrogen and fuel cells in the global energy system", *Energy & Environmental Science* **12** 2 (2019) 463-491.

[3] Brandon, N. P. and Z. Kurban, "Clean energy and the hydrogen economy", *Philosophical Transactions of the Royal Society A* **375** 2098 (2017).

[4] Ursua, A., L. M. Gandia, P. Sanchis, "Hydrogen production from water electrolysis: current status and future trends", *Proceedings of the IEEE* **100** 2 (2012).

[5] Gardner, D., "Hydrogen production from renewables", *Renewable Energy Focus* **9** 7 (2009) 34-7.

[6] Santos, D. M., C. A. Sequeira, and J. L. Figueiredo, "Hydrogen production by alkaline water electrolysis", *Quimica Nova* **36** (2013) 1176-1193.

[7] Luo, J., J. Im, M. T. Mayer, M. Schreier, M. K. Nazeeruddin, N. Park, S. D. Tilley, H. J. Fan, and M. Gratzel, "Water photolysis at 12.3% efficiency via perovskite photovoltaics and Earth-abundant catalysts", *Science* **345** (2014) 1593-1596.

[8] Fan, G., F. Li, D. G. Evans, and X. Duan, "Catalytic applications of layered double hydroxides: recent advances and perspectives", *Chemical Society Reviews* **43**20 (2014) 7040–7066.

[9] Lu, Z., W. Xu, W. Zhu, Q. Yang, X. Lei, J. Liu, Y. Li, X. Sun, and X. Duan, "Three-dimensional NiFe layered double hydroxide film for high-efficiency oxygen evolution reaction", *Chem. Commun.* **50** (2014) 6479-6482.

[10] Li, F. and X. Duan, "Applications of layered double hydroxides", *Structure and Bonding* **119** (2005) 193-224, Springer, Berlin, Heidelberg.

[11] Fan K., H. Chen,Y. Ji, H. Huang, P. M. Claesson, Q. Daniel, B. Philippe, H. Rensmo, F. Li, Y. Luo, and L. Sun, "Nickelvanadium monolayer double hydroxide for efficient electrochemical water oxidation", *Nat. Commun.* **7** (2016) 11981.

[12] Hou, Y., M. R. Lohe, J. Zhang, S. Liu, X. Zhuang, and X. Feng, "Vertically oriented cobalt selenide/NiFe layered-double-hydroxide nanosheets supported on exfoliated graphene foil: an efficient 3D electrode for overall water splitting" *Energy & Environmental Science*, **9** 2 (2016) 478–483.

[13] Nayak, S., L. Mohapatra, and K. Parida, "Visible light-driven novel gC_3N_4/NiFe-LDH composite photocatalyst with enhanced photocatalytic activity towards water oxidation and reduction reaction", *Journal of Materials Chemistry A*, **3** 36 (2015) 18622–18635.

[14] Ohashi, H., H. Zhang, P. Zhang, T. Tamaki, G. M. Anilkumar, and T. Yamaguchi, "Layered Double Hydroxide as a Potential Electrolyte Material in Solid-State Alkaline Fuel Cell Catalyst Layer". *ECS Electrochemistry Letters*, **4** 8 (2015) F47–F49.

[15] Li, X., P. Gong, Y. Li, J. Yu, F. Wang, X. Li, Z. Fan, and Z. Wang, "Double-carrier drug delivery system based on polyurethane-polyvinyl alcohol/layered double hydroxide nanocomposite hydrogel", *Materials Letters* **243** (2019) 1–4.

[16] Hamann, T., "Perovskites take lead in solar hydrogen race", *Science* **345** (2014) 1566-1567.

[17] Chen, G., T. Wang, J. Zhang, P. Liu, H. Sun, X. Zhuang, M.Chen, and X. Feng, "Accelerated hydrogen evolution kinetics on NiFelayered double hydroxide electrocatalysts by tailoring water dissociation active sites", *Adv. Mater.* **30** (2018) 1706279.

[18] Chen, Q. Q., C. C. Hou, C. J. Wang, X. Yang, R. Shi, and Y. Chen, "Ir^{4+}-Doped NiFe LDH to expedite hydrogen evolution kinetics as a Pt-like electrocatalyst for water splitting", *Chem. Commun.* **54** (2018) 6400.

[19] Azizi, O., M. Jafarian, F. Gobal, H. Heli, and M.G. Mahjani, "The investigation of the kinetics and mechanism of hydrogen evolution reaction on tin", *Int. J. Hydrogen Energy* **32** (2007) 1755-1761.

[20] Dau, H., C. Limberg, T. Reier, M. Risch, S. Roggan, and P. Strasser, "The mechanism of water oxidation: from electrolysis via homogeneous to biological catalysis", *ChemCatChem* **2** 7 (2010) 724-761.

[21] Krstajic, N., M. Popovic, B. Grgur, M. Vojnovic, and D. Sepa, "On the kinetics of the hydrogen evolution reaction on nickel in alkaline solution: Part I. The mechanism", *J. Electroanal. Chem.* **512** (2001) 16-26.

[22] Doyle, R. L. and M. E. G. Lyons, "An electrochemical impedance study of the oxygen evolution reaction at hydrous iron oxide in base", *Phys. Chem. Chem. Phys.* **15** (2013) 5224-5237.

[23] Hu, J. M., J. Q. Zhang, and C. N. Cao, "Oxygen evolution reaction on IrO_2-based DSA type electrodes: kinetics analysis of Tafel lines and EIS" *International Journal of Hydrogen Energy* **29** 8 (2004) 791–797.

[24] Garcia-Osorio, D. A., R. Jaimes, J. Vazquez-Arenas, R. H. Lara, and J. Alvarez-Ramirez, "The Kinetic Parameters of the Oxygen Evolution Reaction (OER) Calculated on Inactive Anodes via EIS Transfer Functions: OH Formation", *J. Electrochem. Soc.* **164** 11 (2017) E3321–E3328.

[25] Doyle R. L. and M. E. G. Lyons, "Kinetics and mechanistic aspects of the oxygen evolution reaction at hydrous iron oxide films in base", *J. Electrochem. Soc.* **160** (2013) H142-H154.

[26] Zeng, K. and D. Zhang, "Recent progress in alkaline water electrolysis for hydrogen production and applications",*Prog. Energy Combust. Sci.* **36** (2010) 307-326.

[27] Doyle, R. L. and M. E. G. Lyons, "The oxygen evolution reaction: mechanistic concepts and catalyst design", *Photoelectrochem. Solar Fuel Production* (2016) 41-104, Springer, Cham.

[28] Shinagawa, T., A. T. Garcia-Esparza, and K. Takanabe, "Insight on Tafel slopes from a microkinetic analysis of aqueous electrocatalysis for energy conversion", *Scientific reports* **5** (2015) 13801.

[29] Zhu, Y., T. Liu, L. Li, S. Song, and R. Ding, "Nickel-based electrodes as catalysts for hydrogen evolution reaction in alkaline media", *Ionics* **24** (2018) 1121-1127.

[30] Hitz, C. and A. Lasia, "Experimental study and modeling of impedance of the her on porous Ni electrodes", *J. Electroanal. Chem.* **500** (2001) 213-222.

[31] Ye, C.Q., R.G. Hu, S.G. Dong, X.J. Zhang, R.Q. Hou, R.G. Du, C.J. Lin, and J.S. Pan, "EIS analysis on chloride-induced corrosion behavior of reinforcement steel in simulated carbonated concrete pore solutions", *Journal of Electroanalytical Chemistry* **688** (2013) 275–281.

[32] Franceschini, E. A., G. I. Lacconi, H. R. Corti, "Kinetics of the hydrogen evolution on nickel in alkaline solution: new insight from rotating disk electrode and impedance spectroscopy analysis", *Electrochim. Acta* **159** (2015) 210-218.

[33] Yin, X., G. Sun, A. Song, L. Wang, Y. Wang, H. Dong, and G. Shao, "A novel structure of Ni-(MoS_2/GO) composite coatings deposited on Ni foam under supergravity field as efficient hydrogen evolution reaction catalysts in alkaline solution", *Electrochim. Acta* **249** (2017) 52-63.

[34] "ZView impedance /gain phase graphing and analysis software operating manual, version 3.5, revision F (11/2017)", *Scribner Associates, Inc.* Retrieved by email from info@scribner.com on Feb 19, 2018.

[35] Lyons, M. E., and M. P. Brandon, "The oxygen evolution reaction on passive oxide covered transition metal electrodes in aqueous alkaline solution. Part 1-Nickel", *Int. J. Electrochem. Sci* **3** (2008) 1386-1424.

[36] Dong, Y., P. Zhang, Y. Kou, Z. Yang, Y. Li, and X. Sun, "A first-principles study of oxygen formation over NiFe-layered double hydroxides surface", *Catal. Lett.* **145** (2015) 1541-1548.

[37] Louie, M. W. and A. T. Bell, "An investigation of thin-film NiFe oxide catalysts for the electrochemical evolution of oxygen", *J. Am. Chem. Soc.* **135** (2013) 12329-12337.

[38] Zheng, X., Z. Yang, J. Wu, C. Jin, J. H. Tian, and R. Yang, "Phosphorus and cobalt co-doped reduced graphene oxide bifunctional electrocatalyst for oxygen reduction and evolution reactions", *RSC Adv.* **6** (2016) 64155-64164.

[39] Li, G., L. Anderson, Y. Chen, M. Pan, and P.Y.A. Chuang, "New insights into evaluating catalyst activity and stability for oxygen evolution reactions in alkaline media", *Sustainable Energy Fuels* **2** 1 (2018) 237-251.

[40] Brug, G. J., A.L.G. Van Den Eeden, M. Sluyters Rehbach, and J.H. Sluyters, "The analysis of electrode impedances complicated by the presence of a constant

phase element", *J. Electroanal. Chem. Interfacial Electrochem.* **176** (1984) 275-295.

[41] Hirschorn, B., M. E. Orazem, B. Tribollet, V. Vivier, I. Frateur, and M. Musiani, "Determination of effective capacitance and film thickness from constant-phase-element parameters", *Electrochim. Acta*, **55** 21 (2010) 6218-6227.

[42] Zhang, F., J. Liu, I. Ivanov, M. C. Hatzell, W. Yang, Y. Ahn, and B. E. Logan, "Reference and counter electrode positions affect electrochemical characterization of bioanodes in different bioelectrochemical systems", *Biotechnol. Bioeng.* **111** (2014) 1931-1939.

[43] Conibeer, G. J. and B. S. Richards, "A comparison of PV/electrolyser and photoelectrolytic technologies for use in solar to hydrogen energy storage systems", *Int. J. Hydrogen Energy* **32** (2007) 2703-2711.

[44] Esposito, D. V., "Membraneless electrolyzers for low-cost hydrogen production in a renewable energy future", *Joule* **1** 4 (2017) 651-658.

[45] Fu, R., D. Feldman, R. Margolis, M. Woodhouse, and K. Ardani, "U.S. solar photovoltaic system cost benchmark: Q1 2017", *National Renewable Energy Laboratory* (2017). Retrieved from: https://www.nrel.gov/docs/fy17osti/68925.pdf

[46] Gibson, T. L., N. A. Kelly, "Optimization of solar powered hydrogen production using photovoltaic electrolysis devices", *International journal of hydrogen energy* **33** 21 (2008) 5931-5940.

[47] Khalilnejad, A., A. Sundararajan, and A. I. Sarwat, "Optimal design of hybrid wind/photovoltaic electrolyzer for maximum hydrogen production using imperialist competitive algorithm", *Journal of Modern Power Systems and Clean Energy* **6** 1 (2018) 40-49.

[48] Lagorse, J., D. Paire, and A. Miraoui, "Sizing optimization of a stand-alone street lighting system powered by a hybrid system using fuel cell, PV and battery", *Renewable Energy* **34** 3 (2009) 683-691.

[49] Hassan, S. Z., S. Mumtaz, T. Kamal, and L. Khan, "Performance of grid-integrated photovoltaic/fuel cell/electrolyzer/battery hybrid power system", *Power Generation System and Renewable Energy Technologies (PGSRET)*, 1-8, IEEE, (2015).

[50] Yang, H., Z. Wei, and L. Chengzhi, "Optimal design and techno-economic analysis of a hybrid solar-wind power generation system", *Applied energy*, **86** 2 (2009) 163-169.

[51] Adomaitis, R. A., *Solar energy lecture notes: "Modeling and analysis of photovoltaic and related solar energy systems"* (2018).

[52] Wenham, S. R., M. A. Green, M. E. Watt, R. Corkish, and A. Sproul, *Applied Photovoltaics*. 3rd ed. Hoboken: Taylor and Francis,(2013).

[53] The Dark Sky API. https://darksky.net/dev. Accessed June 6, 2018.

[54] SunPower product data sheet. Retrieved from: https://us.sunpower.com/solar-panels-technology/x-series-solar-panels/. Accessed May 17, 2018.

[55] Zeng, K. and D. Zhang, "Recent progress in alkaline water electrolysis for hydrogen production and applications", *Progress in energy and combustion science* **36** 3 (2010) 307-326.

[56] Ulleberg, O., "Modeling of advanced alkaline electrolyzers: a system simulation approach", *International journal of hydrogen energy*, **28** 1 (2003) 21-33.

[57] Buttler, A., and H. Spliethoff, "Current status of water electrolysis for energy storage, grid balancing and sector coupling via power-to-gas and power-to-liquids: a review", *Renewable and sustainable energy reviews* **82** (2018) 2440-2454.

[58] Koponen, J., "Review of water electrolysis technologies and design of renewable hydrogen production systems", *MS Thesis*, (2015).

[59] AGFA Specialty Products. http://www.agfa.com/specialty-products/solutions/membranes/zirfon-perl-utp-500/. Accessed May 22, 2018.

[60] Gilliam, R. J., J. W. Graydon, D. W. Kirk, S. J. Thorpe, "A review of specific conductivities of potassium hydroxide solutions for various concentrations and temperatures", *International journal of hydrogen energy* **32** 3 (2007) 359-364.

[61] May, G. J., A. Davidson, B. Monahov, "Lead batteries for utility energy storage: a review", *Journal of energy storage* **15** (2018) 145-157.

[62] Fathima, H. and K. Palanisamy, "Optimized sizing, selection, and economic analysis of battery energy storage for grid-connected wind-PV hybrid system", *Modelling and simulation in engineering* **2015** (2015).

[63] Locatelli, G., S. Boarin, A. Fiordaliso, and M. Ricotti, "Load following of small modular reactors (smr) by cogeneration of hydrogen: A techno-economic analysis", *Energy*, **148** (2018).

[64] Bertuccioli, L., A. Chan, D. Hart, F. Lehner, B. Madden, and E. Standen, "Development of water electrolysis in the European Union", *Fuel Cells and Hydrogen Joint Undertaking*, (2014).

[65] The U.S. Energy Information Administration, "2017 average monthly bill- commercial". Retrieved from: https://www.eia.gov/electricity/sales_revenue_price/pdf/table5_b.pdf. Accessed December 27, 2018.

[66] Yang, H., L. Lu, and W. Zhou, "A novel optimization sizing model for hybrid solar-wind power generation system", *Solar Energy* **81** 1 (2007) 76-84.

[67] Mukherjee, U., A. Maroufmashat, J. Ranisau, M. Barbouti, A. Trainor, N. Juthani, H. El-Shayeb, and M. Fowler, "Techno-economic, environmental, and safety assessment of hydrogen powered community microgrids; case study in Canada", *International Journal of Hydrogen Energy*, **42** 20 (2017) 14333–14349.

[68] Banerjee, P., I. Perez, L. Henn-Lecordier, S. Lee, and G. Rubloff, "Nanotubular metal-insulator-metal capacitor arrays for energy storage", *Nature Nanotechnology* **4** 5 (2009) 292-296.

[69] Krogstrup, P., H. Jorgensen, M. Heiss, O. Demichel, J. Holm, M. Aagesen, J. Nygard and A. Morral, "Single-nanowire solar cells beyond the ShockleyQueisser limit", *Nature Photonics* **7** (2013) 306-310.

[70] Singh, P., M. Niamat, and S. Vemuru, 2011, "Modeling of random shading effects in solar cells", *21st International Conference on Systems Engineering (ICSEng)* (2011).

[71] Vemuru, S., P. Singh, and M. Niamat, "Modeling impact of bypass diodes on photovoltaic cell performance under partial shading", *IEEE International Conference on Electro/Information Technology EIT*, (2012).

[72] Silvestre, S., A. Boronat, and A. Chouder, "Study of bypass diodes configuration on PV modules", *Applied Energy* **86** 9 (2009) 1632-1640.

[73] TEXAS INSTRUMENTS Smart Bypass Diode SM74611 datasheet. http://www.ti.com/product/SM74611/samplebuy. Accessed Feb 12, 2019.

[74] Wang, T., and H. Lee, "Developing a fuzzy TOPSIS approach based on subjective weights and objective weights", *Expert Systems with Applications*, **36** 5 (2009) 8980-8985.

[75] Huang, J., "Combining entropy weight and TOPSIS method for information system selection", *IEEE Conference on Cybernetics and Intelligent Systems (CIS)*, Chengdu, China, (2008) 1281-1284.

[76] Hwang, C. L. and K. S. Yoon, "Multiple attribute decision making: methods and applications: A state-of-the-art survey". Berlin: Springer-Verlag, (1981).

[77] "Reference guide to the International Space Station Utlization Edition NP-2015-05-022-JSC", *National Aeronautics and Space Administration*, September (2015), Retrieved from: https://www.nasa.gov/sites/default/files/atoms/files/np-2015-05-022-jsc-iss-guide-2015-update-111015-508c.pdf. Accessed March 4, 2019.

[78] Justin Fitzgerald, J. (NASA Glenn) and N. O'Bryan (InDyne, Inc.), "Fuel cells: A better energy source for earth and space", Retrieved from: https://www.nasa.gov/centers/glenn/technology/fuel_cells.html. Accessed March 4, 2019.

Publications & Presentations

Publications

Alobaid, A., C. S. Wang, and R. A. Adomaitis, "Mechanism and kinetics of HER and OER on NiFe LDH films in an alkaline electrolyte", *J. Electrochem. Soc.* **165** (2018) J3395-3404, DOI: 10.1149/2.0481815jes

Alobaid, A., H. Salami, and R. A. Adomaitis, "On the computation and interpretation of semi-positive reaction network invariants", *Computers & Chem. Eng.* **117** (2018) 236-248, DOI: 10.1016/j.compchemeng.2018.06.009

Alobaid, A. and R. A. Adomaitis, "Monte Carlo simulation for optimal solar cell configuration", *Proceedings of PSE 2018*, (2018), DOI: 10.1016/b978-0-444-64241-7.50304-9

Publications to be Submitted

Alobaid, A. and R. A. Adomaitis, "Sizing optimization of a coupled photovoltaic-electrolysis-battery System for hydrogen generation", manuscript to be submitted: April (2018).

Presentations

Alobaid* A., C. Wang, and R. A. Adomaitis, "Kinetic investigation of nickel-iron layered double hydroxide for hydrogen evolution in an alkaline electrolyte", Paper 217f, *AICHE Annual Meeting*, Pittsburgh, PA, October 28–November 2, (2018).

Alobaid* A., and R.A. Adomaitis, "Optimal solar cell configuration under partially shaded conditions ", Paper 182B, *AICHE Annual Meeting*, Pittsburgh, PA, October 28–November 2, (2018).

Salami* H., A. Alobaid, and R. A. Adomaitis, "A combined graphical/algebraic method for model reduction and analysis of chemical reaction networks: Application to atomic layer deposition process", Paper 182a, *AICHE Annual Meeting*, Pittsburgh, PA, October 28–November 2, (2018).

Alobaid* A., C. Wang, and R.A. Adomaitis, "Kinetic investigation of nickle-iron layered double hydroxide toward hydrogen evolution in alkaline electrolyte", *UMD Research Fest*, College Park, MD, Jun 29, (2018).

Alobaid* A., and R.A. Adomaitis, Monte Carlo simulation for optimal solar cell configuration", Paper 605, *Process Systems Engineering (PSE 2018)*, San Diego, CA, July 1–5, (2017).

Alobaid* A., and R.A. Adomaitis, Modeling a coupled photovoltaic-photoelectrochemical (PV-PEC) system for hydrogen generation, *The Institute for Systems Research (ISR) Celebration of Research Event*, UMD, College Park, MD, May (2017).

* denotes the presenter